

**A TWENTY-EIGHT CHANNEL COIL ARRAY FOR
IMPROVED OPTIC NERVE IMAGING**

by

Robb Phillip Merrill

A thesis submitted to the faculty of
The University of Utah
in partial fulfillment of the requirements for the degree of

Master of Science

Department of Electrical and Computer Engineering

The University of Utah

May 2010

Copyright © Robb Phillip Merrill 2010

All Rights Reserved

STATEMENT OF THESIS APPROVAL

The thesis of _____ **Robb Phillip Merrill** _____

has been approved by the following supervisory committee members:

_____ **Cynthia M. Furse** _____, Chair _____ **3/23/2010** _____
Date Approved

_____ **Dennis L. Parker** _____, Member _____ **3/23/2010** _____
Date Approved

_____ **J. Rock Hadley** _____, Member _____ **3/23/2010** _____
Date Approved

and by _____ **Gianluca Lazzi** _____, Chair of

the Department of _____ **Electrical and Computer Engineering** _____

and by Charles A. Wight, Dean of The Graduate School.

ABSTRACT

The purpose of this work was to design and construct a radio-frequency coil optimized for imaging the Optic Nerve (ON) on a Siemens 3T magnetic resonance imaging (MRI) scanner. The specific goals were to optimize signal sensitivity from the orbit to the optic chiasm and improve SNR over designs currently in use. The constructed coil features two fiberglass formers that can slide over each other to accommodate any arbitrary head size, while maintaining close coupling near the eyes and around the head in general. This design eliminates the air void regions that occur between the coil elements and the forehead when smaller heads are imaged in one-piece, nonadjustable coil formers. The 28 coil elements were placed using a soccer-ball pattern layout to maximize head coverage. rSNR profiles from phantom imaging studies show that the ON coil provides approximately 55% greater rSNR at the region of the optic chiasm and approximately 400% near the orbits compared to the 12-channel commercial coil. The improved rSNR in the optic nerve region allows performance of high resolution DTI, which provides a qualitative measurement for evaluating optic neuritis. Images from volunteer and patient studies with the ON coil reveal plaques that correspond well with the patient disease history of chronic bilateral optic neuritis. Correspondence of image findings with patient disease histories demonstrates that optic neuritis can be visualized and detected in patients using 3T MRI with advanced imaging coils, providing improved patient care.

FOREWORD

18 March 2010

The Optic Nerve Coil for the Siemens 3T MRI has already accomplished two major objectives: 1) improved imaging for the optic nerve, chiasm and optic tracts as well as the orbit, and 2) imaging of the optic nerve for research purposes.

The first objective is critical for the clinical setting where previous imaging of the optic nerve, for example, has not been well resolved and prone to variation leading to difficulty in accurate interpretation of images. In practice the optic nerve coil has been effective in eliminating artifact that complicated interpretation of images. This development is a great improvement and important for confirmation of the clinical diagnosis of optic neuritis. Going forward there are unlimited opportunities to apply the imaging with this coil to diseases of the optic nerve and visual pathway as well as studies of the eye and ocular muscles.

The second objective includes the use of the coil with advanced imaging protocols to produce data indicating the types of tissue damage in the optic nerve including inflammation, demyelination and axonal injury. Initial studies with the optic nerve coil and protocols for diffusion imaging are most promising. We will now have an innovative research tool for natural history studies of optic neuritis. In addition, these techniques can

also be utilized in the assessment of optic neuritis and response to therapies in formal clinical trials.

In summary, the development and implementation of the optic nerve coil provides a foundation for future clinical and research applications.

John Rose, M.D.

Professor of Neurology
The Brain Institute

Chief of Neurology
VA Hospital

TABLE OF CONTENTS

ABSTRACT	iii
FOREWORD	iv
Chapter	
1 INTRODUCTION	1
1.1 Project Background	1
1.2 Outline of Thesis	4
2 COIL BACKGROUND	7
2.1 Spin Behavior in a Magnetic Field	7
2.1.1 Basic Spin Theory	7
2.1.2 The Bloch Equation	19
2.1.3 MRI Scanner Components	23
2.2 Faraday's Law	28
2.2.1 Derivation of Faraday's Law	28
2.2.2 Coil Orientation	33
2.2.3 Coil Cross-sectional Profiles	36
2.3 Coil Performance	42
2.3.1 Quality Factor	42
2.3.2 S-parameters	47
2.3.3 Electric Fields and Coil Noise	50
2.3.4 SNR Considerations	58
2.4 Overlap Theory	59
2.4.1 Volume Imaging	59
2.4.2 Coil Overlapping	64
2.5 Decoupling Theory and the Preamplifier Board	73
2.5.1 Traps	77
2.5.2 The Coil Cable and Common-Mode Currents	80
2.5.3 Active and Passive Decoupling	82
2.5.4 Preamplifier Decoupling	85
2.6 Parallel Imaging	88
2.7 Conclusion	91

3	METHODS AND COIL CONSTRUCTION	94
	3.1 Preliminary Work	95
	3.1.1 Phantom Construction	95
	3.1.2 Double-loop (S_{21}) Measurement Probe	97
	3.1.3 Q Test Jig	97
	3.1.4 Test Board	99
	3.1.5 Study #1: Variable Capacitor Q	99
	3.1.6 Study #2: Coil Construction Parameters	102
	3.2 Construction Procedure	106
4	IMAGING RESULTS	115
	4.1 Coil Layout Comparison Studies	117
	4.1.1 rSNR Comparison of Coil Layout	117
	4.1.2 Parallel Imaging Comparison	128
	4.2 Collapsible Design Comparison Studies	128
	4.2.1 rSNR Comparison of Former Design	130
	4.2.2 Multiple Head-Size Study	135
	4.2.3 Patient Studies	139
5	DISCUSSION	142
6	SUMMARY, CONCLUSIONS, AND FUTURE WORK	147
	6.1 Summary	147
	6.2 Significance	148
	6.3 Future Work	149
Appendices		
A.	MUTUAL INDUCTANCE	151
B.	MAGNETIC FIELD PROFILE PLOTS	161
	REFERENCES	174

CHAPTER 1

INTRODUCTION

1.1 Project Background

Optic neuritis is one of the first symptoms to appear during the early stages of Multiple Sclerosis (MS) [1, 2]. Optic neuritis is characterized by inflammation of the optic nerve, leading to eye movement pain, reduced color perception, poor pupillary response, and eventually complete vision loss. The most common form, acute demyelinating optic neuritis, occurs in 50% of MS patients. Data from clinical trials demonstrate a significant reduction in risk of contracting MS if demyelinating lesions are detected early enough, and therapy is initiated [3]. Consequently, there is great motivation among researchers and radiologists to produce images of the optic nerve with higher resolution, and with greater coverage of the optic pathway, from which to form more accurate diagnoses [1].

Nearly every optic nerve MRI study has reported the difficulty of performing scans of the optic pathway [1, 4, 5, 6, 7]. The nerve structure is very small (4 to 6 mm diameter) and highly mobile. Motion artifacts often make the nerve difficult to distinguish. In addition, image-obscuring susceptibility artifacts arise from the complex surrounding anatomy consisting of fat, cerebral-spinal fluid, bone, and air cavities. Consequently, optic neuritis has typically been diagnosed based on its clinical features

(eye pain, visual field loss, etc.), and MRI has been demoted to the task of ruling out alternate diagnoses [6, 7] and monitoring known lesion development [3, 5].

Recent advances in coil technology promise to move MRI to the forefront of clinical diagnosis. One such innovation is the implementation of anatomy-specific coils. Radiologists studying optic neuritis are currently investigating the use of custom built phased-array coils as an alternative to the commercially-available brain imaging coils already in use in MRI clinics. Commercial coils are usually either spherically- or cylindrically-shaped, allowing a comfortable fit for a variety of patient head shapes and sizes. Such general-purpose brain imaging coils reduce costs for clinics, but this comes at the expense of image resolution when performing detailed studies of specific anatomy. For example, when commercial coils are too large or otherwise not well fitted to a patient, large void regions typically occur around a patient's head. These imaging gaps separate the receiver coils from the desired anatomy and cause the signal-to-noise ratio (SNR) of the image to be reduced [4].

Numerous advanced phased-array head coils have been developed in recent years, ranging in complexity from 4 to 96 channels [8, 9, 10, 11, 12]. One of the more recent optic nerve-specific coils ("ONC1") developed at UCAIR consists of 20 overlapped loops of copper foil. The close-fitting mask-style construction of this phased array provides four times the SNR at the orbits than the commercial coil available from Siemens [13].

When ONC1 was presented at the 15th annual ISMRM conference [13], it evoked numerous comments from the coil hardware community about the benefits of using coils constructed from copper wire, rather than the previously-used copper foil.

Wire, it was thought, would reduce the capacitive coupling between adjacent loops at the point of coil overlap. More significantly, the use of wire as the conductor material would improve the SNR of each coil by decreasing the effect of a phenomenon known as *flux shielding*. Wiggins has recently presented a study investigating the effects of flux shielding. He compared the quality factor values (Q) of coils constructed using copper foil vs. copper wire. He showed that when coils are constructed in an overlapped array pattern, flux shielding significantly affects the Q ratio (sensitivity) of the individual loops. This effect occurs when the inductance of a loop is influenced by eddy currents in the copper of adjacent loops. Specifically, Wiggins pointed out that when a single, resonating copper foil loop element was placed into an array of overlapped foil loops, the sensitivity of the loop under test dropped by 26%. However, when a single wire loop was placed in an overlapped wire array, the sensitivity was reduced by only 6%. Wiggins concluded that the use of wire loops reduces the shielding effects of eddy currents in the surrounding copper [12, 14].

In addition to his overlap study, Wiggins published the imaging results from a 32-channel coil utilizing a novel method of arranging coil elements for full-head coverage. His study describes the construction of a dome-shaped, ‘one size fits all’ fiberglass helmet to allow room for a wide range of head sizes. The hexagon and pentagon tiling pattern of a soccer ball was created from paper cut-outs, and the vertices of each tile were transferred to the helmet to recreate the pattern on the helmet surface. This pattern was sized to allow the critical overlap to be maintained between all adjacent coils. The imaging results of the study showed that SNR gains of up to 35 times in the cortex, and 1.4 times in the corpus callosum were achieved with this full-coverage helmet design,

when compared to the Siemens eight-channel domed head coil. Wiggins attributed these improvements to two unique features: the tighter-fitting nature of the helmet and the smaller, overlapped construction of the individual coil elements [11].

This thesis describes the construction of a new coil (“ONC2”) specifically designed to image the optic nerve tract. This coil provides a number of improvements over general-purpose brain coils in the study of optic neuritis. These improvements will allow the SNR gains reported in recent studies to be realized or exceeded by merging recent imaging technology into a single coil. The coil was designed as a tight-fitting mask to allow the receiver coils to be placed very near the face regardless of the head size of the patient, thus maximizing the SNR along the optic nerve and allowing more detailed examination of deeper anatomy. In particular, the following design features have been implemented:

- (1) The coil has 26 loops arranged in a soccer ball pattern surrounding the face, with an additional two loops in the head/neck support, for full head coverage.
- (2) The fiberglass former features a collapsible design, allowing the mask to remain very near the face regardless of the head size of the patient.
- (3) The loops are made of wire rather than copper foil to reduce magnetic flux limitation through the coil.

1.2 Outline of Thesis

Chapter 2 of this thesis is devoted to the fundamental concepts of MRI and coil design. Specifically, in Section 2.1 the interaction of electromagnetic energy with biological tissue will be discussed. Section 2.2 introduces the basic principle of

Faraday's Law as it applies to receiver coils, and Section 2.3 describes measurement techniques and considerations for evaluating a coil's imaging performance. The principles of coil-to-coil decoupling, and the motivation behind these procedures, are explained in Sections 2.4 and 2.5. Descriptive, three-dimensional illustrations are plentiful throughout the chapter in order to develop in the reader an intuitive understanding of otherwise very abstract theoretical models. This visual approach provides a solid foundation for further study, if desired, into the complex mathematics governing MRI theory.

Chapter 3 explains the practical design factors involved in the construction of ONC2, as well as a step-by-step account of coil assembly. A great deal of preliminary work was required to develop measurement tools and testing devices required for accurate coil positioning. Results from many preliminary studies are covered in Chapter 3 as well. Insight from these studies influenced such construction parameters as coil material, coil size, and component selection.

The work presented in Chapter 4 shows an analysis of the phantom and volunteer studies performed using the completed coil. To determine SNR improvement, ONC2 data is compared to similar data obtained from ONC1 and from the commercial Siemens head coil. The unique fiberglass former shapes of both ONC1 and ONC2 required a dedicated imaging phantom for each respective coil. The challenge of developing a procedure to compare the two coils is described. In regard to patient studies, volunteers with known histories of chronic bilateral optic neuritis were imaged with ONC2. Comparison of the imaging results with patient symptoms revealed that an anatomy-specific MRI coil can be used as a primary means of clinical diagnosis.

Many of the problems encountered during the construction and testing of ONC2 are discussed in Chapter 5. These issues typically involved the mechanical structure of the coil, along with a number of other project considerations not directly related to Electrical Engineering.

Finally, Chapter 6 concludes the thesis with a summary of the effectiveness of patient care using custom MRI coils, and number of future studies that could be performed using ONC2 as a research platform.

CHAPTER 2

COIL BACKGROUND

2.1 Spin Behavior in a Magnetic Field

In 1952, Felix Bloch and Edward Purcell shared the Nobel Prize in Physics for a technique they developed 6 years earlier called *nuclear magnetic resonance* (NMR). After its discovery, NMR was adopted and used nearly exclusively by physicists, chemists, and biologists to study the structure of compounds at the atomic level. It took many years before technology was sufficient to construct a device that made use of NMR for medical diagnosis. However, in 1977 an Armenian-American named Raymond Damadian developed such a device and reported the first human NMR images. Since then, Damadian has come to be known as “the man who invented the MRI scanner,” and received the Lemelson-MIT Program's \$100,000 Lifetime Achievement Award in 2001 [15].

2.1.1 Basic Spin Theory

The foundation of NMR is the study of the behavior of atomic nuclei in the presence of a magnetic field. Although over 100 types of atoms exhibit the NMR phenomenon, hydrogen (^1H) is the most widely studied in medical applications due to its abundance in the human body. Hydrogen imaging is often called *proton* imaging because

the nucleus of the hydrogen atom consists of a single proton. While other nuclei such as phosphorus or sodium provide means for certain biological processes or tissues to be studied, hydrogen provides the largest and most easily distinguishable signals [16].

Angular momentum is an intrinsic property of elementary particles such as protons. In basic terms, a proton can be viewed as a rotating sphere of electric charge, similar in behavior to a spinning top. The proton has a net positive charge; the rotation of this charge about an axis gives rise to a small magnetic moment, since the definition of magnetism is the motion of electric charge (Fig. 2.1). This magnetic moment is aptly named a *spin*. [17]

The spins of individual protons interact with magnetic fields in the surrounding environment in predictable ways. If a multitude of spins are clustered together, with no external magnetic field present, the spins are oriented randomly. In mathematical terms, the vector components $\bar{\mu}_x$, $\bar{\mu}_y$, and $\bar{\mu}_z$ of all the proton magnetic moment vectors $\bar{\mu}$ sum to zero, and the region is said to have no net magnetization. This is the equilibrium state of biological tissue in a nonmagnetic environment. In response to an applied magnetic field, however, the spins rotate about the field in a manner comparable to a spinning top (Fig. 2.2). As a top spins, it tends to ‘wobble’ about a central axis. In the case of NMR, the protons also wobble, or *precess*, with the applied magnetic field (rather than gravity) forming the central axis of precession.

The rate of precession is a quantity of great importance in MR imaging, and is governed by the Larmor equation:

$$\omega = \gamma B_0 \quad [2.1]$$

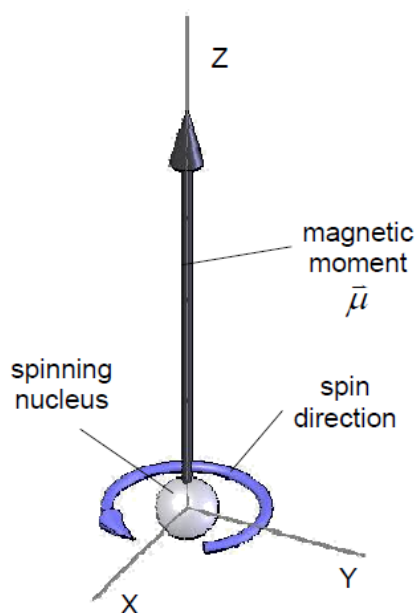


FIG. 2.1: A spinning proton creates an electric current, which in turn induces a magnetic moment $\bar{\mu}$.

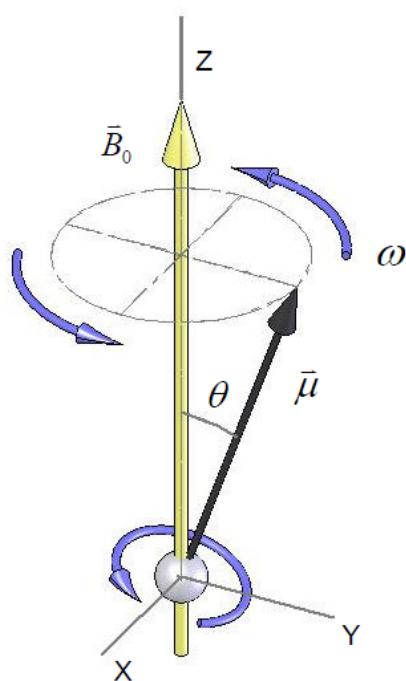


FIG. 2.2: In the presence of an external magnetic field \bar{B}_0 (directed along Z), $\bar{\mu}$ precesses about \bar{B}_0 with frequency ω .

Equation [2.1] states that the precession frequency ω is directly related to the type of atom being studied (having a unique gyromagnetic ratio γ) and the strength of the applied field (B_0). For hydrogen, the value of γ is 42.58 MHz/Tesla. A precession frequency of 123.23 MHz was measured on the Siemens 3 Tesla research scanner at UCAIR.

For convenience in quantifying the amount of NMR signal produced by a region of protons within a sample, the region can be broken into a regular pattern of volumetric units called *voxels* (see Fig. 2.3). When no external magnetic field is present, all the spins within a voxel are randomly oriented, and there is no net magnetization (as shown in Fig. 2.4). However, when an external field is applied, the precession axis of each spin aligns itself with the external field (Fig. 2.5). The resulting net magnetization \vec{M} is the vector sum of all the spin vectors $\vec{\mu}_i$ within the voxel (Fig. 2.6). At any given instant of time the vector components of $\vec{\mu}_i$ in the transverse (X-Y) plane point in essentially every radial direction with equal distribution, so all the transverse components cancel. Thus, in equilibrium, \vec{M} points along the direction of \vec{B}_0 and, due to their completely random orientation, the individual spins have no precession phase coherence.

Nuclear magnetic moments do not always align themselves *parallel* to an applied field. Probabilistically, some moments happen to have a slightly higher energy, and reside in an *antiparallel* alignment. This difference in low- and high-energy states arises from elementary quantum mechanics. When a region of atoms in thermal equilibrium is placed into an environment with a static magnetic field, the number of nuclei in the lower-energy parallel state (N_P) is slightly higher than the number of nuclei in the higher-energy antiparallel state (N_{AP}) by the ratio

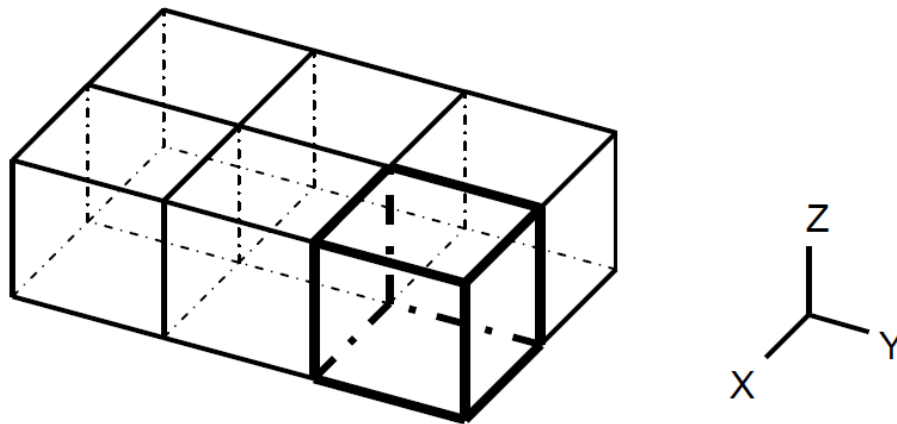


FIG. 2.3: A sample region subdivided into volumetric units called voxels; one voxel is highlighted.

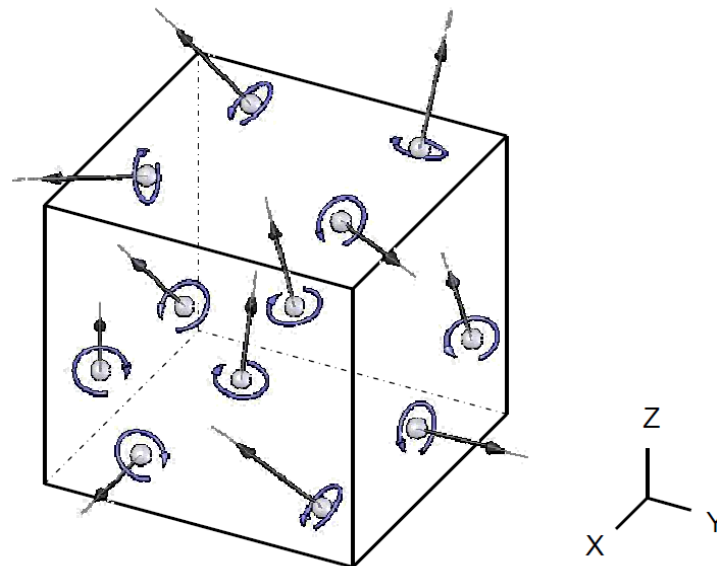


FIG. 2.4: With no external magnetic field present, the individual spin vectors $\vec{\mu}_i$ within a voxel are randomly oriented and do not precess. The net voxel magnetization \vec{M} is zero.

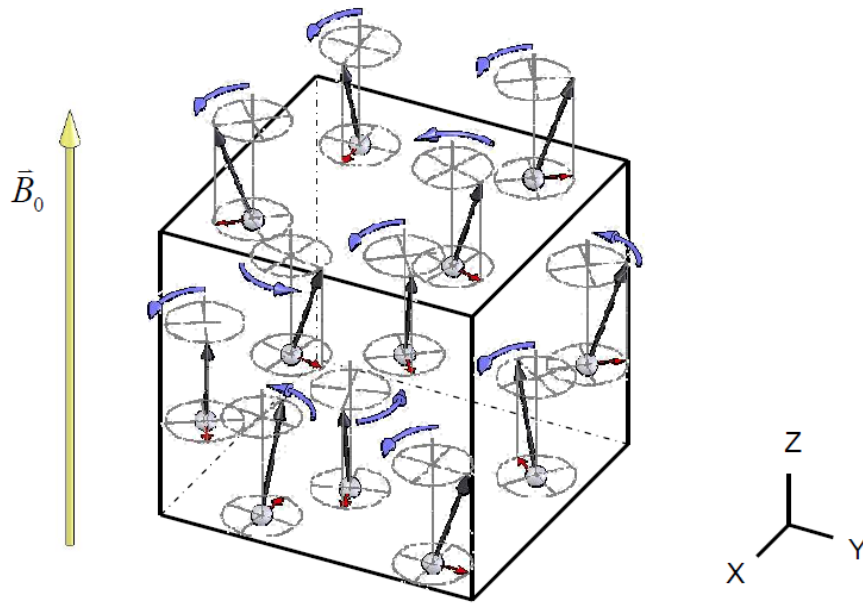


FIG. 2.5: The spins align with an applied external magnetic field \vec{B} and begin to precess; The small black arrows represent the transverse (X Y) components of $\vec{\mu}_i$, and point in all radial directions, so there is no precession phase coherence.

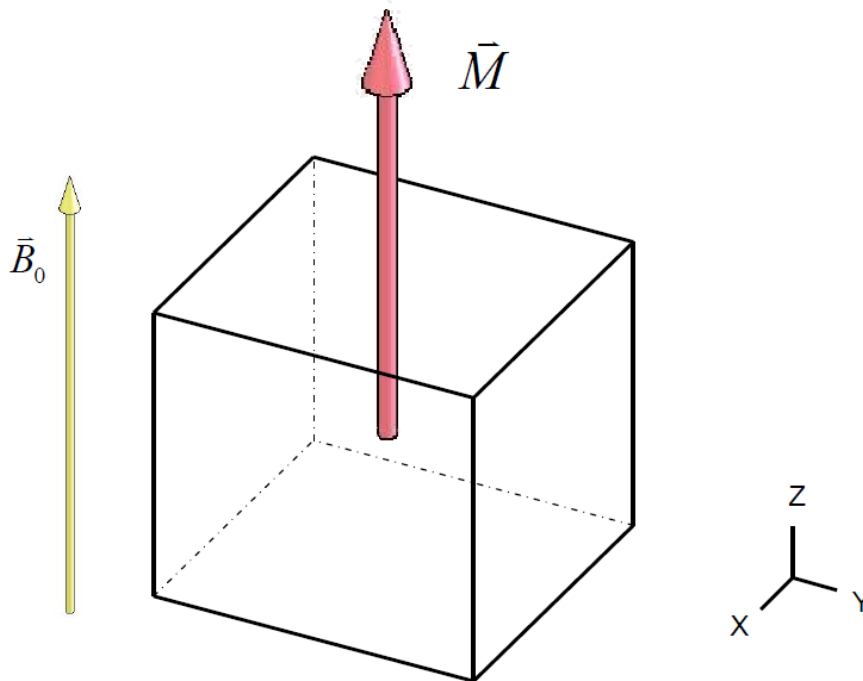


FIG. 2.6: The net magnetization vector \vec{M} results from the vector summation of individual spin moments $\vec{\mu}_i$.

$$\frac{N_{parallel}}{N_{antiparallel}} = 1.0000007 \quad [2.2]$$

[17]. The difference in energy between the parallel (P) and antiparallel (AP) states is proportional to the magnetic field strength. If a nucleus in state P were to absorb a unit of energy (a photon) equal to the energy difference between AP and P , the nucleus could jump to state AP . On a larger scale, if the voxel in Figure 2.5 were irradiated by photons of energy ($AP - P$), many of the parallel spin moments $\bar{\mu}_P$ would ‘tip’ to become antiparallel moments $\bar{\mu}_{AP}$. This would result in a significantly reduced net magnetization magnitude \bar{M} . Due to the dual particle / wave nature of energy, photons are actually electromagnetic fields of a characteristic frequency. In MRI, a radio-frequency (RF) electromagnetic pulse specifically tuned to the Larmor frequency (as given in Equation [2.1]) is applied to ‘tip’ the spins into a higher-energy state [18]. This field is known as the B_1 field (Fig. 2.7). It is the process of energy absorption that is made reference to by the word ‘resonance’ in the term Magnetic Resonance Imaging [19].

The irradiation of a voxel with RF energy, in the environment of a static field, has two important effects upon the nuclear spins [20]. The first has already been described: the magnitude of the net magnetization component \bar{M}_z along \bar{B}_0 decreases (Figs. 2.8 – 2.10). Secondly, the absorbed energy causes the individual proton spins to precess *in phase* with each other. \bar{M} develops a vector component in the transverse plane, perpendicular to \bar{B}_0 . The transverse component of \bar{M} reaches full magnitude by superposition when all the spins precess in phase with each other (Figs. 2.11 – 2.13).

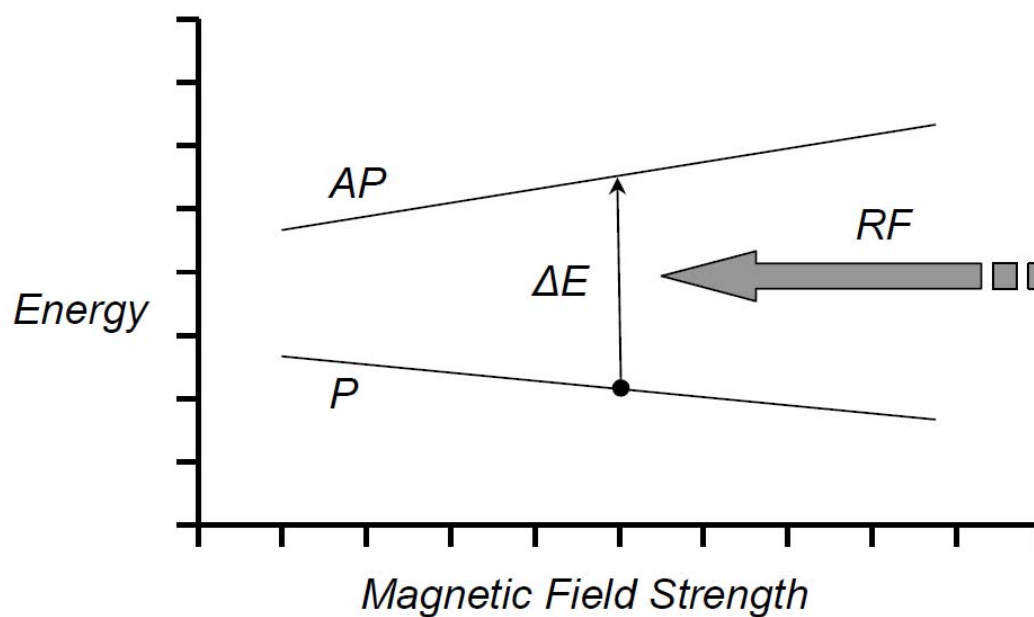


FIG. 2.7: Energy absorption by a nucleus in a parallel state (P) results in a jump in energy to the antiparallel (AP) state. The absorbed energy is provided by an applied RF field, called the B_1 field. The energy difference ΔE is proportional to the strength of the primary magnetic field. Adapted from [18].

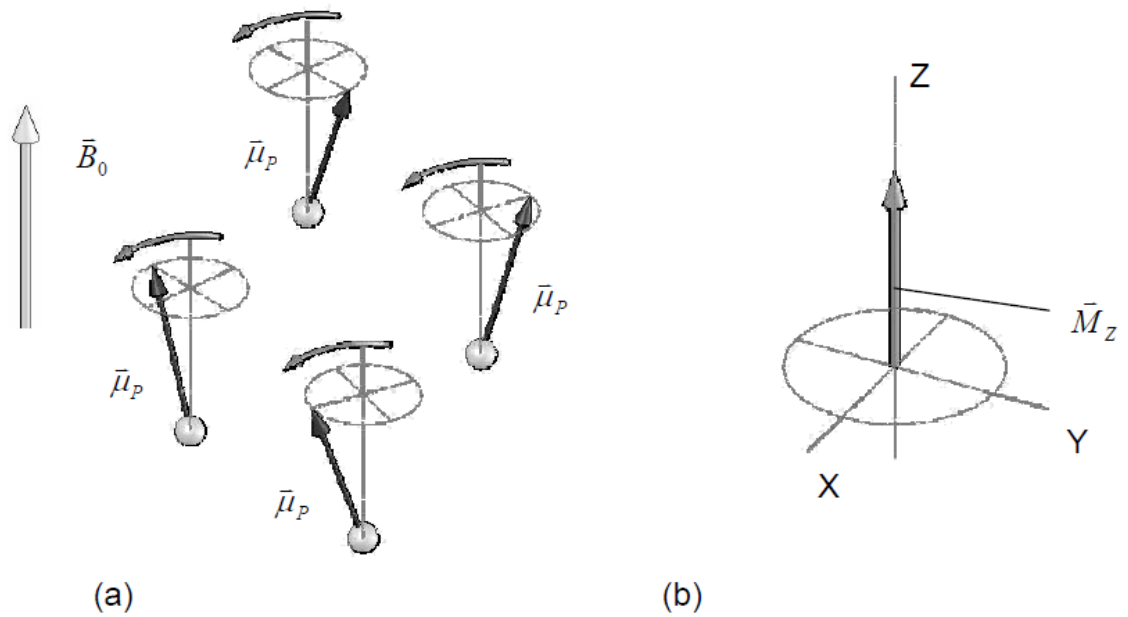


FIG. 2.8: Longitudinal (Z) excitation (part 1 of 3). (a) Precessing spins within a voxel all aligned in the parallel state with applied field \bar{B}_0 . (b) The longitudinal component \bar{M}_Z of the resulting magnetization vector is at full magnitude.

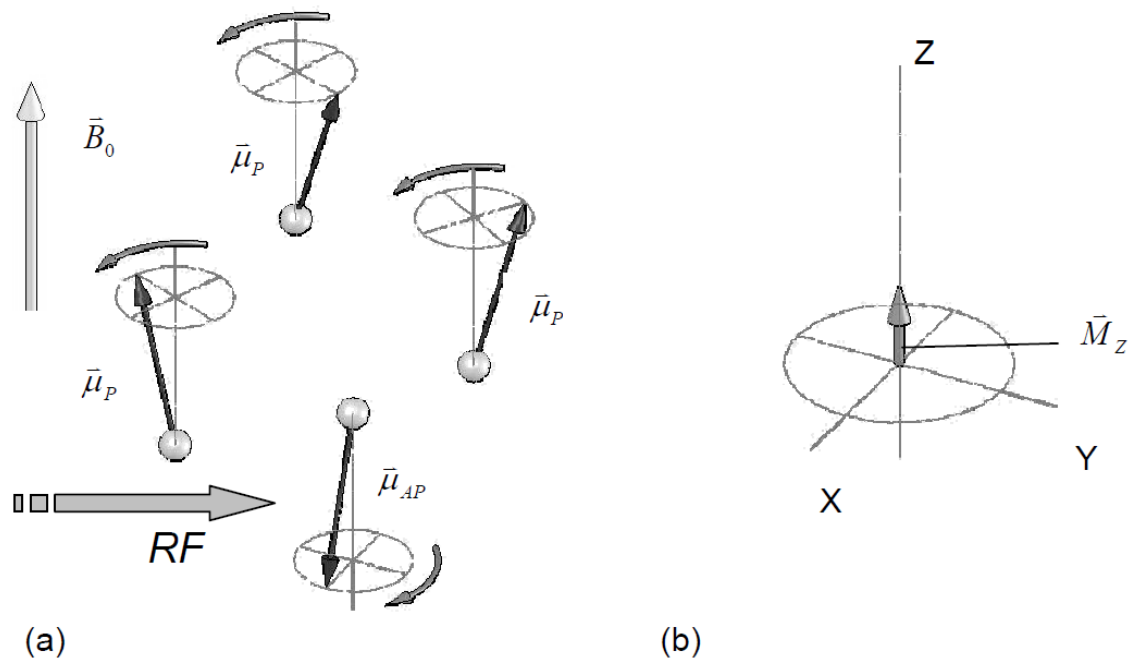


FIG. 2.9: Longitudinal (Z) excitation (part 2 of 3). (a) Absorption of RF energy causes a spin to jump to the antiparallel state. (b) \bar{M}_Z is reduced in magnitude.

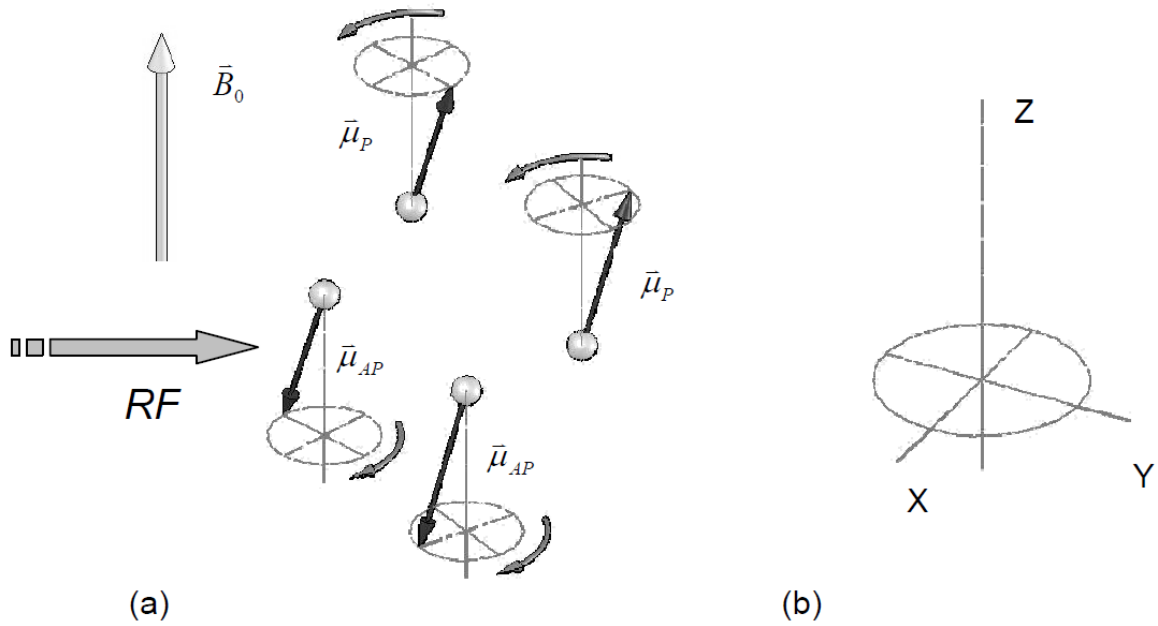


FIG. 2.10: Longitudinal (Z) excitation (part 3 of 3). (a) Continued absorption causes additional spins to jump to the antiparallel state. (b) When $N_{\text{antiparallel}} = N_{\text{parallel}}$, \vec{M}_Z becomes zero by superposition.

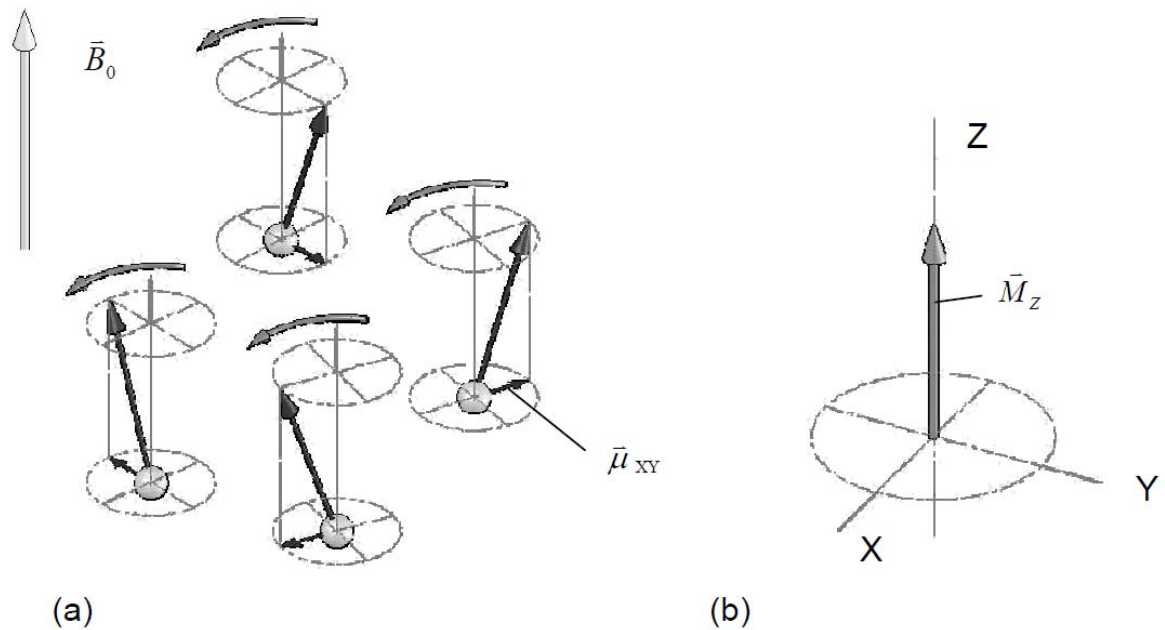


FIG. 2.11: Transverse (X-Y) excitation (part 1 of 3). (a) In an applied field \vec{B}_0 , precessing spins within a voxel have no phase coherence at steady state. (b) \vec{M} has no transverse (X-Y) component.

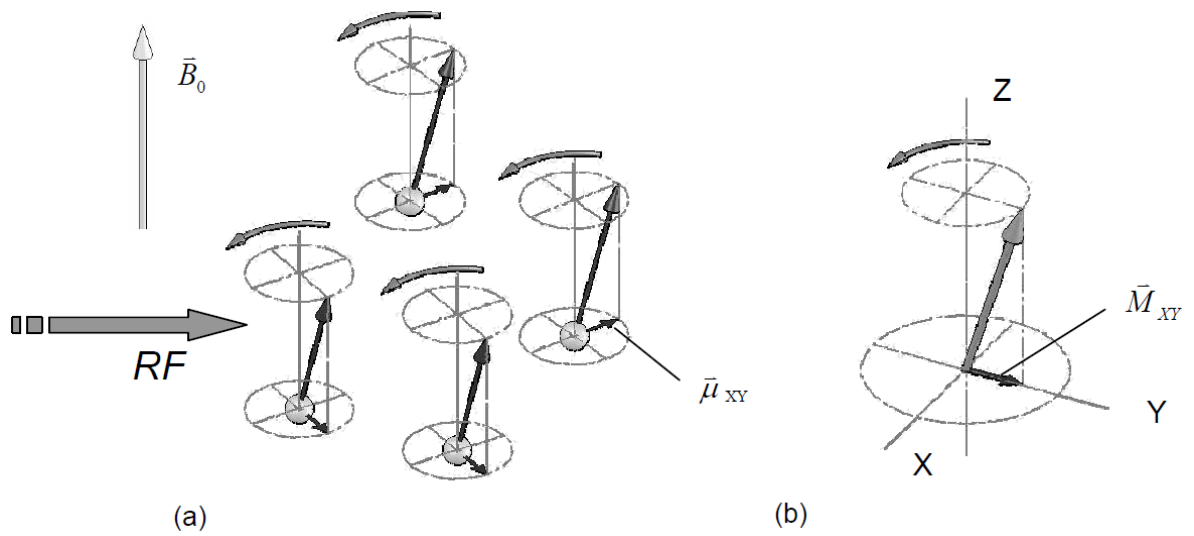


FIG. 2.12: Transverse (X-Y) excitation (part 2 of 3). (a) Introduction of RF energy impels the random spin precession phases into alignment. (b) \vec{M} begins to precess with frequency ω , developing a transverse component \vec{M}_{XY} .

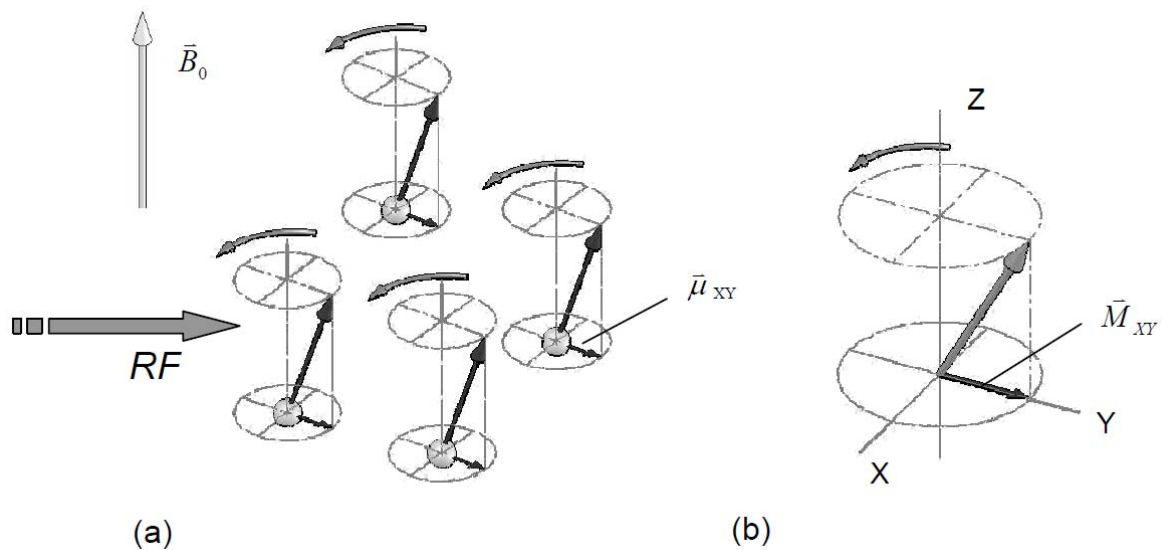


FIG. 2.13: Transverse (X-Y) excitation (part 3 of 3). (a) With additional RF energy the spin phases are fully aligned. (b) \vec{M}_{XY} reaches full magnitude.

The interaction of a static magnetic field with the nuclear magnetic moment of any type of atom is very weak. In fact, the thermal energy of the atom exceeds the magnetic coupling energy by five to seven orders of magnitude [17]. It is the resonance phenomenon, or the coherence (phase alignment) of magnetic fields of the nuclei within the sample, that produces a magnetic disturbance of enough magnitude to be detected. Without the resonance effect, the noise due to random thermal excitations in the sample would overwhelm the minute NMR signal of any single atom.

Immediately after the absorption of RF radiation the excited protons return to their equilibrium state. The precessing spins fall out of phase, reducing the transverse component of \vec{M} to zero. During this time the excess nuclei in the AP state return to the P state, emitting a packet of RF energy in the process. This emitted energy from the relaxation of proton spins is called a *free-induction decay* (FID) signal. Different tissue types relax at different rates, creating unique FID waveforms. The entire ensemble of signals from all the voxels within a volume combine to create a complex waveform, which is detected, deciphered, and finally converted into a visual image. The following step-by-step description summarizes the creation of an FID signal.

(A) Before application of the B_1 RF field, the magnetization vector \vec{M} of each voxel is aligned along Z (the longitudinal axis of the MRI scanner bore, also the direction of the primary field \vec{B}_0); see Figure 2.14.

(B-C) When the B_1 field is introduced, \vec{M} decreases in magnitude along Z and develops a vector component in the transverse (X - Y) plane. The vector \vec{M} itself is tipped through an angle (called the *flip angle*) stipulated by the strength and duration of

B_1 . A flip angle of 90 degrees results in a magnetization solely within the transverse plane (Figs. 2.15 and 2.16).

(D) When the B_1 field is removed, the tipped \vec{M} vector relaxes back to equilibrium. The time required for relaxation along the longitudinal (Z) direction is called T_1 . The decay time of the magnetization component in the transverse plane is referred to as T_2 . T_1 and T_2 differ for each type of tissue within the sample (based on the density of water in the tissue), allowing different tissue types to be identified in the final image that is produced (Fig. 2.17).

2.1.2 The Bloch Equation

The relaxation time constants T_1 and T_2 are two important terms used in the MRI literature for describing voxel magnetization behavior. Their application is governed by the Bloch equation:

$$\frac{d\vec{M}}{dt} = \vec{M} \times \gamma \vec{B} - \frac{(M_z - M_0)\vec{k}}{T_1} - \frac{M_x\vec{i} + M_y\vec{j}}{T_2} \quad [2.3]$$

where \vec{i} , \vec{j} , and \vec{k} represent unit vectors along the X, Y, and Z axes, respectively. The \vec{B} field term includes all the various types of magnetic fields (gradients, etc.) imposed upon the voxel by the scanner [16].

The first term on the righthand side of Equation [2.3] simply represents the precession of the voxel magnetization about \vec{B}_0 , which is dependent upon the

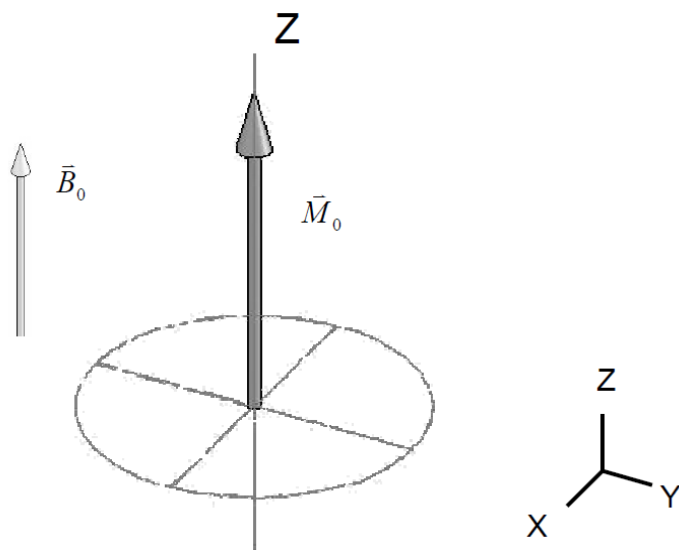


FIG. 2.14: Spin excitation (part 1 of 4). The steady-state magnetization vector \vec{M}_0 is aligned with static field \vec{B}_0 .

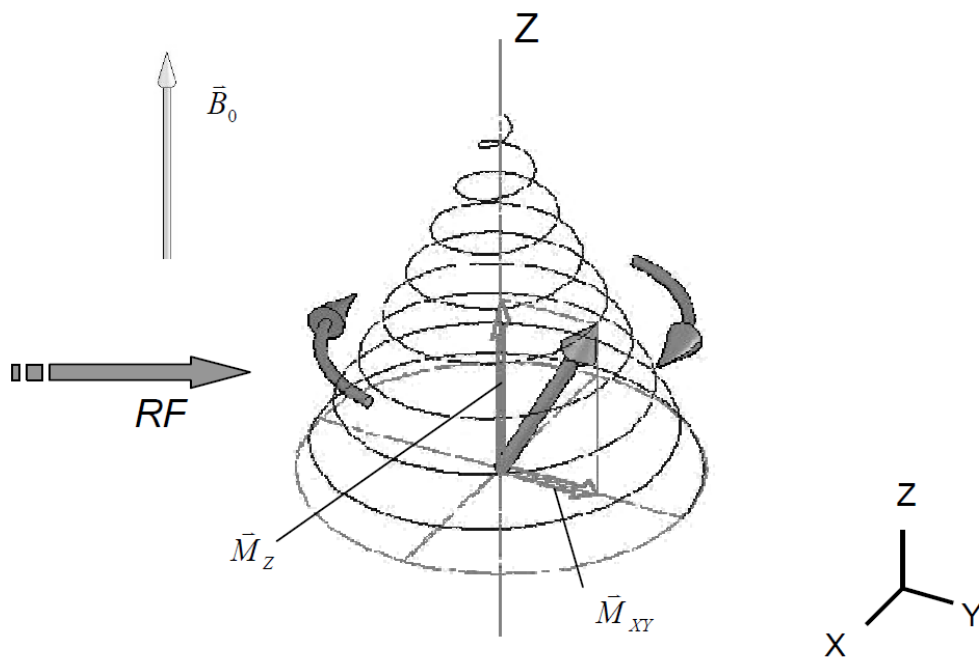


FIG. 2.15: Spin excitation (part 2 of 4). When RF energy is applied \vec{M} begins to precess, developing both a longitudinal component \vec{M}_z and transverse component \vec{M}_{xy} .

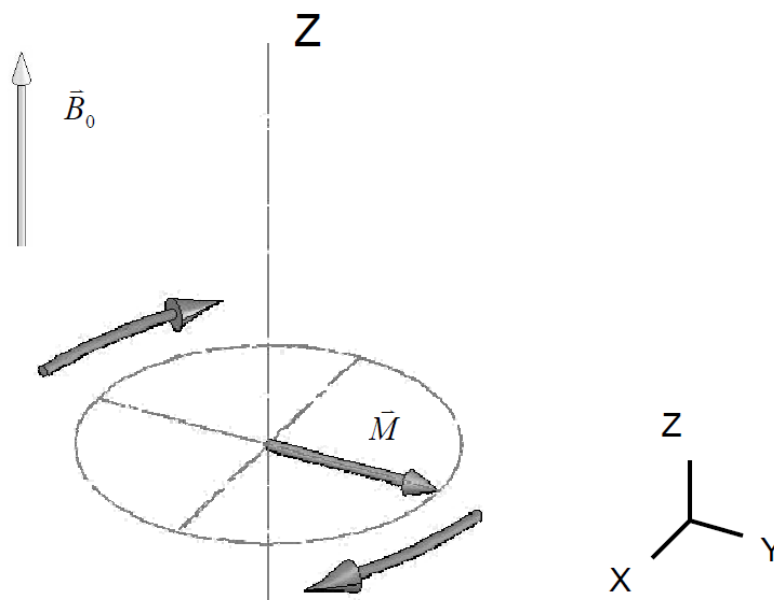


FIG. 2.16: Spin excitation (part 3 of 4). \vec{M} precessing in transverse plane, about the Z axis.

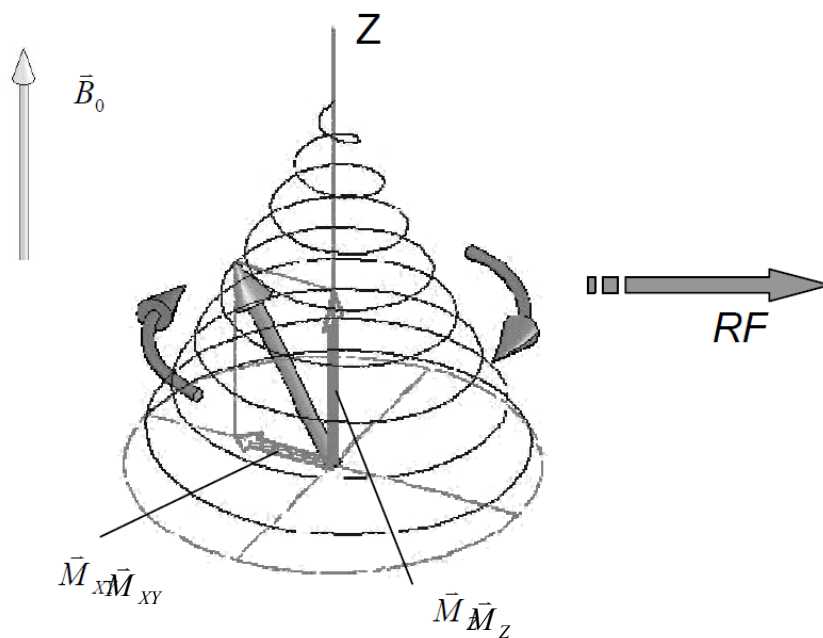


FIG. 2.17: Spin excitation (part 4 of 4). As \vec{M} relaxes, \vec{M}_{xy} and \vec{M}_z return to their steady state magnitudes. RF energy, called the FID signal, is released to the environment.

gyromagnetic ratio term γ unique for each type of atom. The expressions of primary interest in this analysis are the two terms involving T_1 and T_2 . The first of these terms,

$$\frac{d\bar{M}_z}{dt} = -\frac{(M_z - M_0)\bar{k}}{T_1} \quad [2.4]$$

describes the relaxation of the magnetization vector \bar{M}_z from an excited state to the equilibrium magnitude M_0 which was shown in Figures 2.14 – 2.17. A solution to Equation [2.4] is the following [16]:

$$\bar{M}_z = M_0 \left(1 - e^{-\frac{t}{T_1}} \right) + M(0) e^{-\frac{t}{T_1}} \quad [2.5]$$

which mathematically represents the relaxation of \bar{M} and the regrowth of \bar{M}_z . A plot of this function can be seen in Figure 2.18.

Secondly, the term involving T_2 in Equation [2.3] is isolated and given in Equation [2.6]:

$$\frac{d\bar{M}_{xy}}{dt} = \frac{M_x \bar{i} + M_y \bar{j}}{T_2} \quad [2.6]$$

The following is a solution to Equation [2.6]:

$$\vec{M}_{XY} = M_0 \left(e^{-\frac{t}{T_2}} \right) + M(0) e^{-\frac{t}{T_2}} \quad [2.7]$$

Equation [1.7] states that \vec{M}_{XY} tends to decay over time until a steady-state condition of zero magnitude is reached. This expression is plotted in Figure 2.19. There is an interesting difference between the exponential T_1 and T_2 curves of Figures 2.18 and 2.19: \vec{M}_Z lengthens *much* more slowly than \vec{M}_{XY} decays. An important implication of this observation will be explored in detail in Section 2.2 – Faraday’s Law.

2.1.3 MRI Scanner Components

The MRI scanner produces three types of magnetic fields that interact with the proton spins to produce images. Figure 2.20 shows a cut-away view of how the magnets and coils used to create these fields are configured. First, the primary field (\vec{B}_0) is generated by a superconducting coil surrounded by liquid helium (label A, Fig. 2.20). The strength of this field is the primary method of characterizing an MRI scanner (i.e. a 3 Tesla scanner). \vec{B}_0 is the static field directed axially through the scanner bore (the Z axis) that causes spin precession, and consequently, the net magnetization of each voxel. Ideally, the main magnet in the scanner would produce a uniform \vec{B}_0 field throughout the entire imaging volume. Since this is rarely the case in a commercial scanner, ‘shim’ coils (label B, Fig 2.20) are strategically installed to broaden the region of uniformity. The shim coils themselves produce magnetic fields that interact with \vec{B}_0 by superposition to correct known field inhomogeneities [18].

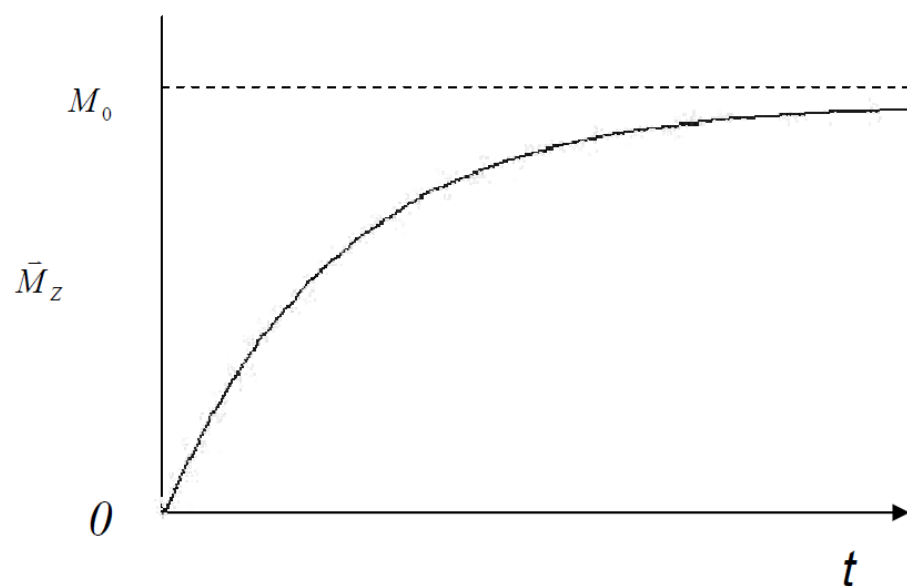


FIG. 2.18: Plot of T_1 relaxation (regrowth of \bar{M}_z) according to Eqn. [2.5].

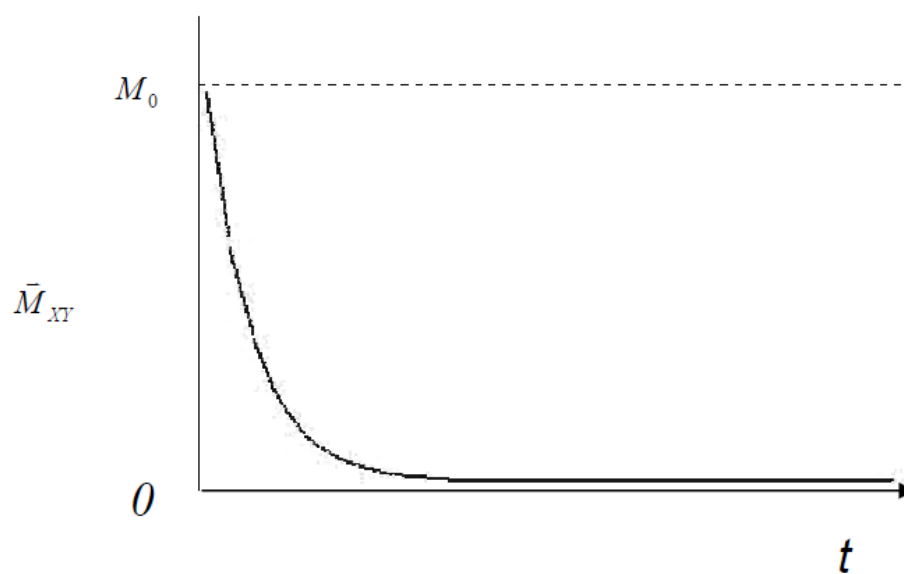


FIG. 2.19: Plot of T_2 decay (decay of \bar{M}_{xy}) according to Eqn. [2.7].

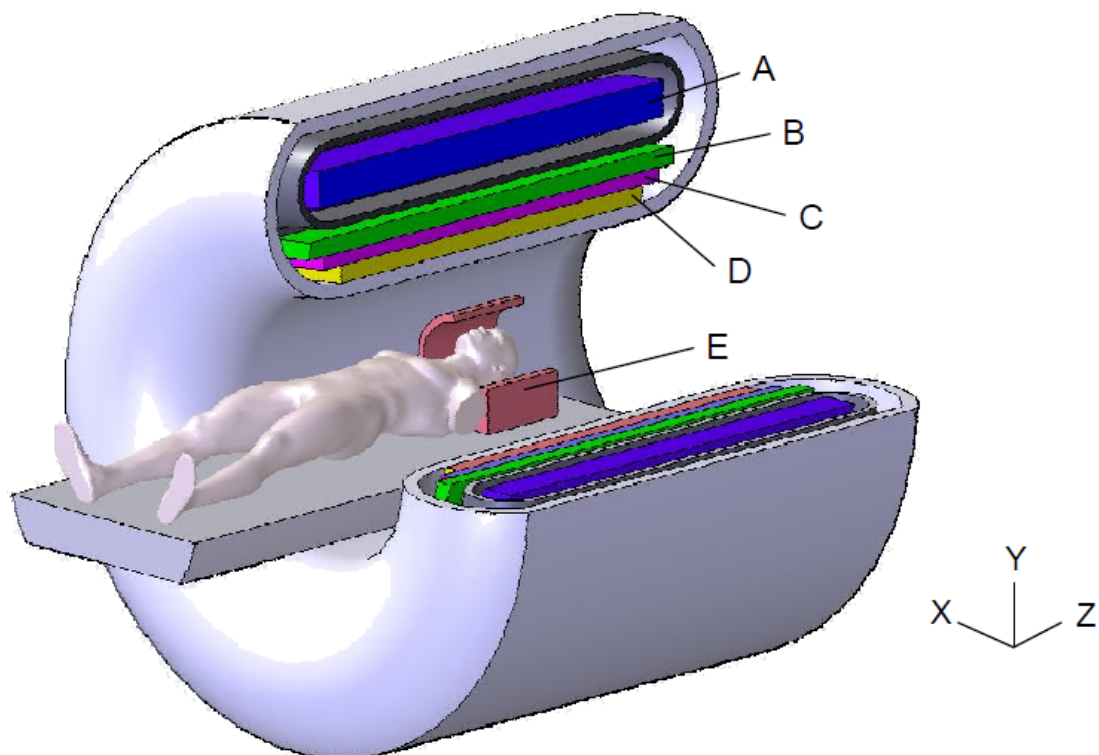


FIG. 2.20: Cut-away view of an MRI scanner. **A:** Primary field (\vec{B}_0) magnet in liquid helium bath **B:** Shim coil **C:** Gradient coil **D:** Body transmit/receive coil **E:** Local transmit/receive coil. Adapted from [21].

The second type of magnetic field applied by the scanner is an RF pulse referred to as the B_1 field. This field is produced by the body coil within the scanner (label D of Fig 2.20) or by a transmit coil local to the imaging volume (label E, Fig. 2.20). The B_1 field is tuned to the Larmor frequency, and temporarily excites the spins of the sample out of their equilibrium state as described in the previous section. Similar to the \vec{B}_0 field, the ideal B_1 field is homogeneous to uniformly excite the nuclei of the entire volume to be imaged.

Finally, the third type of field in the scanner is produced by a specially-designed coil within the scanner called the *gradient* coil (label C, Fig. 2.20). When activated, this coil generates three different gradient fields that combine with the primary \vec{B}_0 field by superposition. Gradient fields establish a nearly linear difference in \vec{B}_0 field strength along the X, Y, and Z axes, throughout the entire scanner bore. Varying the field magnitude in this manner allows signal from different locations in the bore to be ‘spatially coded’ for proper reconstruction into a viewable image.

RF coils (labels D and E, Fig. 2.20) serve two primary roles during an MRI scan. First, a ‘transmit’ coil is used to generate the B_1 field that excites the spins in the sample out of equilibrium. Second, a ‘receive’ coil detects the FID signal of the relaxing spins. Ideally, a receive coil would have a high signal-to-noise ratio (SNR), and would be uniformly responsive to the range of FID signal frequencies produced within the imaging volume. This last provision allows the pixel intensity in the final image to be based upon the tissue type, rather than physical coil construction. Dedicated transmit or receive coils are not required for imaging; a single coil may perform both roles, though such coils are very specialized and not used routinely. The body coil (label D, Fig. 2.20) is generally

the transmit coil of choice during the majority of MRI scanning procedures, due to its large size and homogeneous field pattern [18].

Following the design conditions of an ideal receive coil, two types of local RF receive coils are in common use in MRI systems: the birdcage coil and the surface coil. Birdcage coils provide very homogeneous signal reception of an image volume. However, the SNR suffers when imaging very specific anatomy that is small compared to the total volume. For such an application the surface coil is better suited. The smaller region of sensitivity decreases the amount of noise received from the sample, allowing higher SNR performance of tissue near the sample surface [18]. For this reason, the surface coil was the local receive coil of choice for this thesis.

A surface coil is a resonating combination of inductors and capacitors, commonly called an LC circuit. Resonance occurs when energy alternates between the magnetic fields of the inductors and the electric fields of the capacitors. A resonant circuit of this type is called a “tank circuit,” storing energy in a manner similar to a tank storing water [22]. The fact that a coil is not designed to radiate energy forms the fundamental distinction between an antenna and a coil. Antennas are typically designed to transmit or receive RF energy in the far-field region, whereas coils are designed for transmission or reception of RF in the near-field region. Ideally, only minimal energy within a coil is lost to radiation.

When properly tuned, the LC configuration of a surface coil acts as a pass-band filter to selectively detect the RF radiation emitted by the relaxing spins within the sample. The resonant frequency of a coil must be tuned to the precession frequency of the particular atomic nucleus of interest. As stated earlier, the emitted NMR signal is

very weak. Extreme care must be taken in the design, construction, and placement of surface coils to perform as sensitive a task as FID signal reception.

2.2 Faraday's Law

2.2.1 Derivation of Faraday's Law

Faraday's Law of magnetic induction is fundamental to the theory of MRI. Since every facet of coil design stems from this basic physical principle, it is appropriate that Faraday's Law be derived as it applies specifically to surface coils.

Magnetic flux is defined as the component of an arbitrary magnetic field \vec{B} that is perpendicular to an area of interest. In the case of surface coils, the area of interest is the surface area of the coil itself, represented by the surface vector \vec{S} directed axially to the coil. Flux is represented mathematically as a surface integral over all the magnetic field components of \vec{B} parallel to \vec{S} that pass through the coil:

$$\phi = \int_s \vec{B} \cdot d\vec{S} \quad [2.8]$$

Figure 2.21 shows a coil randomly positioned in a uniform magnetic field \vec{B} . The 'flux' as shown in Figure 2.21 is represented in Equation [2.8] by the dot product.

If the \vec{B} field in Figure 2.21 was not a static field, the changing flux passing through the coil over time would establish a potential difference, or electromotive force (emf), in the coil:

$$V_{emf} = -N \frac{d\phi}{dt} \quad [2.9]$$

where N represents the number of coil loops. N is assumed to be a single turn ($N = 1$) in the case of a surface coil. After substitution of Equation [2.8] for the flux term in Equation [2.9],

$$V_{emf} = -\frac{d}{dt} \int_S \vec{B} \cdot d\vec{s} \quad [2.10]$$

The righthand term can be simplified after considering the most common physical configuration of a coil in the MRI scanner: both the sample and coil typically remain fixed in space while the precessing spins create a time-changing magnetic flux through the coil. Thus, the time derivative applies only to the magnetic field vector \vec{B} :

$$V_{emf} = -\int_S \frac{d\vec{B}}{dt} \cdot d\vec{s} \quad [2.11]$$

The induced emf in the coil causes a current to flow through the coil conductor. The directionality of the current is determined by Lenz's Law, which states that current flows in order to produce a magnetic field which *opposes* the changing flux. The negative sign outside the integral in Equation [2.11] expresses the opposing relationship between current and changing flux.

In a more general sense, an electric field is established in space whenever there is a change in magnetic flux, whether a conductor is present or not. Equation [2.12] quantifies the change in electric field potential around a closed contour C :

$$V_{emf} = \oint_C \vec{E} \cdot d\vec{l} \quad [2.12]$$

The electric field, in turn, produces current flow if indeed a conductor is present. Finally, if the contour of Equation [2.12] encloses a region of changing magnetic flux, then Equations [2.11] and [2.12] can be combined to obtain the integral form of Faraday's Law:

$$\oint_C \vec{E} \cdot d\vec{l} = - \int_S \frac{d\vec{B}}{dt} \cdot d\vec{s} \quad [2.13]$$

In summary, Faraday's Law gives the line integral of the electric field around a closed loop in terms of the rate of change of magnetic flux through the loop [23]. The electric field creates a potential difference, driving a current which generates an induced field. Figures 2.22, 2.23, and 2.24 show the application of Faraday's Law to a surface coil. It is important to realize that the same effect also occurs in reverse. By the principle of reciprocity, the induced field of the coil (the 'transmit' pattern) doubles as the sensitivity region of the coil (the 'receive' pattern) [24]. Figure 2.24 illustrates the field pattern produced by a surface coil using a field simulation in Matlab. Not only does the coil induce the strongest field through the center region (through the enclosed surface area), but the coil is most sensitive to flux through this region as well. In fact, the most important characteristic of a coil – its *sensitivity profile* – is completely determined by the principle of reciprocity applied to Faraday's Law.

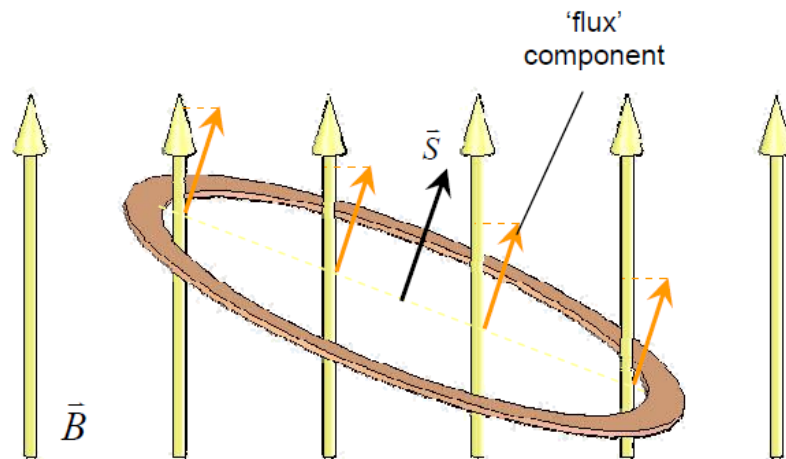


FIG. 2.21: A surface coil in an time-changing magnetic field \vec{B} . Components of \vec{B} parallel with surface vector \vec{S} are known as *magnetic flux*.

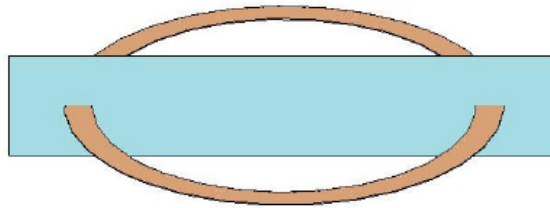


FIG. 2.22: Coil cross-section plane (blue) used in future figures.

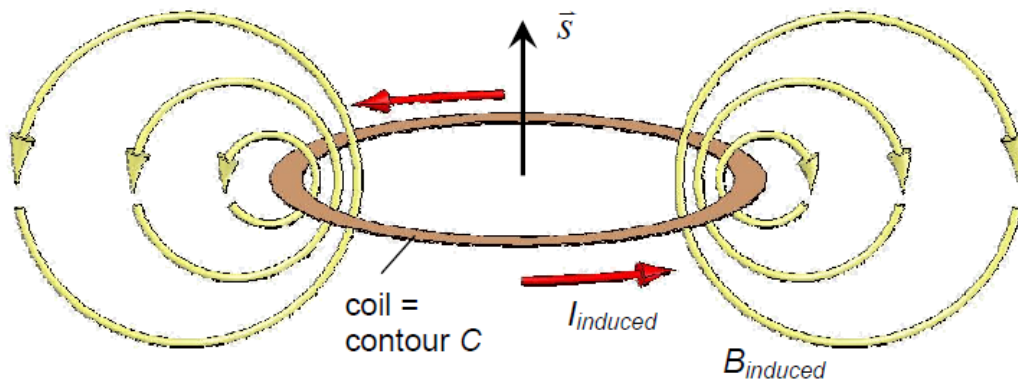


FIG. 2.23: Current I is induced in the coil when the flux of \vec{B} changes with time through contour C . Current I , in turn, induces coil field $B_{induced}$, shown here in cross-section.

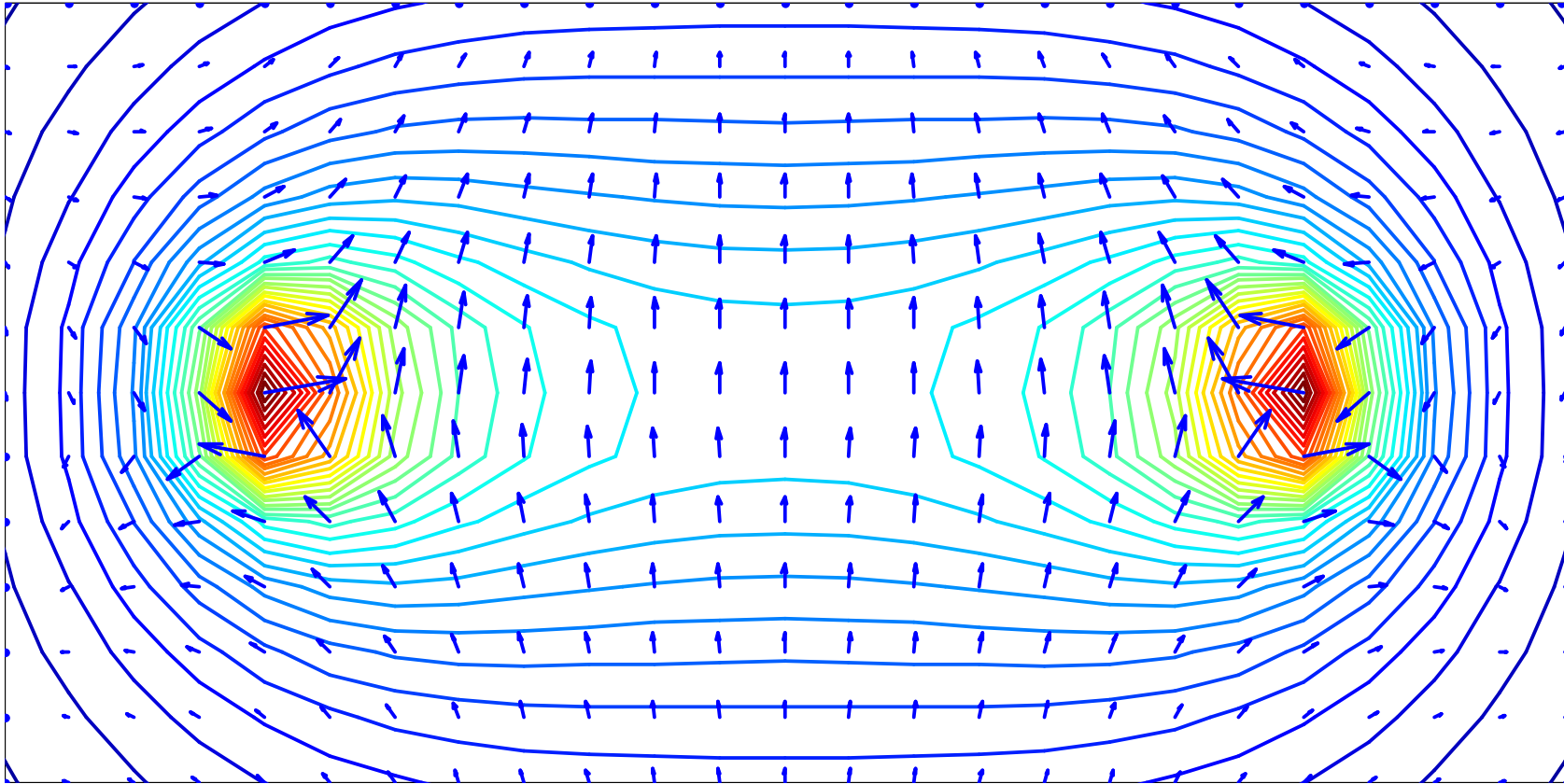


FIG. 2.24: Biot-Savart simulation showing the induced magnetic field of a surface coil, performed in Matlab following [25]. The field vectors (small blue arrows) and magnitude contours (colored lines) demonstrate the high-magnitude induced field through the center of the coil. Relative contour color scale: red = high magnitude, blue = low magnitude.

2.2.2 Coil Orientation

The introductory section of this chapter – 2.1.1 Basic Spin Theory – discussed the nature of the magnetization vector (\vec{M}) of a voxel. When in an excited state, \vec{M} tips into the transverse plane and begins to precess, developing a \vec{M}_{xy} component. The magnetic flux lines produced by precessing spins essentially form the field pattern of a magnetic dipole, similar to that of a small bar magnet (Figs. 2.25 and 2.26). The dipole field approximation is especially valid when considering the orders-of-magnitude difference between the minute nuclear scale and the macroscopic scale of the surface coil.

Figure 2.27 illustrates a surface coil placed into the rotating spin field of Figure 2.26, though *not* to scale. If the surface vector \vec{S} of the coil is aligned with the Z axis, the coil does not detect any changing flux. This fact can be confirmed by imagining a cross-section of the rotating magnetic field through the coil surface. The different flux magnitudes of the field can be viewed where it intersects the coil surface, but due to the rotational symmetry of the field, the field magnitudes do not change in time. Thus, the coil detects no change in flux when oriented in the Z direction. (Actually the flux through a Z-aligned coil changes *very slowly* with T1 relaxation, as plotted in Figure 2.18, but this relatively slow change in time does not produce a useful signal for imaging.)

Figure 2.28 illustrates the same coil after being repositioned orthogonal to Z. Although the coil vector \vec{S} is directed along the Y axis in the illustration, it can be placed in arbitrary orientation within the transverse plane within the same result. In this

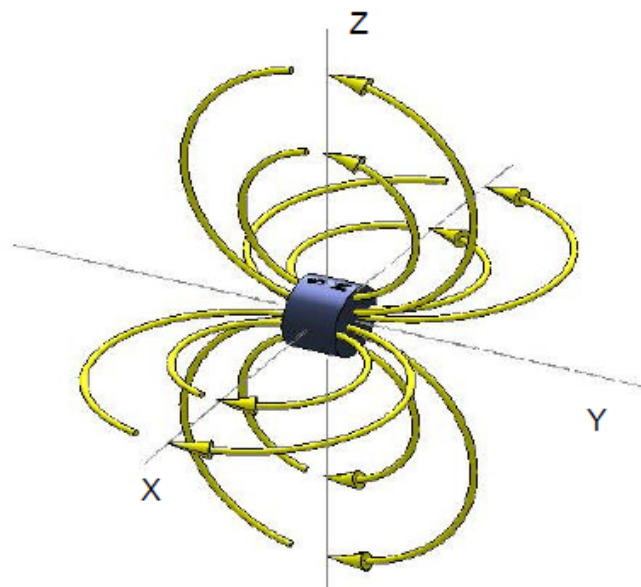


FIG. 2.25: The net magnetization from a voxel produces (approximately) a dipole magnetic field similar to that of a small bar magnet.

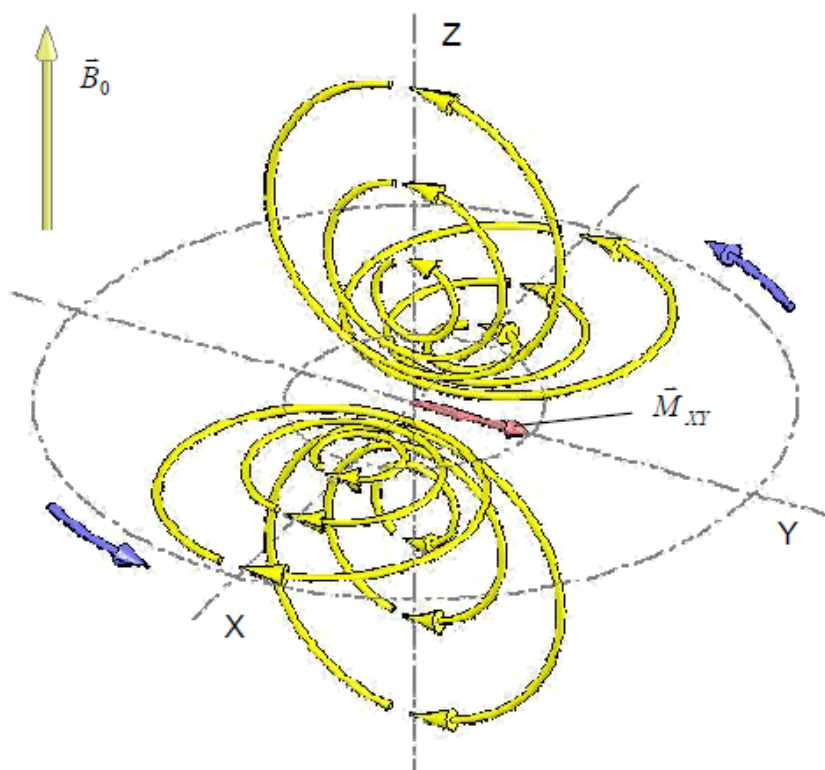


FIG. 2.26: A voxel magnetization vector component (\vec{M}_{xy}) in the excited state, precessing in the transverse plane, producing a rotating dipole field.

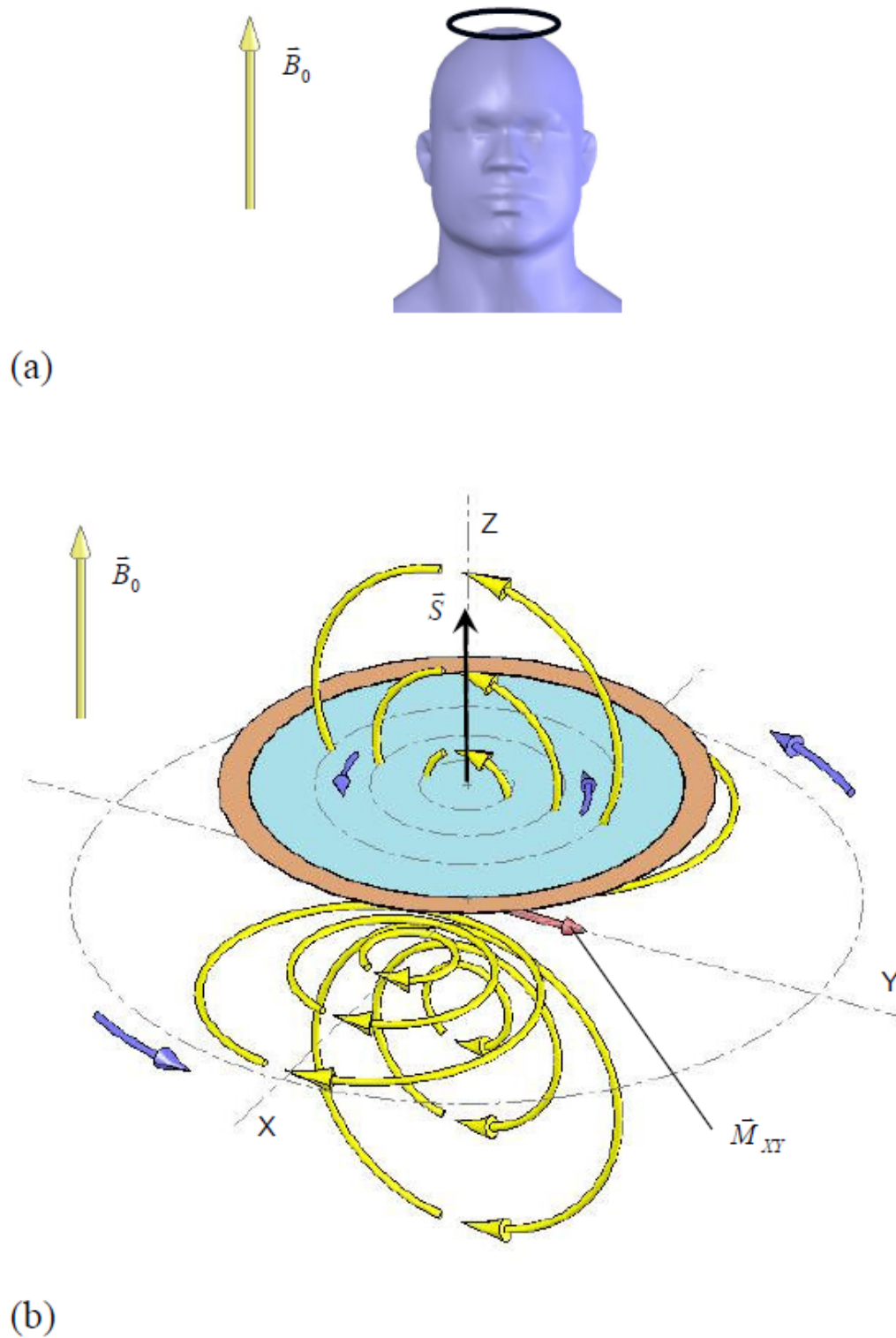


FIG. 2.27: Axially-aligned coil. (a) Coil shown relative to a human lying supine within the scanner bore. (b) In this orientation, a coil receives minimum signal due to nearly constant flux through the coil. The shaded region represents the surface area of the coil.

position, the coil ‘sees’ an alternating positive-negative-positive change in polarity of the magnetic field as the field rotates about the Z axis. The changing flux through the coil surface induces a response in the coil conductor.

In summary, orientation of the receive coil relative to the magnetization vector \vec{M} is an extremely important consideration when designing the layout of surface coils to image specific patient anatomy. The maximum amount of magnetic flux is detected when the coil’s surface vector \vec{S} is contained within the transverse plane.

2.2.3 Coil Cross-sectional Profiles

Imaging a sample through different cross-sectional planes is an important diagnostic feature that is made possible by MRI. The standard imaging planes are entitled *axial* (also called *transverse*), *coronal*, and *sagittal*. Imaging along one of these planes is referred to as taking a ‘slice,’ since the radiologist essentially extracts data from a cross-sectional plane through the sample tissue. During a scan procedure, radiologists often refer to image slices from multiple imaging planes to form a more complete mental picture of complicated anatomy.

The sensitivity profile of a coil can appear to be quite dissimilar in different imaging planes. The terms for the standard imaging planes are given in Figure 2.29. Figure 2.30 shows a coil placed in the transverse plane of a precessing spin field. Here, the coil is now illustrated as rectangular instead of circular to help distinguish the sensitivity profile planes, though the same physical principles apply to either coil shape.

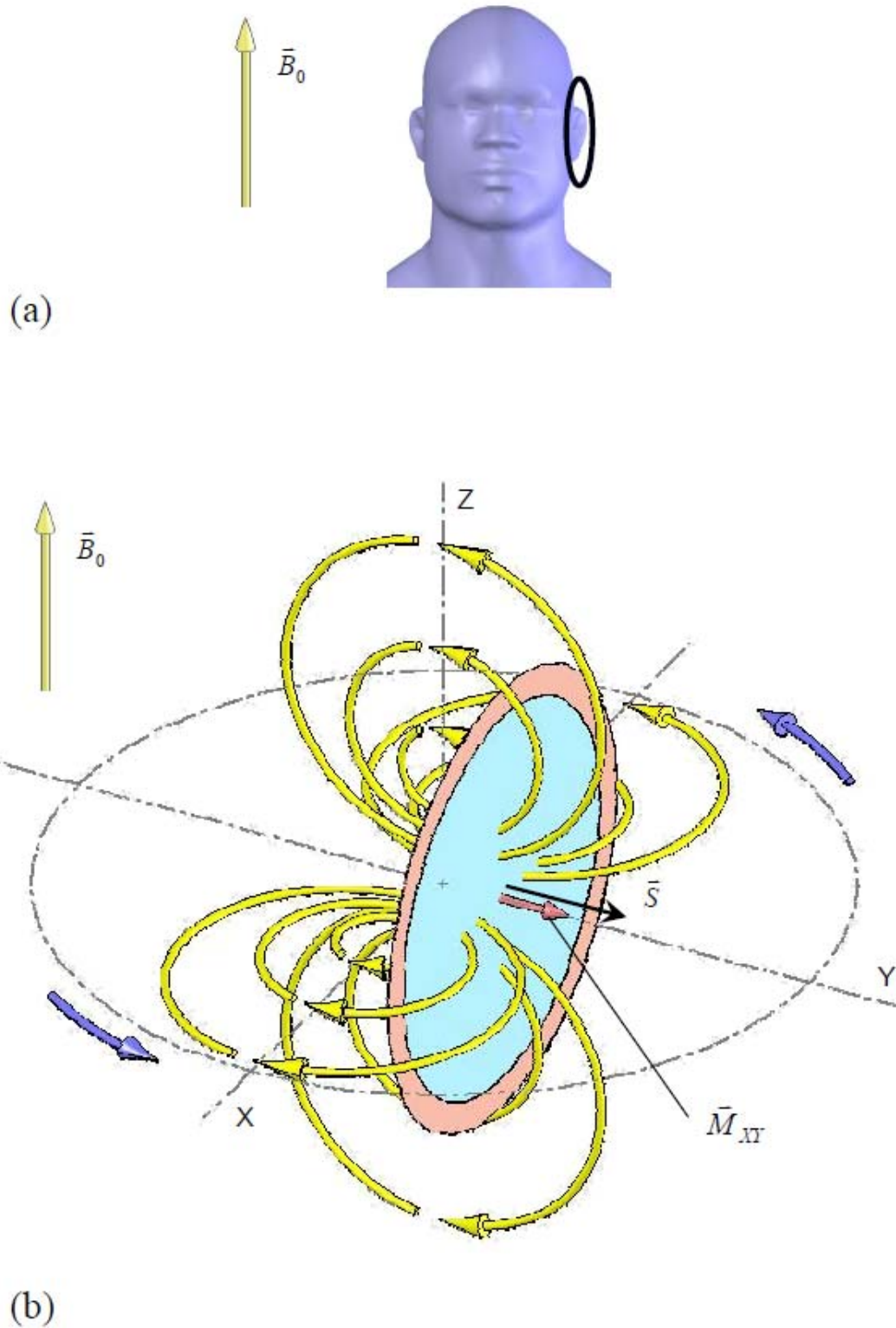


FIG. 2.28: Orthogonal coil. (a) Coil orientation shown relative to a human lying supine within the scanner bore. (b) A coil orthogonal to Z receives maximum signal due to continually-changing flux as \vec{M}_{XY} precesses.

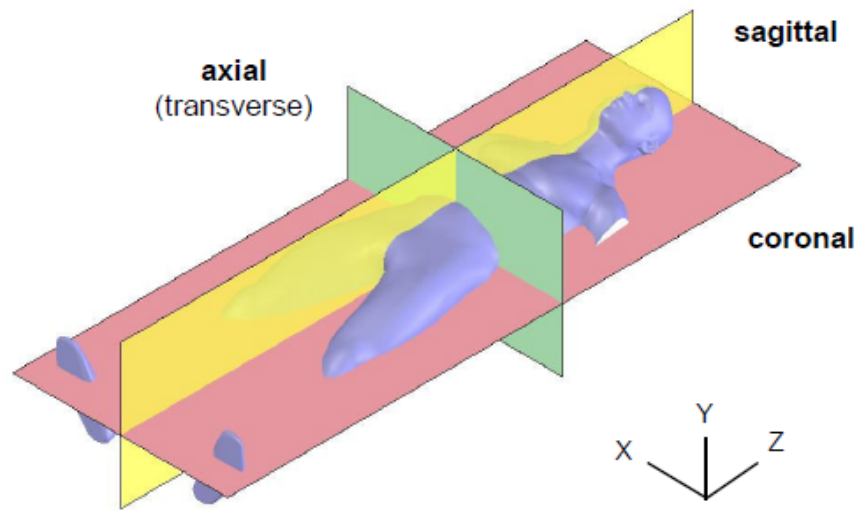


FIG. 2.29: Standard imaging plane orientations shown relative to a supine human as typically encountered in the MRI scanner.

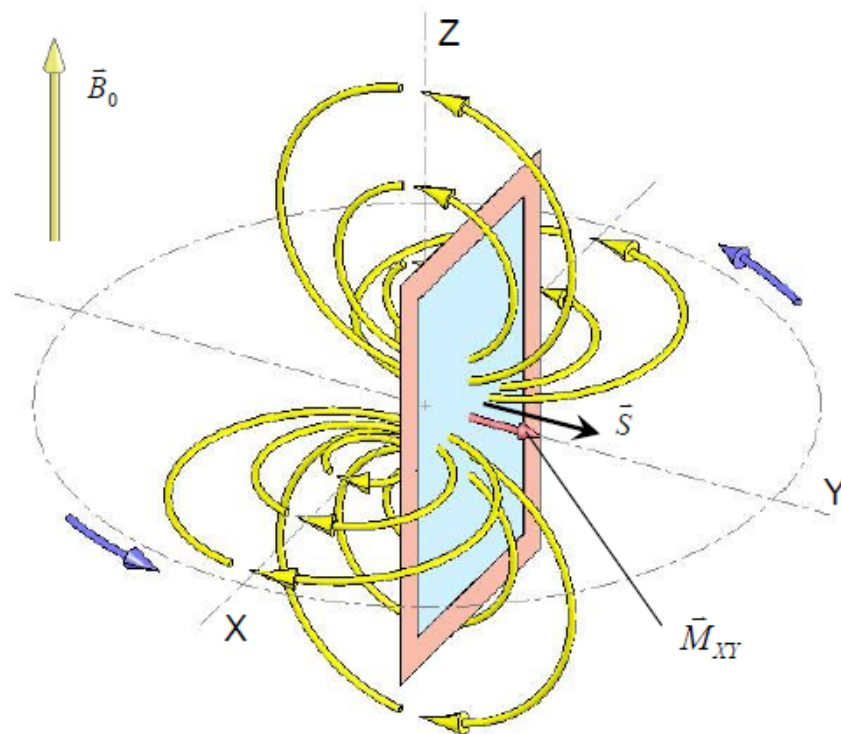


FIG. 2.30: A rectangular coil placed in the field of precessing voxel magnetization \vec{M}_{XY} . Orientation of the primary magnetic field \vec{B}_0 is along Z.

Figure 2.31(a) shows the geometry of a cross-sectional slice through the coil's X-Y plane. Figure 2.31(b) is a Matlab simulation of the sensitivity profile in this plane. As explained before (refer to Fig. 2.28), the flux of the precessing spin magnetization changes maximally through a coil whose surface vector is oriented in the X-Y plane. The profile of Figure 2.31(b) would appear the same for a similar X-Y planar cross-section through the coil offset by any Z-axis distance. Figure 2.31(c) shows an SNR intensity image from a rectangular coil through the X-Y plane; note the field drop-off similarity between Figures 2.31(b) and 2.31(c).

In Figure 2.32(a) the same coil geometry is maintained, but the imaging plane is flipped by 90 degrees into the Y-Z plane. The resulting Y-Z sensitivity profile was simulated to produce Figure 2.32(b). An interesting anomaly occurs in the profile: it would seem that the coil is not sensitive to signal in certain 'signal shadow' regions, for the field magnitude in these regions is significantly reduced. One might question why this situation is different from that shown in the previous figure, where the slice is taken through the X-Y, since the equivalent amount of flux is passing through the coil in either case. The fact is that the coil is only sensitive to *changing* flux. Flux from the precessing spin magnetization continually changes in magnitude in the X and Y directions, but not in the Z direction. Hence, the field pattern is uniform in X and Y, as seen in Figure 2.31(b). However, flux in the Y-Z plane changes only along Y. Thus, the signal shadow regions represent areas where there is little or no change in flux at all: Z-varying flux does not exist, and the coil's sensitivity to Y-varying flux has naturally diminished anyway following the $\frac{1}{y^2}$ decay of the Biot-Savart law, as in the X-Y profile.

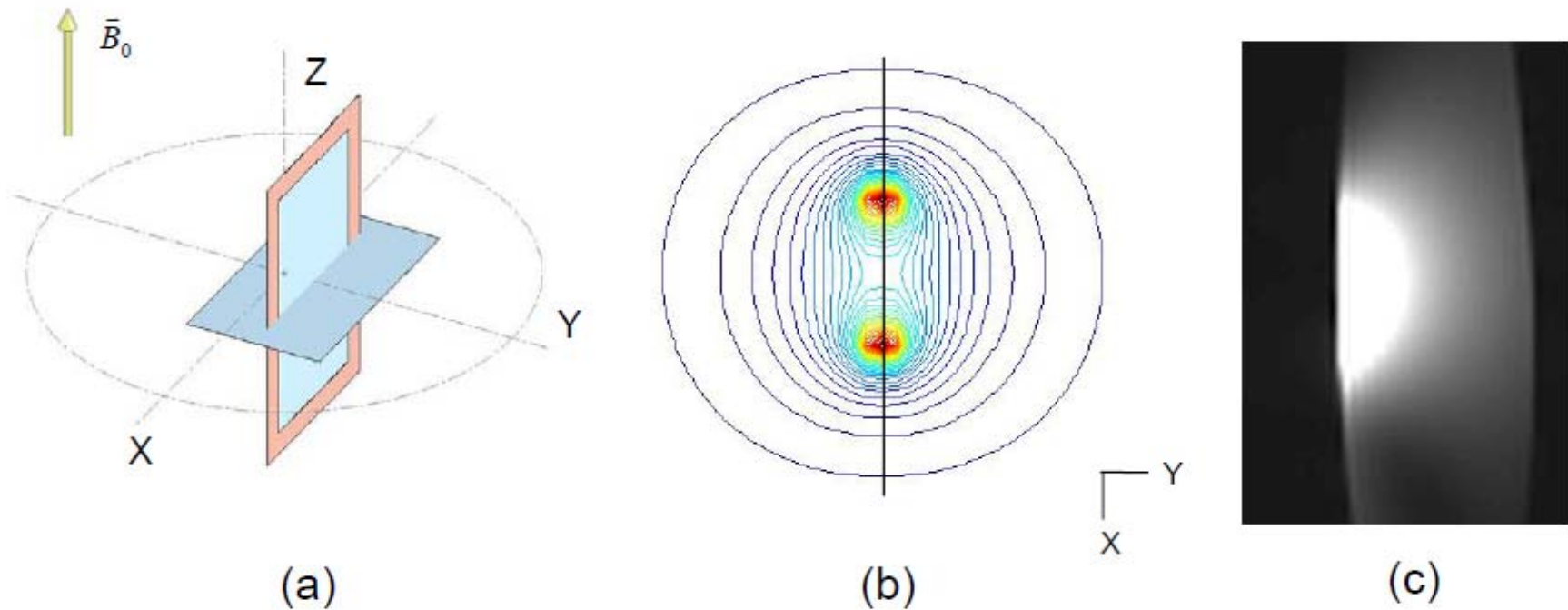


FIG. 2.31: Axial scan plane (orthogonal to scanner bore). (a) Simplification of Fig. 2.30 showing X-Y profile plane. (b) Simulated sensitivity profile in X-Y plane (relative scale: red = highest magnitude, blue = lowest magnitude). (c) Scan image of a coil placed on a conductive phantom, confirming the sensitivity profile of (b).

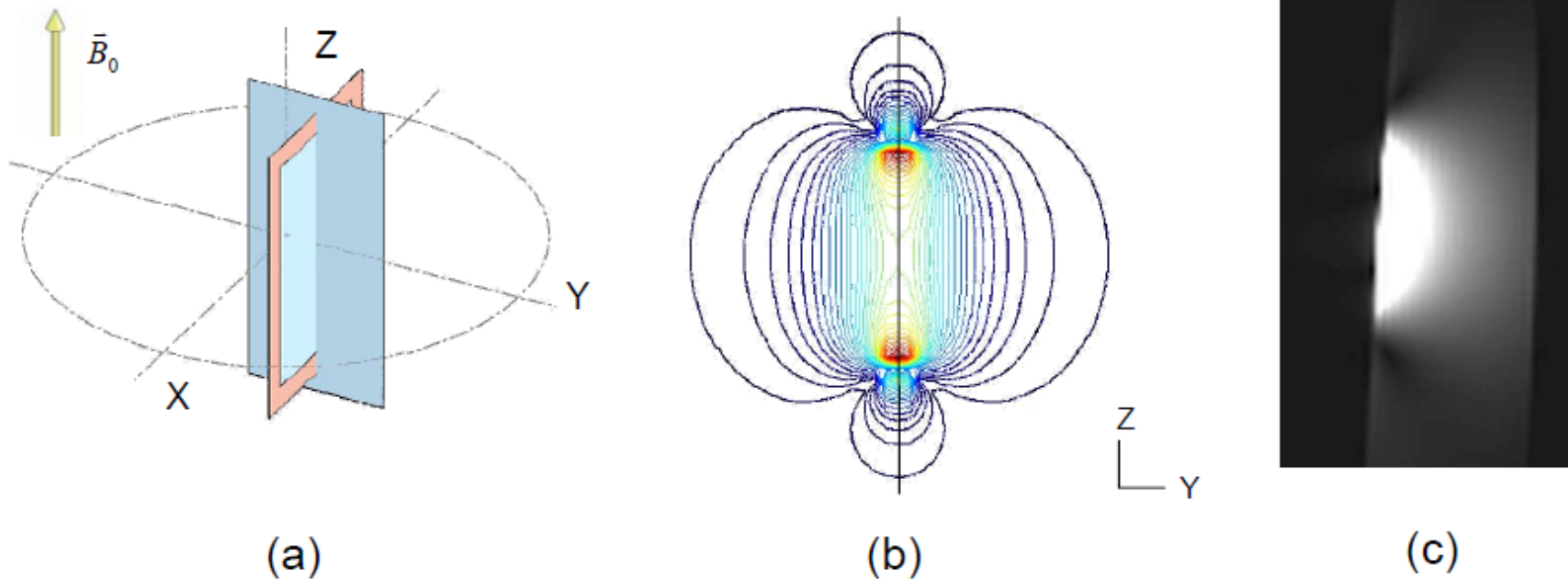


FIG. 2.32: Sagittal or coronal scan plane (parallel to scanner bore). (a) Simplification of Fig. 2.30 showing Y-Z profile plane. (b) Simulated sensitivity profile exhibiting shadow regions (relative scale: red = highest magnitude, blue = lowest magnitude). (c) Scan image of a coil placed on a conductive phantom, confirming the sensitivity profile and shadow regions.

The field simulations of Figures 2.31(b) and 2.32(b) were performed in Matlab using a special application of the Biot-Savart Law to rectangular coils [25]. A test coil was constructed and imaged in the MRI scanner to produce Figures 2.31(c) and 2.32(c), with a homogeneous phantom used as the imaging sample.

When engineering a coil array, the sensitivity profile of each coil in various imaging planes is a crucial design consideration. The full significance of this concept will be elucidated in Section 2.4, which deals with coil overlap decoupling in a phased array.

2.3 Coil Performance

Constructing a surface coil involves much more than simply placing a conductive loop in a region of changing magnetic flux. Usually considerable time, effort, and resources must be invested into preliminary research of construction designs and procedures. This section describes several methods that are used on the test bench to characterize the performance of coil components and configurations during the construction process. These techniques and measurements are essential for determining the coil's proper response to electromagnetic stimulation. Additionally, several coil properties will be discussed that ultimately influence the coil's achievable SNR.

2.3.1 Quality Factor

Quality factor (Q) is an industry standard metric for describing the resonant characteristics of an oscillating system. Since resonance is universally applicable to nearly every engineering discipline, Q has been adopted into these diverse fields of study,

including structural design, mechanics, optics, acoustics, and electronics. Indeed, it is encountered frequently in the MRI literature as a method of comparing coils of dissimilar designs.

In simple terms, the Q of an oscillator refers to the speed at which the oscillations die out. Different rates of oscillation decay are desirable in various circumstances. In the case of a pendulum system, such as a grandfather clock, a very high Q is required for the clock to maintain accurate time. On the other hand, a car ride would be very uncomfortable if, after every bump in the road, the car's shocks encouraged oscillation rather than absorbing it. In regards to MRI, an imaging coil is designed to function as an energy storage device. Oscillations are maintained in the form of alternating magnetic and electric fields. Quality factor is employed in coil engineering to measure the energy storage performance, or 'tank circuit' capacity, of a resonant coil [22]. Equation [2.14] mathematically describes Q:

$$Q = \frac{2\pi \cdot \text{max instantaneous energy stored in circuit}}{\text{energy dissipated per cycle}} \quad [2.14]$$

Alternately, Q can be given as a ratio of the *reactance* of a coil to the coil *resistance (r)* at resonance:

$$Q = \frac{\omega L}{r} \quad [2.15]$$

The reactance term ωL in the numerator of Equation [2.15] represents the coil's 'opposition' to induced currents, specifically the rapidly-alternating currents induced by the precessing spins in the sample. The reactance of a coil is important because it describes how the coil responds to stimulation at various frequencies. The coil's induced magnetic and electric fields 'ramp up' and 'ramp down' as current flows and charge accumulates. In other words, it might be said that magnetic and electric inertia must be overcome during each cycle of coil resonance. The value of Q specifies how responsive the circuit is to resonance at a given frequency and to what degree that response falls off over a given bandwidth. A coil with high Q resonates with large amplitude over a very small range of frequencies. Inversely, a low-Q coil resonates poorly over a large bandwidth.

The Q of a coil is based upon the speed at which magnetic and electric fields are established around the coil. Since these fields pass through the imaging sample, the conductivity, or *load*, of the sample significantly affects the coil Q:

$$Q_{unloaded} = \frac{\omega L}{r_{coil}} \quad [2.16]$$

$$Q_{loaded} = \frac{\omega L}{r_{coil} + r_{sample}} \quad [2.17]$$

In an unloaded state, the only resistance affecting a coil is the internal resistance of the coil conductor and the coil's various electronic components (r_{coil}). Thus, according to Equation [2.16], a *high* Q value describes a coil a very small coil resistance.

In this condition the coil has a sharp, narrow frequency selectivity, which is desirable for a coil in the unloaded state.

When a coil is placed near, or ‘loaded’, with a conductive sample, the coil’s various fields interact with the charged ions within the sample. This interaction can be represented by the equivalent resistance term r_{sample} in Equation [2.17]. A low Q_{loaded} usually indicates that r_{sample} is producing a greater loading effect upon the coil than r_{coil} . While this condition is not always true, it is a desirable trait making the coil *sample-noise dominated* rather than *coil-noise dominated*. Should the opposite case be true (i.e., if the coil were coil-noise dominated), the performance of the coil would be very poor because the noise magnitude from the coil itself would prevail over the signal generated by the sample. Very small coils typically suffer from the problem of an increased coil resistance.

The *sensitivity* of a coil takes both the unloaded and loaded conditions into account by the ratio:

$$sensitivity = \frac{Q_U}{Q_L} \quad [2.18]$$

Sensitivity is typically measured using two inductive pick up loops and a network analyzer (see Fig. 2.33). The loops must be small compared to the diameter of the coil under test, and must be placed far enough from the coil to be only loosely coupled to the coil and minimally coupled to each other. The loops are positioned on opposite sides of the coil, one loop functioning as transmitter and the other as receiver, and both are connected to the network analyzer [26]. Power transmission through the resonant coil is

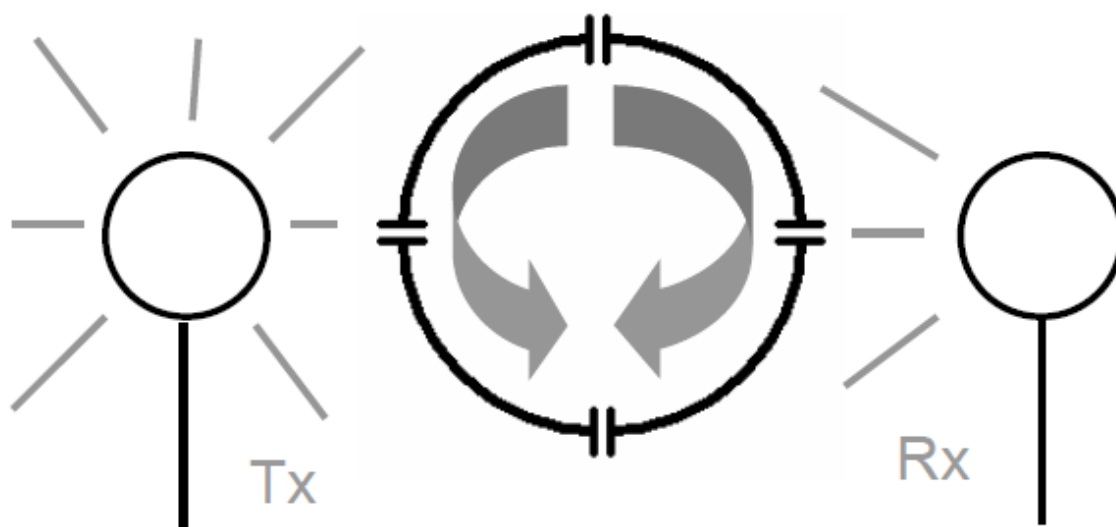


FIG. 2.33: A typical probe arrangement for conducting Q measurements; transmit (Tx) and receive (Rx) probes are placed on either side of a resonating coil, measuring the magnitude of energy transmission through the resonating coil.

measured for both the unloaded and loaded states to obtain the Q_U and Q_L values needed for Equation 2.18.

Quality factor measurements played an important role in the design of the optic nerve coil. These measurements influenced the selection of the construction material and components, since the Q of individual component affects the quality factor of the entire coil assembly [27]. Chapter 3.1 of this thesis, entitled Preliminary Work, will explain how specific coil components were chosen using Q and sensitivity measurements.

2.3.2 S-parameters

Scattering ('S') parameters are used in electromagnetic theory to measure the propagation of RF energy through a network containing multiple input and output ports. Mathematically, S-parameters are arranged in the form of a scattering matrix. If a network has N ports, the number of elements in the scattering matrix will be N^2 , representing all possible permutations of RF energy reflection and transmission through the network. The two-port matrix is referred to frequently in coil design:

$$\begin{pmatrix} S_{11} & S_{12} \\ S_{21} & S_{22} \end{pmatrix} \quad (two - port) \quad [2.19]$$

The diagonal elements (S_{11} , S_{22}) of the Equation [2.19] are known as the *reflection* coefficients. By way of illustration, suppose a coil were connected to a network analyzer via a length of cable, as shown in Figure 2.34. From the reflection port (port 1) the network analyzer sends out RF energy at all frequencies within a certain bandwidth, called the frequency 'span'. At the same port, the reflected power magnitude

of each respective frequency is measured. This type of measurement is called an S_{11} measurement; an example screenshot from this setup is shown in Figure 2.35. Note that the frequency span forms the X axis of the display, and the reflected power magnitude forms the Y axis.

Figure 3.35 is best understood by remembering the ‘tank’ circuit property of a coil, meaning the coil stores energy at a particular frequency of resonance. Although RF energy of all frequencies within the span is incident upon the coil, only those frequencies very near the resonant frequency are significantly absorbed by the coil. All other frequencies are rejected and sent back to the network analyzer by reflection. Since the reflection port of the analyzer measures *reflected* energy, rejected frequencies (see point ‘A’) show up as high magnitude data points, while absorbed frequencies (point ‘B’) appear as low magnitude points. Of particular interest is the frequency of highest absorption, or resonant frequency of the coil, often called the coil *tune*. Another important property called the *match* of the coil, or the degree to which energy from the cable is coupled into the coil, can be qualitatively determined by the depth of the resonance ‘dip’. (Note: A Smith Chart display is usually better suited for quantitative match determination.) The depth of the resonance dip has a more standard name called *insertion loss*, referring to the amount of inserted energy that is *lost to* (or absorbed by) the coil.

The off-diagonal elements (S_{12} , S_{21}) of the S matrix in Equation [2.19] are called the *transmission* coefficients. Transmission properties of a coil are measured by connecting probes to both ports of the network analyzer, as shown in Figure 2.36. As

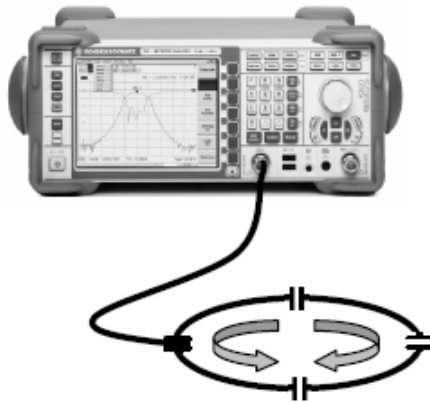


FIG. 2.34: Measurement of S_{11} : surface coil connected to the reflection port of the network analyzer.

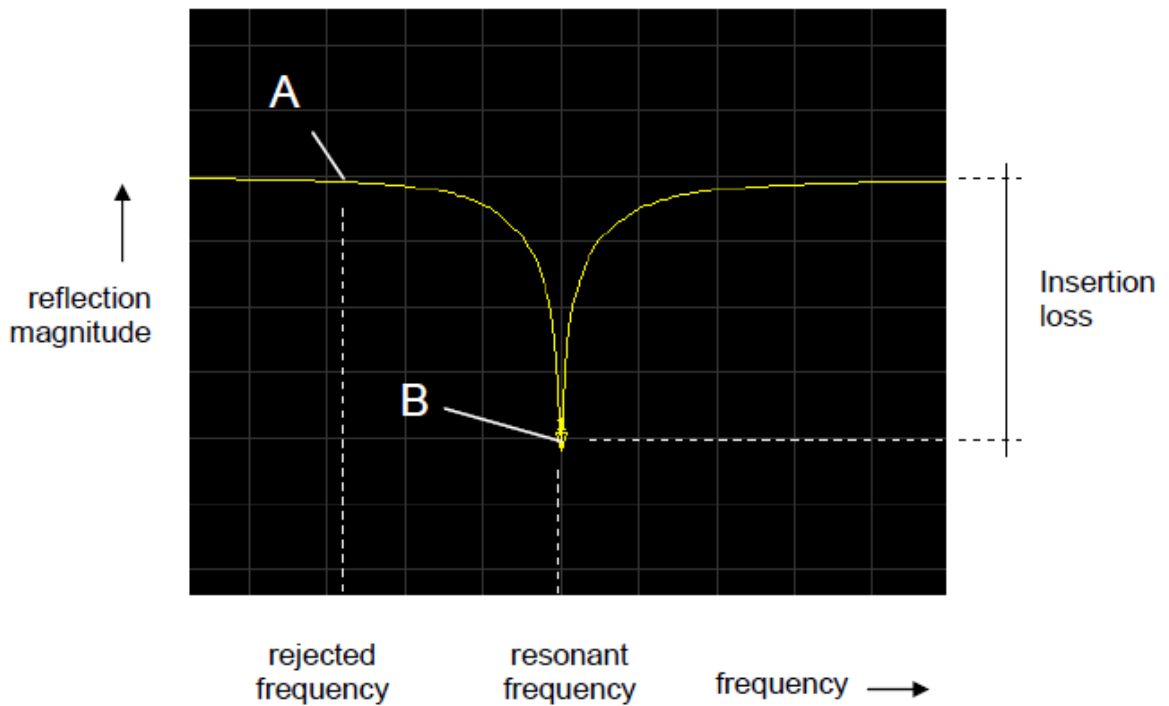


FIG. 2.35: Network analyzer screen snapshot showing an S_{11} curve from the coil configuration of Fig. 2.34. Most energy reflection occurs at nonresonant frequencies such as point 'A', while the most energy absorption occurs at the resonant frequency (point 'B').

before, the analyzer sends out energy at all frequencies within the span from the *reflection* port. This energy is uniformly broadcasted by the probe labeled ‘Tx,’ but only energy of frequency matching the coil’s resonant frequency is absorbed by the coil. The Rx probe, in turn, detects the strong magnetic field produced by the resonating coil, and transfers this energy back to the analyzer through the *transmission* port. Thus, in the case of transmission measurements, the network analyzer display is reversed from reflection mode (see Figure 2.37). Only the energy near the resonant frequency is transferred through the system (point ‘B’), while the energy of all other frequencies is lost to the environment (point ‘A’).

In summary, S-parameters play a crucial role in coil construction. The network analyzer’s capability to graphically represent S-parameters is ideal for measuring the many important characteristics of a surface coil. Not only are coil Q properties measured in this manner, but also many other operations such as coil-to-coil overlapping and decoupling, which will be discussed in Sections 2.4 and 2.5.

2.3.3 Electric Fields and Coil Noise

Faraday’s Law was derived in Section 2.2 with a particular focus on the generation of a coil’s induced magnetic field. However, the generation of a coil’s electric field is of considerable interest as well, especially when studying the factors that contribute to a coil’s SNR. Equation [2.13] illustrated how an electric field forms a closed loop around any region of changing magnetic flux. In the case of MRI, this changing flux is due to the precessing spin magnetizations. The electric field induced by this changing flux causes electric charge to flow within the nearby coil conductor, which

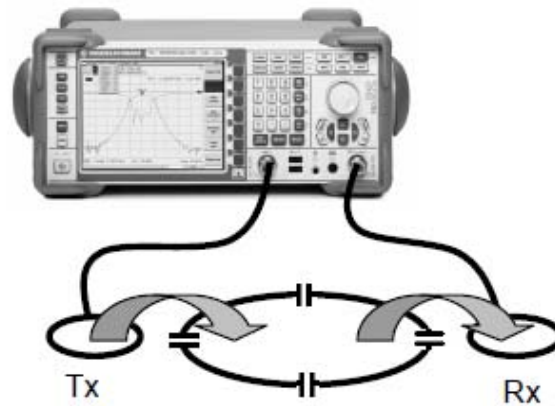


FIG. 2.36: Measurement of S_{21} : probes connected to both ports 1 and 2 allow the measurement of energy transfer through the coil.

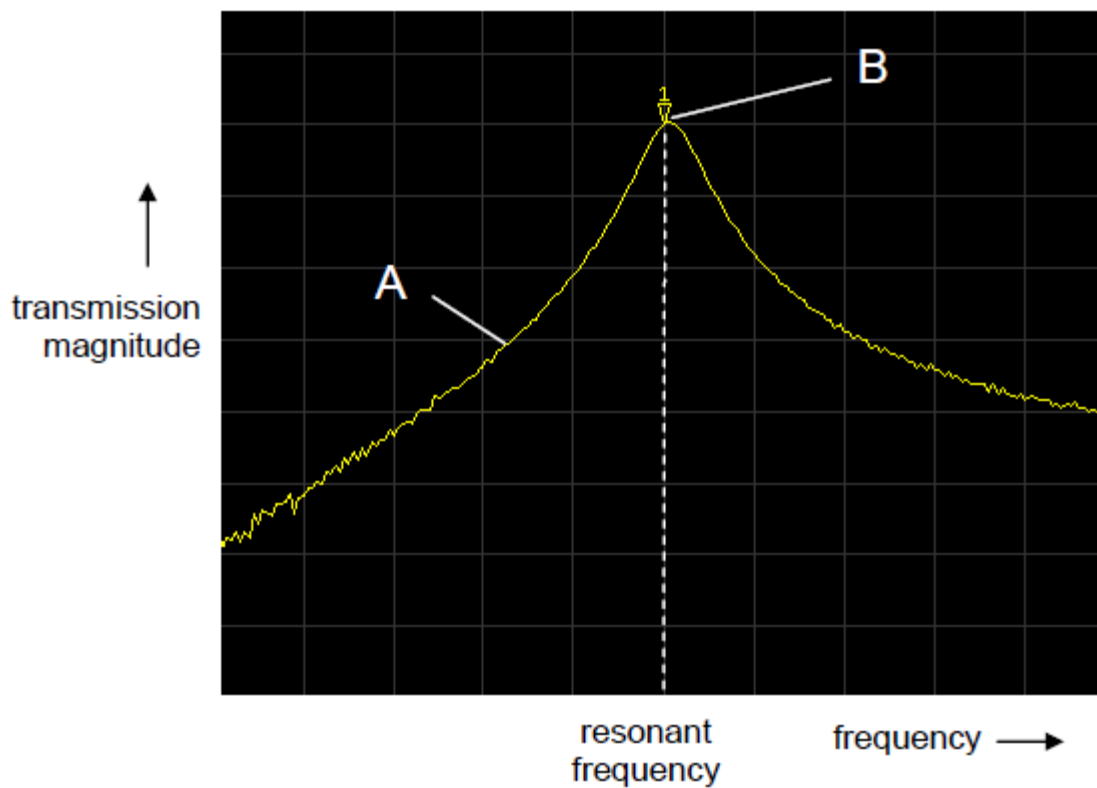


FIG. 2.37: Network analyzer screen snapshot showing an S_{21} curve from the coil configuration of Fig. 2.36. Point 'A' is a nonresonant frequency, so little energy transfer is measured. Point 'B' exhibits maximum transfer at the resonant frequency.

creates a current. This current, in turn, induces the magnetic field of the coil, which establishes the coil's electric field in the region immediately surrounding the coil.

Two types of electric fields are produced by a surface coil. The first of these is called a *conservative* electric field, also known as a 'static' or 'stray' electric field. Conservative electric fields are created (following Coulomb's Law) by the individual point charges of the surface current distribution of a coil. The reason these fields are considered *conservative* can be explained using the equation for the electrical potential difference between two points A and B :

$$V_{AB} = -\int_A^B \vec{E} \cdot d\ell \quad [2.20]$$

The placement of a test electric charge within an electric field is an illuminating way to interpret Equation [2.20]. If charge #1 shown in Figure 2.38 were moved through a strictly circular path, no net work would be performed by, or on, the charge. This is because the direction of motion $d\ell$ is perpendicular to the electric field \vec{E} along the entire contour, making $\vec{E} \cdot d\ell = 0$. If test charge #2 were taken through a more complicated path but still returned to its starting position, there is an equal amount of positive and negative work done on the charge, and the net work is likewise zero. The fact that no work is performed around any arbitrary closed loop forms the definition of a conservative field.

The second type of field produced by a coil is called a *nonconservative* electric field. This type of field is a result of Faraday's Law, forming closed-loop patterns around

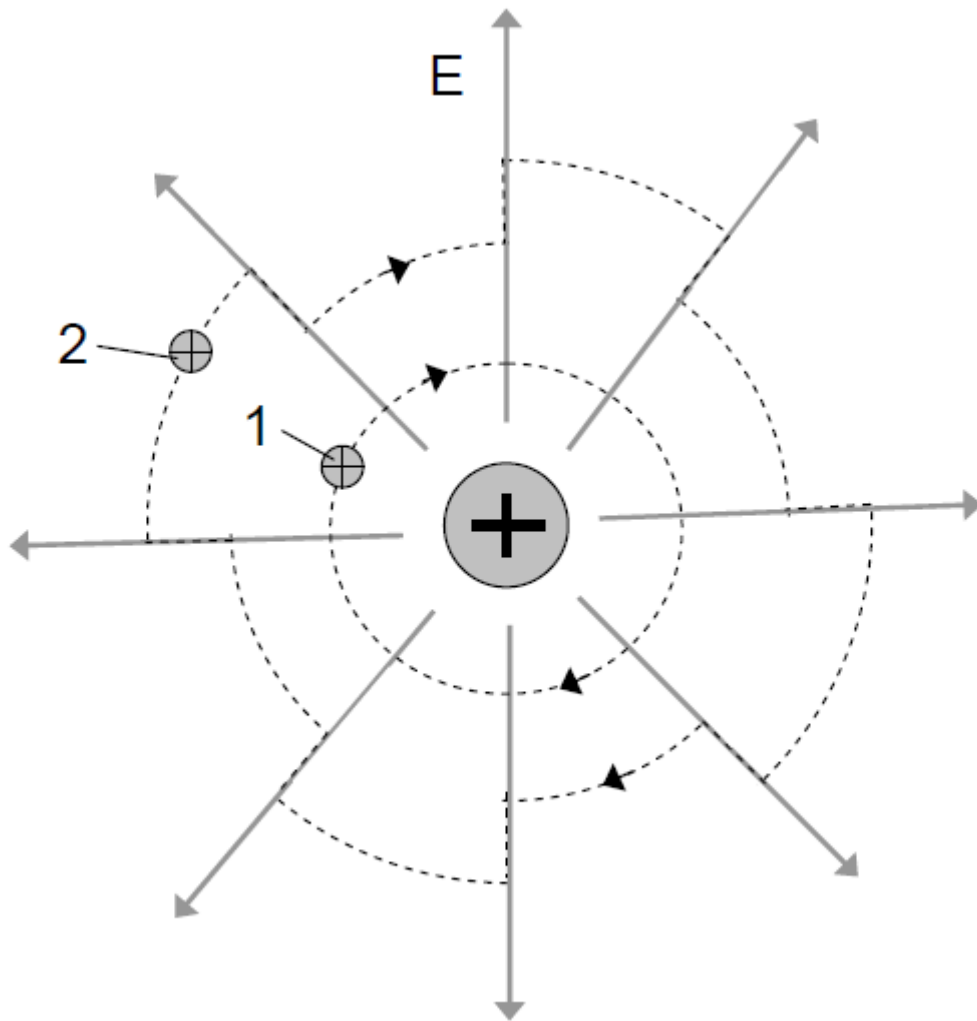


FIG 2.38: Test charges in an electric field E ; zero net work is performed on any test charge moved around any arbitrary closed path.

regions of changing magnetic flux. Due to their closed-loop nature (rather than the point-source nature of conservative fields), nonconservative fields exert work on point charges in the coil environment and add noise to the coil system. Unfortunately, loss and noise from nonconservative fields are unavoidable because these fields naturally exist in conjunction with the magnetic fields essential to imaging.

Two primary energy loss mechanisms must be considered when analyzing surface coils: *coil* resistance loss and *sample* (or *dielectric*) resistance loss [26]. Coil resistance loss is caused by the cumulative resistance of all components of the coil structure itself, i.e. the resonant conductor and capacitors. Since any resistive element in an electrical system is a source of noise [24], more resistance in a coil circuit leads to increased noise, decreased Q, and reduced rSNR.

Sample resistance loss, on the other hand, occurs when both magnetic and electric fields produced by the coil pass through the sample. Electric fields interact with the random motion of charges within the sample, producing heat in conjunction with coil noise. This effect is called *capacitive coupling*. Magnetic fields induce eddy currents in the sample with similar results. These combined factors have a detrimental effect upon the imaging properties of the coil: not only is valuable signal energy lost to heat, but the coil detects additional noise from random charge movements and fluctuating magnetic dipoles that further decreases the SNR [28].

Although magnetic fields, and both conservative and nonconservative electric fields, contribute to the sample loss of a coil, only conservative electric fields can be effectively reduced through proper coil design. Conservative, or stray, electric field is produced by capacitors within the coil. During each cycle of coil resonance, electric

charge flows through the coil conductor and builds up across the terminals of each capacitor. The large quantity of accumulated charge within the coil capacitors causes electric fields to ‘jump’ across the coil surface, resulting in stray fields that penetrate into the sample. Johnson (thermal) noise couples into the coil via these fields, increasing the sample loss but contributing no useful signal [21].

Ironically, while capacitors are the source of conservative electric field in a coil, they can also serve to reduce the stray conservative field. A common method of reducing the electric field-induced sample loss of a coil is to insert a number (N) of equally spaced capacitors around the coil (see Fig. 2.39). The total loop voltage is split equally among the capacitors and reduced by $1/N$, with the result that the stray electric field magnitude is also reduced by $1/N$. Additionally, N virtual ground points are established, which significantly weakens the electric field in the sample region [29].

An important trade-off must be considered when distributing capacitors around a coil: adding additional capacitors may decrease the *sample* loss, but extra capacitors also contribute to the total *coil* loss. Although the sample loss is generally much larger than the coil loss [26], justifying the addition of capacitors, the number of capacitors must nevertheless be limited to maintain a low coil loss. Regarding the optic nerve coil, numerous studies were performed to determine the optimum relationship between the coil size (diameter), coil construction material (copper foil or wire), and the number of distributed capacitors around the coil. These studies will be presented in Chapter 3: Construction.

Noise produced as a result of sample loss can be represented as an equivalent resistance r_{sample} . Since two different phenomena – magnetic fields and electric fields –

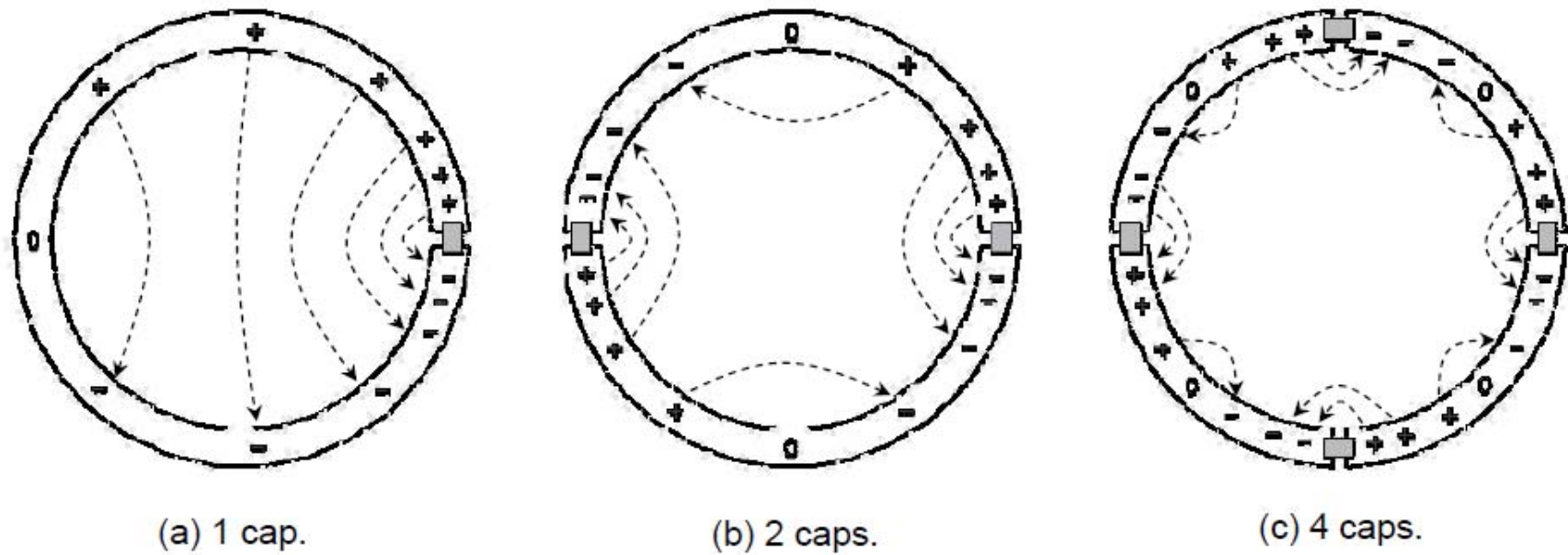


FIG. 2.39: Various distributed capacitor configurations illustrating the approximate conservative (stray) electric fields of a coil (the '0' marks represent the virtual grounds created by the distribution of charge through the coil conductor). (a): a single capacitor produces a large amount of stray field that penetrates the sample. (b) and (c): as the number of distributed capacitors increases, the stray electric field is reduced. Adapted from [29].

contribute to the sample loss of a coil, r_{sample} has two different expressions. In terms of the total electric field produced by two nearby coils:

$$r_{sample(i,j)} = \sigma \int_{volume} E_i \cdot E_j \partial v \quad [2.21]$$

where $r(i \neq j)$ expresses the correlated noise between two coils i and j , and $r(i = j)$ the self-incurring noise. Through the use of the Poynting theorem, it can be shown that Equation [2.21] represents the effective noise resistance, or the power dissipated within the sample volume due to stray electric fields [21]. In terms of the magnetic field penetrating the sample:

$$r_{sample} \propto \sigma \omega^2 B_1^2 b^5 \quad [2.22]$$

where σ is the sample conductivity, ω is the Larmor frequency, B_1 is the RF pulse that tips the sample spins, and b is the size of the sample within influence of the coil, also called the *filling factor*. There is a strong dependence of r_{sample} upon the Larmor frequency in Equation [2.22], and a much stronger dependence upon the filling factor b of the coil. Due to these dependencies, r_{sample} is typically many times larger than r_{coil} for large imaging volumes such as a human torso or head at high field strengths [28].

2.3.4 SNR Considerations

Signal-to-noise ratio (SNR) is generally defined as:

$$SNR = \frac{\textit{average signal amplitude}}{\textit{standard deviation of noise}} \quad [2.23]$$

Increased SNR is the primary goal of modern coil design. In simple terms, SNR can be viewed as a type of imaging ‘currency’, redeemable for other performance factors that may be beneficial when scanning certain anatomy. For example, increased imaging speed might be favorable for motion-prone anatomy such as the chest or the eyes. On the other hand, increased image resolution may be required to differentiate minute tissue characteristics for tumor detection. Thus, by designing a coil with high SNR, many imaging possibilities become available to the diagnostic clinician.

Since RF coils serve as the interface between the patient and the complex chain of imaging hardware, their performance characteristics ultimately determine the maximum achievable SNR of the entire system and are of crucial importance to consider [30]. The many factors that contribute to the SNR of a coil fit into one of two main categories: first, the physical construction characteristics and hardware properties of the coil; second, the pulse sequence used to excite the sample and retrieve data [21]. Additional factors during postprocessing of the raw image data affect the SNR of the final image, but these considerations are limited by the total SNR available from the coil.

Despite its common use in the literature, utilizing pure SNR as a gauge for coil performance is inherently problematic in a practical research environment. Arriving at an

accurate figure for the SNR of any particular setup requires an in-depth knowledge of every aspect of that setup, such as the conductivity and thermal properties of the sample, the coil characteristics, equipment state, imaging method, etc. While it may be possible to determine SNR, such an analysis would be painstaking and strictly academic.

A much more realistic – and yet accurate – coil performance metric is the *relative* SNR. rSNR is distinguished by the fact that only one variable is assumed to change between scans – namely, the coil itself. All other variables, including the scanner, sample, environment, imaging protocol, etc., remain constant. When comparing two coils, these assumptions are reasonable to make: the separate comparison scans are typically performed on the same scanner within a short time period so that similar scanner and environmental properties are maintained; the same test subject is used in both coils; finally, similar imaging protocols control the voxel size and RF field parameters so that only the properties unique to each coil are what affect the final image results. The term rSNR is used throughout the remainder of this thesis when quantitatively measuring or comparing coil SNR characteristics.

2.4 Overlap Theory

2.4.1 Volume Imaging

Surface coils were briefly mentioned in Section 2.1 as the FID detection method of choice for this thesis. In the following discussion, the differences between volume and surface coils will be expanded. Since it is usually desirable to image volumes larger than the small sensitivity region of a single surface coil, a method of combining surface coils into large-scale array will be introduced.

Due to their large field of view (FOV) and superb homogeneity, volume coils are frequently used for entire-brain imaging scans in MRI clinics [30]. Their uniform imaging region provides a much more accurate delineation of tissue within an image than any single surface coil could offer (see Figures 2.40 and 2.41). Thus, clinicians are more willing to entrust the wellbeing of their patients to volume coils, despite the poor SNR they provide. This low SNR performance is a direct result of a large imaging region. While an FID signal might be emitted only from a very small anatomical feature, noise is gathered from the entire volume.

Surface coils are known for their highly localized region of sensitivity. This concentration of SNR comes at the expense of field of view, which is generally only about a coil-radius deep into the sample [31]. Many different methods have been explored in recent years to expand the field of view of surface coils while maintaining their characteristically high SNR.

If a large sample is to be imaged, such as the volume region shown in Figure 2.42, a primitive method of volume imaging could be as follows: (A) position the coil on the volume and perform a scan; (B) reposition the coil and perform another scan; (C) repeat the procedure until the entire volume has been traversed, then combine all the data into the final image. Not only does this process necessitate redundant time to sample data at each coil location, but frequent human involvement is required to reposition the coil.

A more practical procedure would be to secure multiple coils to the volume during the initial setup time. Then, during the scan itself, individual coils could be switched on and off as needed to acquire data. This method has the potential advantage of being automated for ease of use by the MRI technician.

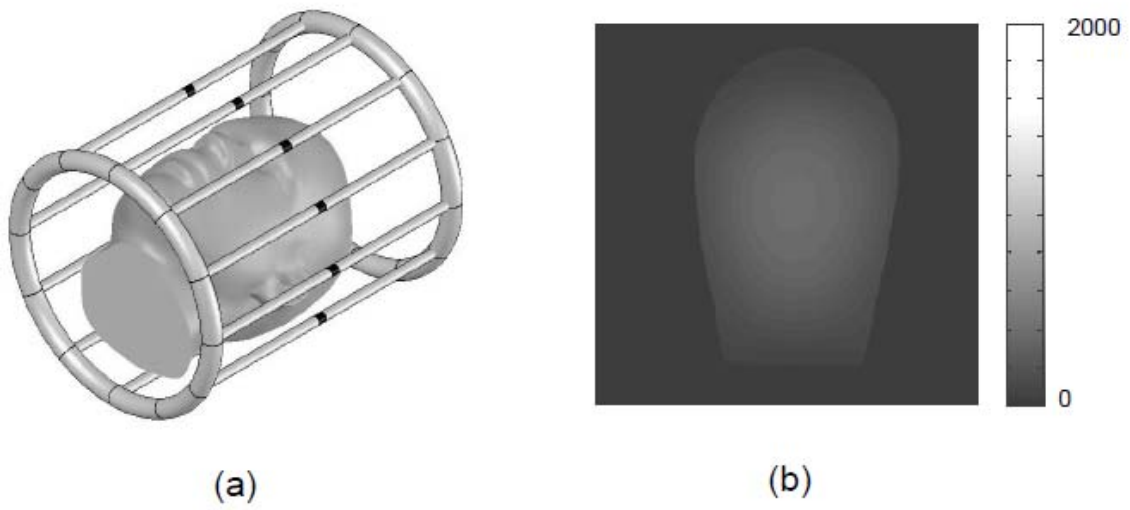


FIG. 2.40: Birdcage volume coil. (a) Coil size relative to a patient. (b) Coronal image slice of phantom showing homogeneous, albeit poor, SNR over the imaging region.

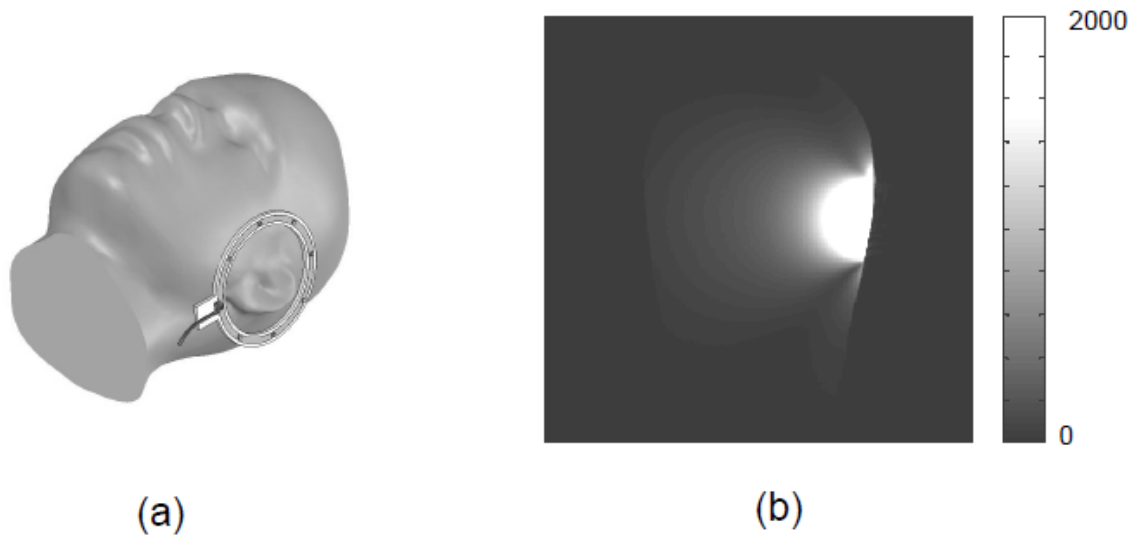


FIG. 2.41: Surface coil. (a) Coil size relative to a patient. (b) Coronal image slice of phantom showing highly localized SNR profile over a small field of view.

Finally, the most ideal arrangement would still involve multiple coils permanently mounted as before, but would also somehow image with all of them *simultaneously* as depicted in Figure 2.43. The speed of a single scan could be maintained with minimal human involvement. A multitude of coils configured together for simultaneous reception has adopted the title of a *phased array*, drawing from a similar concept in antenna design theory.

Phased arrays are advantageous as volume coils in a number of ways. (1) In theory, any number of surface coils can be combined to cover an arbitrary volume. Thus, any anatomical feature has the potential to be imaged, without the access limitations imposed by coils such as a birdcage (refer to Fig. 2.40). (2) In general, higher SNR can be achieved using local phased arrays coils, without the major expense of a higher field strength scanner.

Unfortunately, several limitations hinder the benefits of multiple-coil volume imaging. (1) Only a limited number of channels are available on commercial MRI machines – typically up to 32. (2) The more coils arranged together over a given volume, the smaller each coil tends to become. Noise due to coil resistance becomes a dominant factor as coil size decreases, thus nullifying the benefit of additional coils. (3) Perhaps most importantly, combining coil elements into an array introduces mutual inductance effects that occur between adjacent coils. If a large number of surface coils are inductively coupled, the noise that is shared among the coils reduces the SNR performance of array to that of a standard volume coil. Such problems can be viewed as instructive challenges in the construction of an imaging coil.

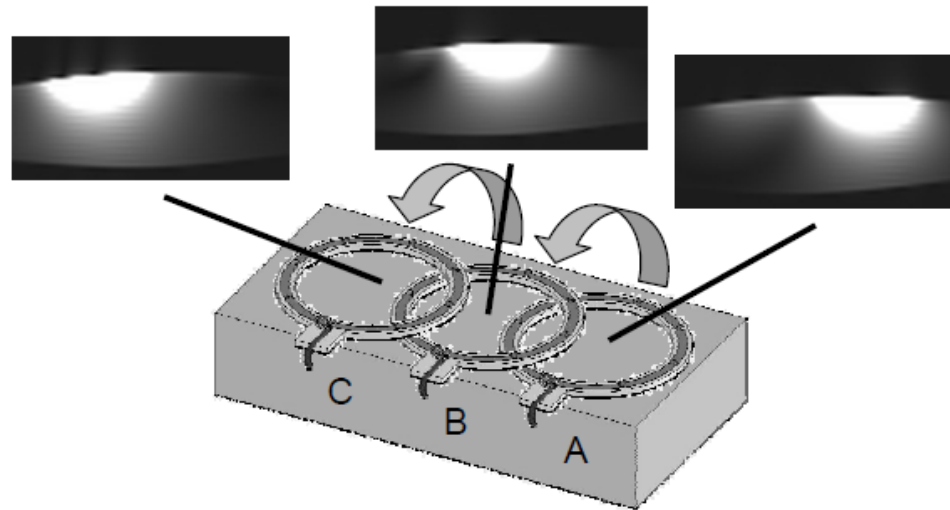


FIG 2.42: Two primitive methods to obtain volume imaging using surface coils: (1) reposition a single surface coil after every scan in order to cover a large volume, (2) secure multiple coils to the volume and sequentially switch each coil on and off for each scan.

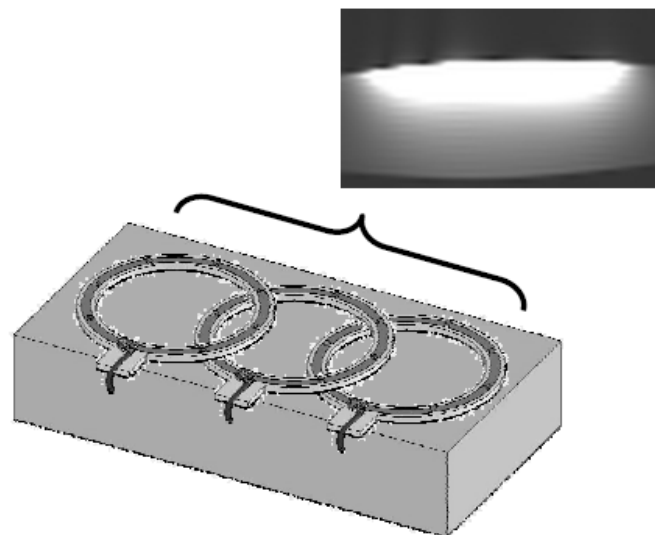


FIG. 2.43: Efficient volume imaging is achieved using multiple coils and simultaneous image reception.

2.4.2 Coil Overlapping

Roemer et al. proposed a method to extinguish the negative coil-to-coil interaction effects of mutual inductance. By overlapping adjacent coils in a precise manner, he demonstrated that the shared magnetic flux between two coils is effectively reduced to zero.

When two loops tuned to the same resonant frequency are placed in proximity (Fig. 2.43), negative interactions occur due to mutual inductance. Signal and noise are transferred between the loops, and a shift in frequency (or a separation into resonant modes – see Fig. 2.44) causes a decline in sensitivity at the target frequency [32].

The frequency shift effect was studied in the lab using two resonant loops. Only one loop had a measurement cable attached, from which S_{11} data were taken using a network analyzer. First, a single isolated loop was placed on a conductive phantom and tuned to resonate at 123.23 MHz (see Fig. 2.45). When a second loop was brought into proximity of the first and overlapped slightly (Fig. 2.46), the resonant frequency split into two discrete modes. A similar problem occurred when the two loops were overlapped too far (Fig. 2.47). However, at a particular overlap position, the separated modes realigned, and each overlapped coil once again resonated at the target frequency (Fig. 2.48).

To explain this effect, it is insightful to examine the electric and magnetic field coupling between two coils placed in proximity. Figure 2.49 illustrates two rectangular loops of side length d placed on the planar surface of a conductive volume. Initially, the two loops are completely overlapped, one atop the other. At this starting position the ratio of the separation distance L to the loop size d is zero, corresponding to the X -axis

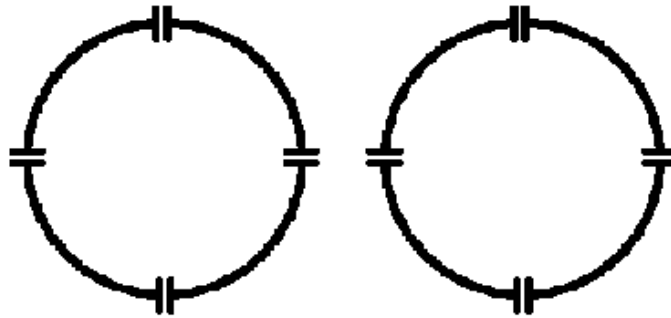


FIG. 2.43: Two coils, tuned to the same resonant frequency (f_0), placed near each other.

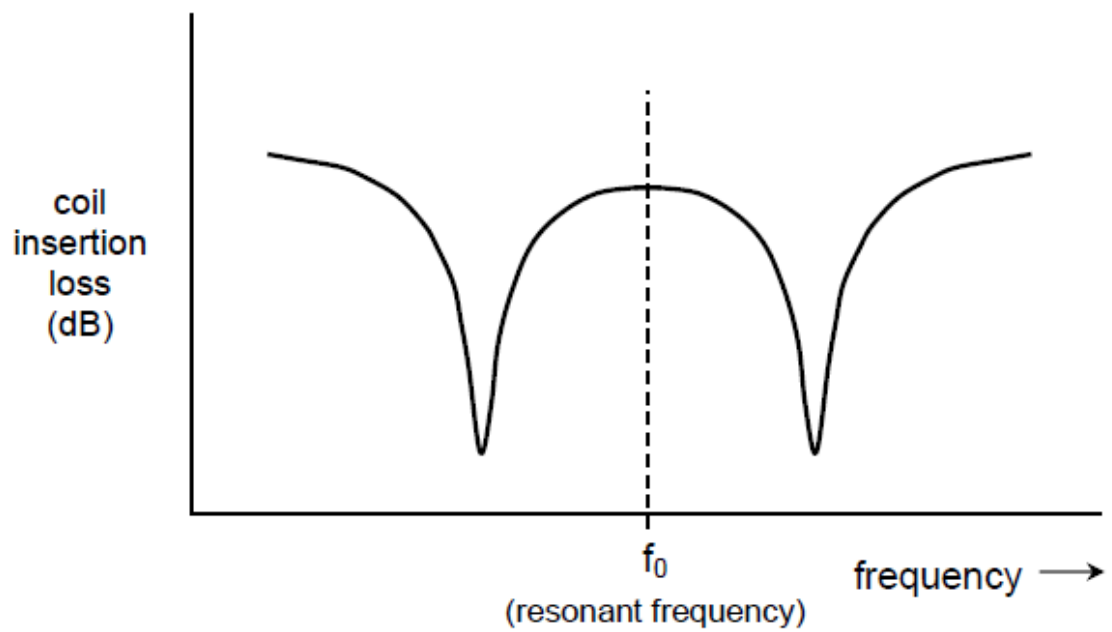


FIG. 2.44: S_{11} plot illustrating the separation of coil resonance into two discrete modes due to the proximity of two similarly-tuned coils. Adapted from [32].



FIG. 2.45: A single resonant coil with an ideal resonant S_{11} curve.

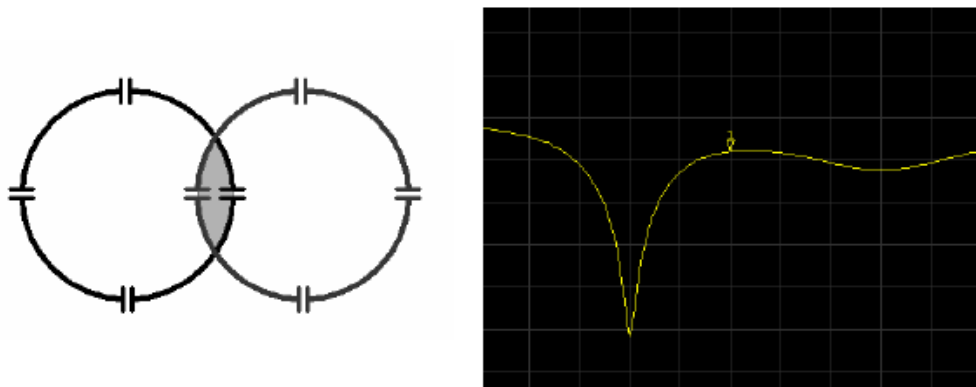


FIG. 2.46: When another resonant coil is introduced and overlapped slightly, the resonant frequency of the system splits into two discrete modes.

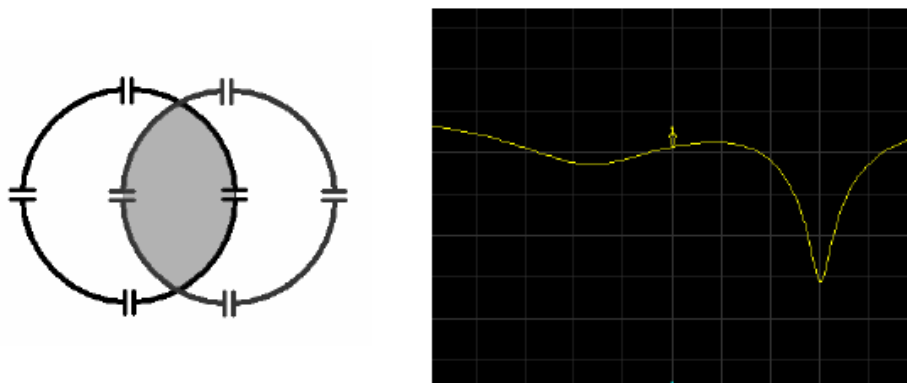


FIG. 2.47: A similar occurrence for two resonant coils overlapped slightly too far.

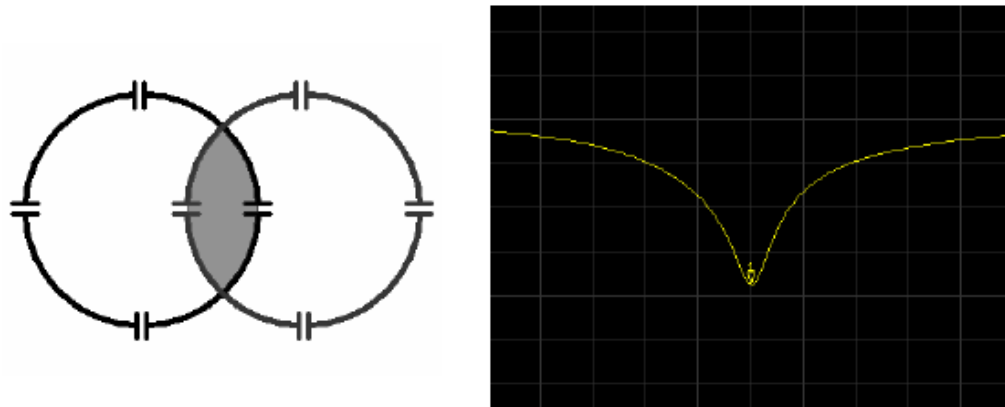


FIG. 2.48: At a particular overlap distance, the modes realign and a single resonant frequency is reestablished.

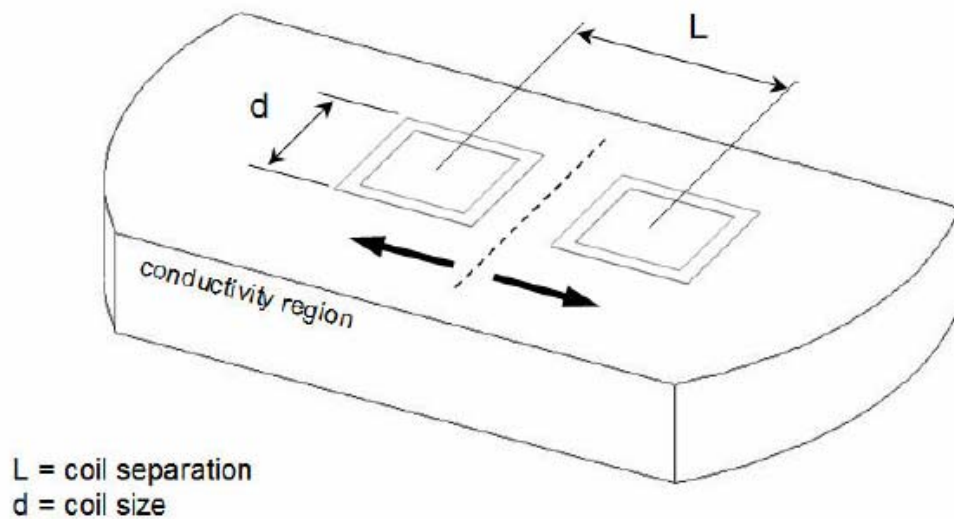


FIG. 2.49: Two square coils on a conductive volume are initially placed completely overlapping each other ($L = 0$), then moved apart following the bold arrows ($L > 0$). Adapted from [32].

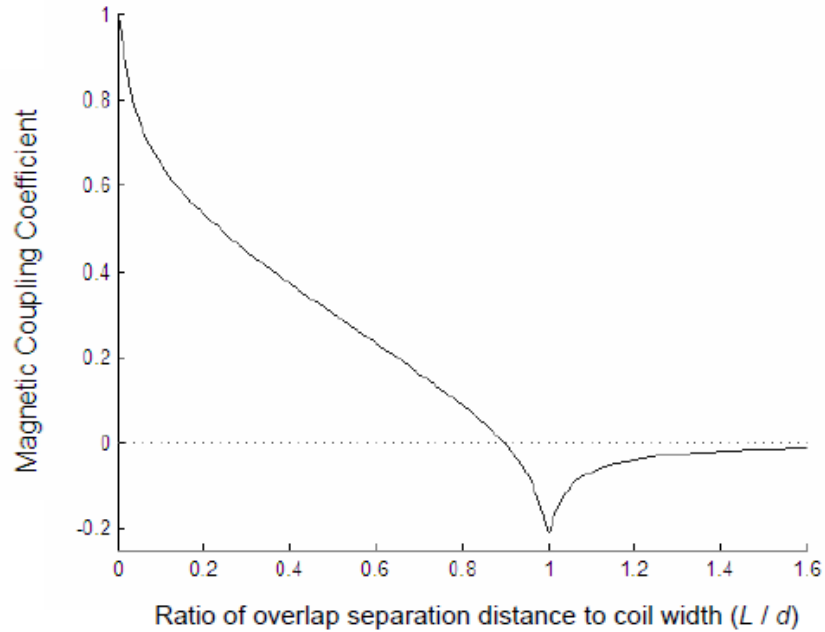


FIG. 2.50 The magnetic and electric coupling between the coils of Fig. 2.46. The point of flux cancellation occurs at approximately 0.9 of the overlap-distance-to-coil-size ratio (L/d). At $(L/d) = 1.0$ one leg of each coil is directly overlapped. Adapted from [32].

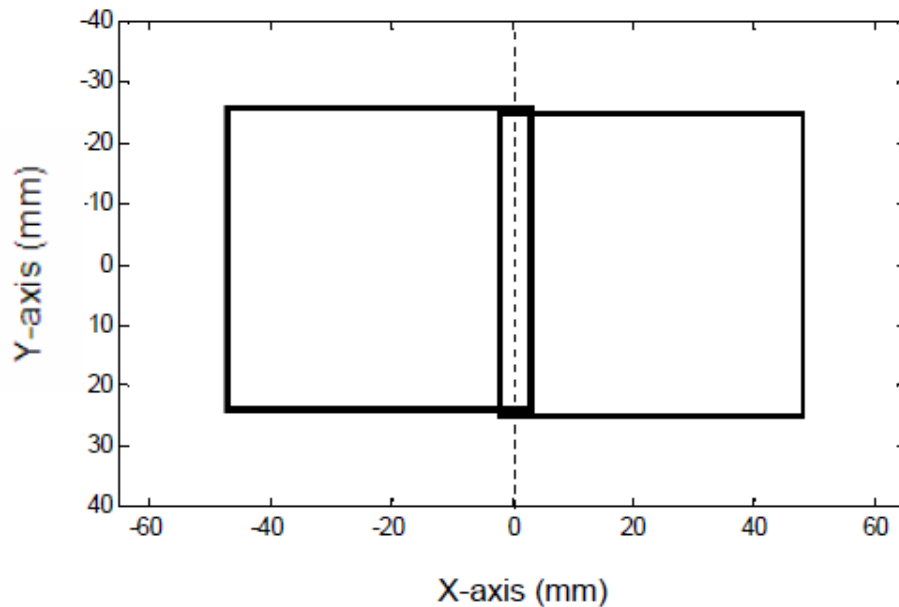


FIG. 2.51 Diagram of two square coils overlapped to produce zero mutual inductance; the overlap amount corresponds to the coil center-to-center separation distance to coil width ratio (L/d) of approximately 0.9.

origin of Figure 2.50 As the separation distance L between the two loops is increased, the amount of overlap decreases, as well as the resultant mutual inductance coupling. Finally, at a specific overlap point of approximately $(L / d) = 0.9$ (see Fig. 2.51), the magnetic coupling decreases to zero. At this point there is *zero* inductive coupling; the two loops are completely magnetically isolated because the mutual flux between them is cancelled.

The same effect does not occur for the electric coupling coefficient of two overlapped loops. Electric coupling approaches zero asymptotically as the two loops are moved an infinite distance apart. Thus, for any practical overlap distance encountered during coil construction, noise from shared electric fields is transferred between coil elements despite the cancelled magnetic flux.

Visualizing the induced flux pattern of a loop is helpful for understanding mutual flux cancellation. Figure 2.52 illustrates two coils, labeled A and B, overlapped at the optimal position for flux cancellation. Figure 2.53 shows a top view of the same overlap configuration. At the optimal point of overlap, the shared flux *into the page* is equal, and opposite, the shared flux *out of the page*. Equation 2.24 expresses this relationship mathematically:

$$\sum (\times) + \sum (\bullet) = 0 \quad [2.24]$$

By the Biot-Savart law, the magnetic field of a conductor falls off by the square of the distance from the conductor. Thus, in terms of set theory, the point of optimum overlap occurs such that the intersection of the coil surface areas ($S_A \cap S_B$) is much

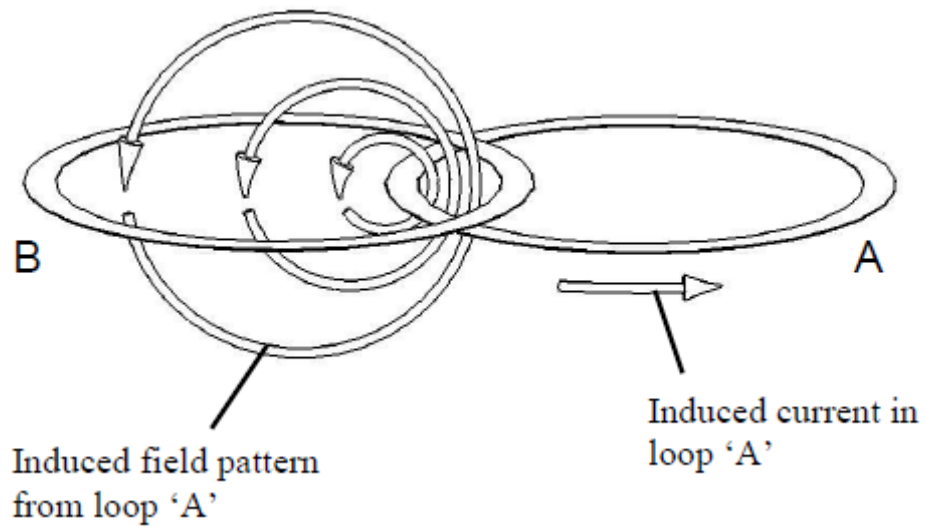


FIG 2.52: Approximate induced flux pattern of loop 'A' passing through surface of loop 'B'. Only shared flux is shown.

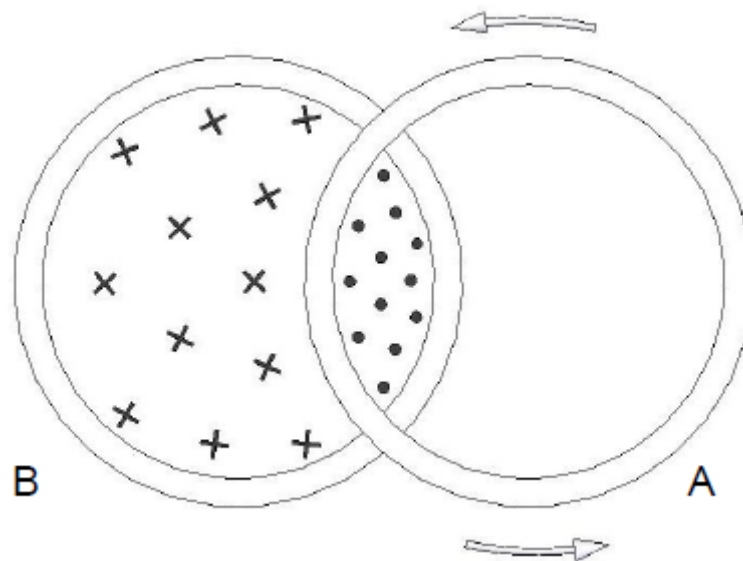


FIG. 2.53: Top view of two overlapped loops A and B. Arrows represent current flow in loop A, 'X' represents shared flux into the page, and '•' represents shared flux out of the page.

smaller than either of the remaining areas $S_A - (S_A \cap S_B)$ or $S_B - (S_A \cap S_B)$. As an additional note of interest, the same cancellation effect works in reverse by reciprocity: the shared flux from loop B through loop A cancels in an equivalent manner.

It is important to realize that, during the construction of a phased array, the process of overlapping coils is not as simple as merely ‘sliding two loops together.’ By way of illustration, suppose two isolated, resonant loops A and B are tuned and matched to resonate exactly at an arbitrary frequency. In other words, the S_{11} and S_{22} curves of A and B, respectively, are individually adjusted to the ideal state shown in Figure 2.35. Figure 2.54 shows a typical network analyzer screenshot of loops A and B after being placed in proximity, without any regard to proper overlapping. An S_{21} trace is introduced to measure the power coupling, via shared flux, between the two loops. It may seem that the optimum overlap position would be obtained by simply minimizing S_{21} . However, in the process of overlapping the coils, both S_{11} and S_{22} in Figure 2.54 have individually slipped off resonance. The flux shared between them is no longer reciprocally cancelled. Thus, if the S_{21} curve were minimized in this state for proper overlap distance, a false minimum would be obtained. Instead, the process of overlapping is iterative, requiring repeated adjustment of all three measurements – S_{11} , S_{22} , and S_{21} – to achieve a correctly overlapped array. Successful completion of this process is shown in Figure 2.55.

Obtaining the maximum rSNR from an overlapped coil array involves more than simply being careful during the overlapping process. An additional and very important consideration stems from the discussion in Section 2.2.3: Coil Cross-sectional Profiles; namely, the fact that the alignment of the primary magnetic field B_0 relative to an individual coil determines the coil field profile as shown in Figures 2.31 and 2.32.

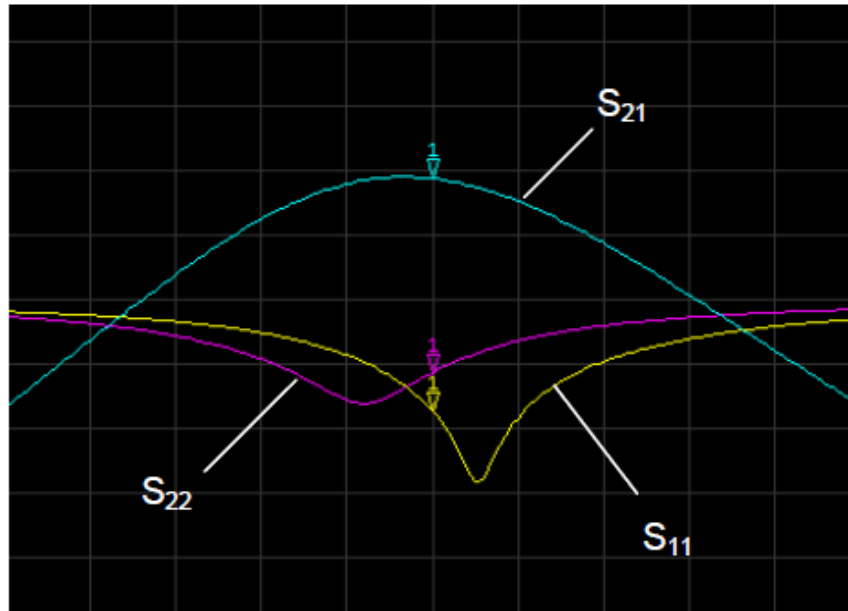


FIG. 2.54: Network analyzer screenshot of two overlapped, out-of-tune coils. The respective S_{11} and S_{22} curves of resonant coils A and B are shown, along with the S_{21} curve of the two coils (or the coil-to-coil power coupling through shared flux).

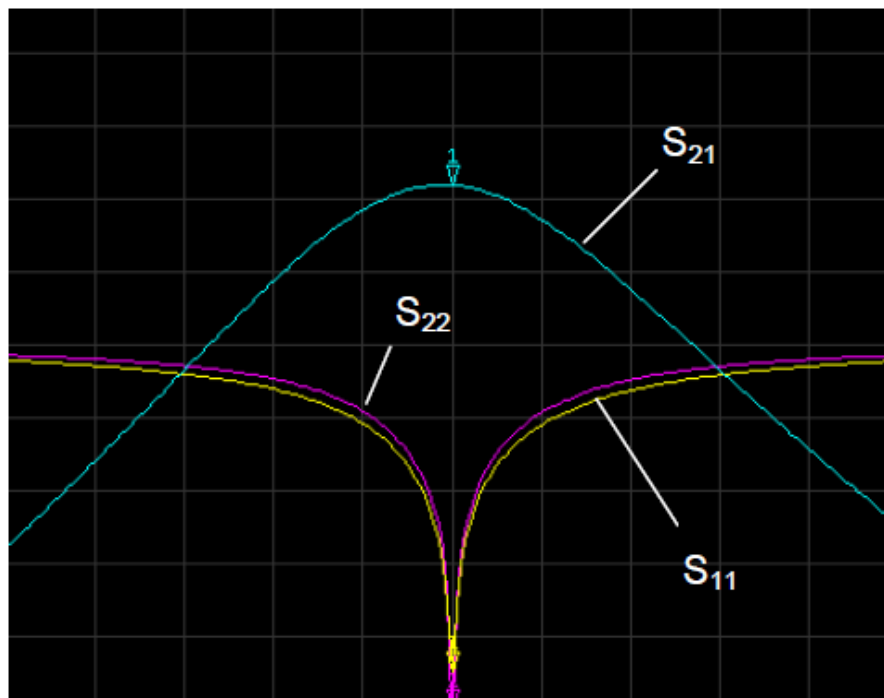


FIG. 2.55: Network analyzer screenshot of two properly overlapped and properly tuned coils. The S_{11} and S_{22} traces are shown after being tuned and matched at the resonant frequency, and S_{21} is minimized.

When two coils are overlapped for mutual flux cancellation, the unique field profile of each coil combines with the profiles of neighboring coils by superposition. In the case of transverse-plane overlapping (Fig. 2.56), the image rSNR directly beneath the overlap region is improved by the square root of two above that of a single isolated coil. However, when coils are overlapped along the bore (Z) axis, a drop in rSNR occurs due to the signal shadow region of each coil (Fig. 2.57). A plot comparing the magnetic field magnitude profiles of each overlap orientation is shown in Figure 2.58. The sum of squares algorithm was used to compute each magnitude plot in this simulation (see Appendix B) [32]. To exploit the enhanced rSNR resulting from transverse-overlapped coils during the construction of ONC2, the overlap direction of ‘key’ coils (coils directly along optic nerve tract) was aligned within the transverse plane.

2.5 Decoupling Theory and the Preamplifier Board

The raw FID signal from sample spins, as detected by a coil, is of such small magnitude that a great deal of supporting circuitry is required to amplify it to a useable level. As part of their research correspondence program, Siemens Medical Solutions donated specially-designed preamplifier circuits for the completion of this project. Not only do these drop-in units perform the challenging task of FID signal magnification, but they act as an additional supplement to the effect of coil decoupling.

Overlapping adjacent coils does not solve all the problematic issues related to coil interaction. So far, this discussion has overlooked the most critical sources of coupling to have under control, which can lead to the most potentially hazardous risks to the patient during an MRI scan: the coupling of the local receive coil array to the transmit coil.

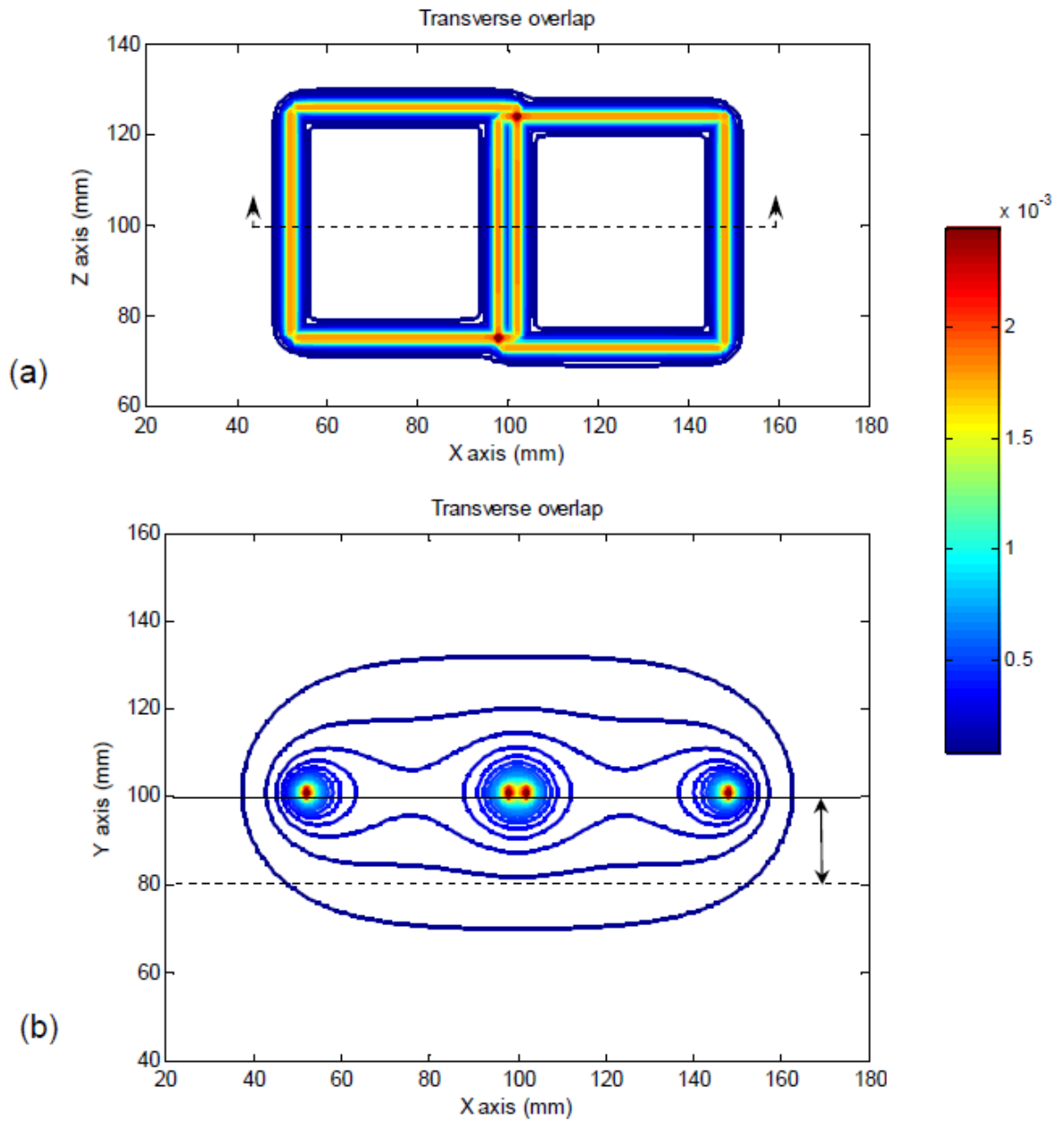


FIG. 2.56: Biot-Savart simulation of two overlapped 5.0 x 5.0 cm coils using Matlab®. (a) Two properly overlapped loops, with a transverse overlap axis. (b) Cross-sectional magnetic flux magnitude contours along the dotted line in (a); the arrow represents imaging depth.

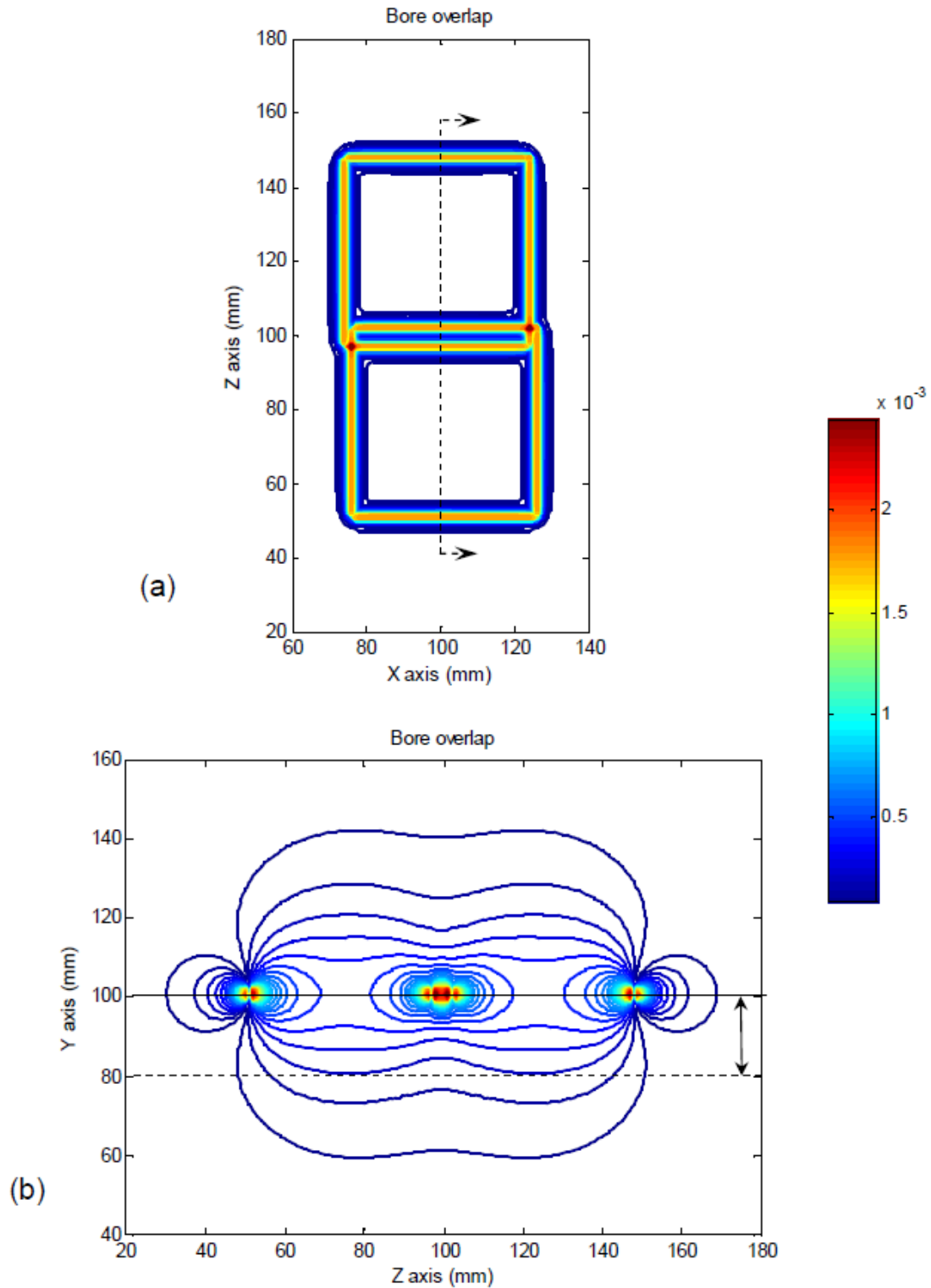


FIG. 2.57: Biot-Savart simulation of two overlapped 5.0 x 5.0 cm coils using Matlab®. (a) Two properly overlapped loops, with the overlap axis along the scanner bore (Z). (b) Cross-sectional magnetic flux magnitude contours along the dotted line shown in (a); the arrow represents imaging depth.

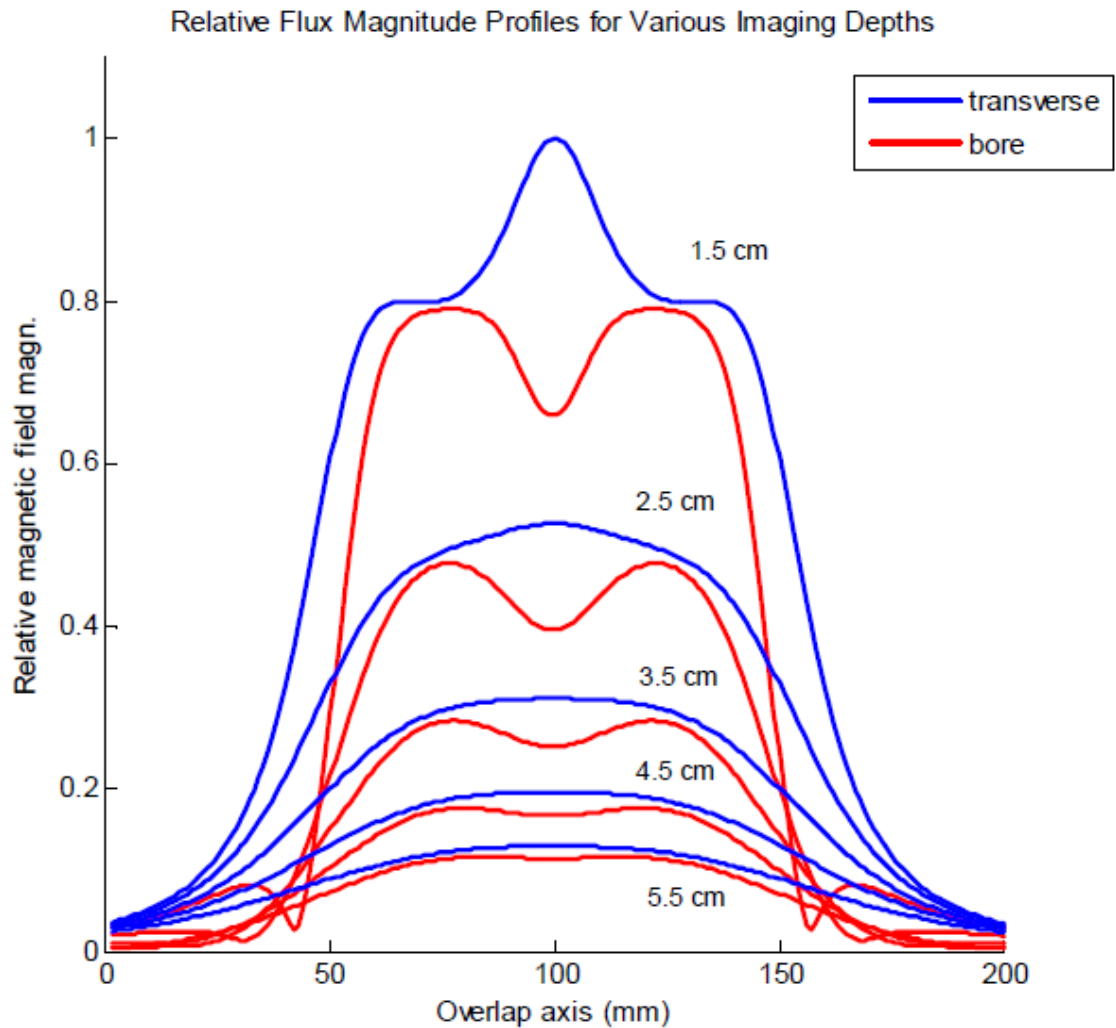


FIG. 2.58: Comparison plot of magnetic flux magnitude profiles at various imaging depths ranging from 1.5 to 5.5 cm from the overlapped coil orientations of Figs. 2.56 and 2.57. The flux magnitude from transverse-overlapped coils is greater than that of the scanner bore-overlapped coils along the entire overlap axis.

2.5.1 Traps

The theory of parallel resonance is a very fundamental concept from electrical engineering that governs nearly every aspect of coil operation – from the resonance of the coil itself, to the methods in which coils are decoupled, and finally to the uncorrupted transfer of signals to the preamplifier and processing hardware.

Traps employ the theory of parallel resonance to create ‘virtual open circuits’ when current flow is undesirable along a prescribed path. Some traps are installed on a cable to passively eliminate undesirable currents along a specific portion of a conductor. Others require an input voltage for activation, and are usually used for temporary ‘on/off’ switching of current and consequent detuning of coils.

A resonant, parallel inductor-capacitor (LC) circuit configuration is shown in Figure 2.59. The equivalent impedance of this configuration (looking into the circuit at terminals *A* and *B*) is given Equation [2.25], where Z_C and Z_L are the impedance terms for a capacitor and inductor, respectively.

$$Z_{AB} = \frac{Z_C Z_L}{Z_C + Z_L} \quad [2.25]$$

$$Z_C = \frac{1}{j\omega C} \quad [2.26]$$

$$Z_L = j\omega L \quad [2.27]$$

In order to impede current flow, an open circuit ($Z_{AB} = \infty$) condition must be established across the terminals. This is accomplished by choosing components such that the denominator of Equation [2.25] is equal to zero, resulting in Equation [2.28].

$$0 = Z_C + Z_L = \frac{1}{j\omega C} + j\omega L \quad [2.28]$$

After rearranging,

$$\frac{j}{\omega C} = j\omega L \quad [2.29]$$

which becomes the standard equation for resonance:

$$\omega = \frac{1}{\sqrt{LC}} \quad [2.30]$$

When the trap inductor and capacitor components are carefully tuned to produce a resonating circuit, current is limited across the trap terminals.

The series resonance LC configuration of Figure 2.60 does not produce a useful trap. When performing a mathematical analysis (as above) for a series circuit, one quickly discovers that either of two unusual conditions must be met to produce an open-circuit across the trap terminals. Either the capacitor value must be zero or the inductor value must be infinitely large. Although neither condition is practical for a coil, in other

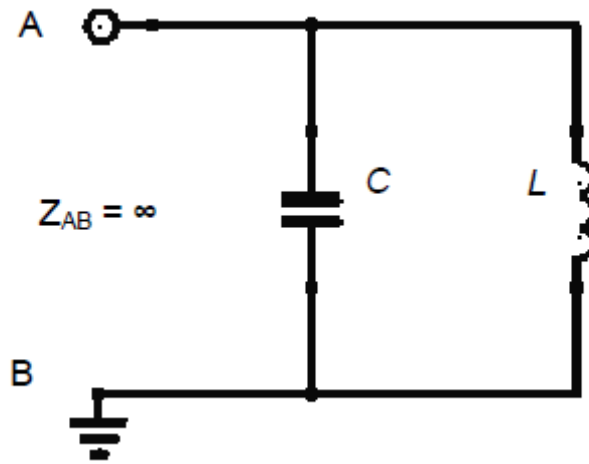


FIG. 2.59: A parallel LC circuit. At resonance, an equivalent open-circuit impedance (Z_{AB}) is established between terminals A and B .

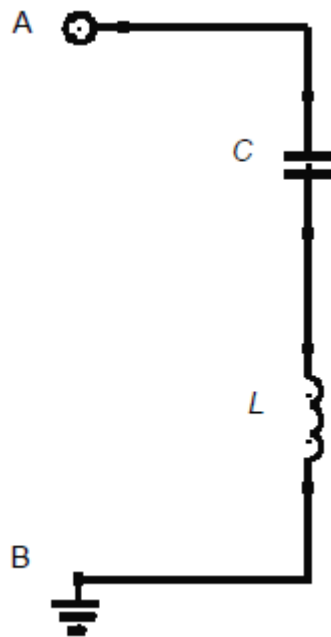


FIG. 2.60: A series LC circuit. At resonance, an equivalent *short-circuit* impedance (Z_{AB}) is established between terminals A and B .

RF applications this type of circuit may find use as a short circuit to pass energy at a particular frequency.

2.5.2 The Coil Cable and Common-Mode Currents

The typical configuration of the coil and supporting hardware is shown in Figure 2.61. Due to the bulky nature of the preamplifier and decoupling circuitry, a coaxial cable is employed for remote placement of the preamp from the coil. Unfortunately, several issues that affect signal quality must be considered in this setup. Specifically if the connecting cable is too long, it may act as an antenna and allow resonant modes to be established along its length, which lead to undesirable shifts in the tune and match of the coil. In addition to resonant modes, common mode currents on the cable are also a detriment to coil performance. Ideally, a properly ‘balanced’ circuit would allow current to flow through the center conductor of the coaxial cable and through the load, then return along the inner surface of the cable shield (see Fig. 2.62). However, common mode currents occur when there is a current phase mismatch at point A, causing an ‘imbalance’ of the feed and return currents through the cable [33]. Undesirable current flows on the outside of the shield, causing electric and magnetic fields to be established along the length of the cable. If a conductive load (such as a hand) is brought near such a “hot” cable, the stray fields along the cable are disrupted, causing havoc with the resonant properties of the coil.

A parallel resonance trap is used to passively kill the flow of common-mode currents along the outside of the coaxial cable connecting the coil to the preamp circuitry. An inductor is formed from the cable shield, and a capacitor is connected across it, as

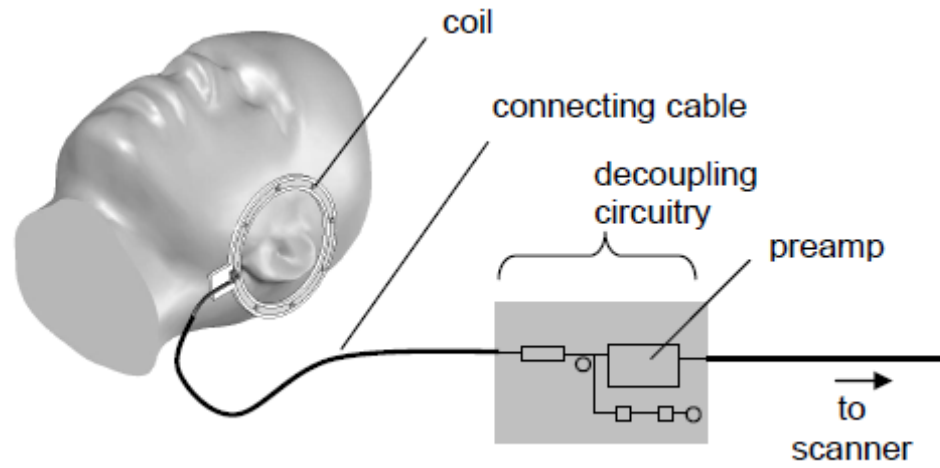


FIG. 2.61: Typical arrangement of imaging hardware for a single channel coil.

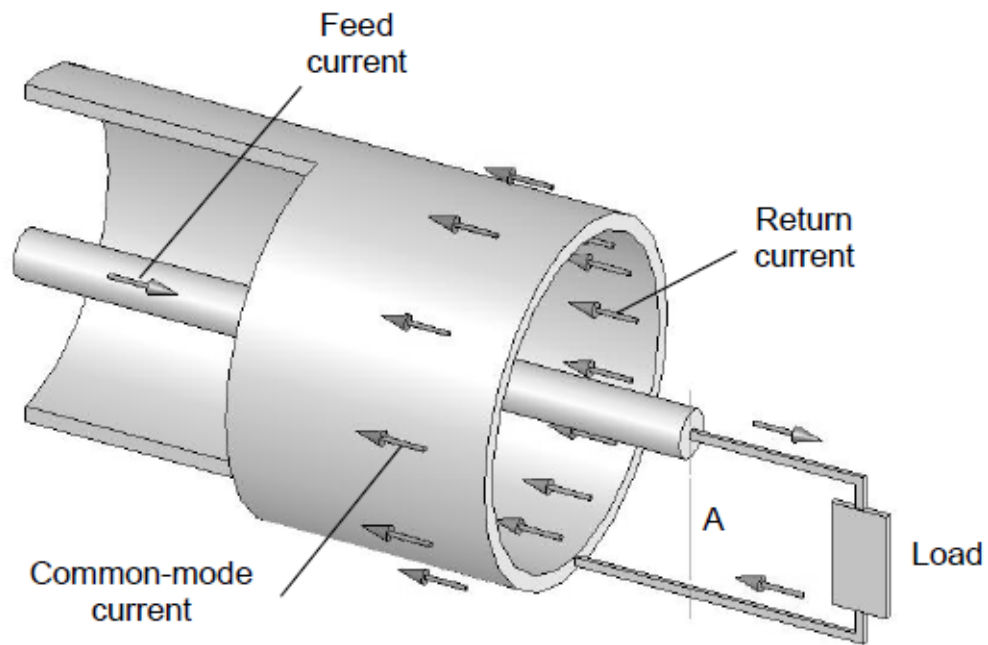


FIG. 2.62: Cut-away illustration of a coaxial cable, showing desirable current passing through the center conductor and returning along the inside of the shield. Common-mode current is undesirable and returns along the *outside* of the shield.

shown in Figure 2.63. When the resonant capacitor/inductor pair is tuned to the Larmor frequency, an effective open circuit is created that blocks common mode currents on the outer shield, but allows the signal current to pass through unaffectedly on the center conductor and inside of the shield.

2.5.3 Active and Passive Decoupling

Another application of a parallel resonance trap is known as a ‘detuning’ trap. In this case, a diode is included to switch the coil current ‘on’ or ‘off’ as desired, making the coil itself resonant or nonresonant, respectively. The trap is inserted at the match point of the coil (Fig. 2.64). When the series PIN diode is forward-biased with a supplied DC voltage during the transmit portion of the pulse sequence, the inductor/capacitor pair resonates at the Larmor frequency. The loop appears very nearly as an open circuit and prevents current flow, and the coil itself is detuned (Figs. 2.65 and 2.66). The DC bias voltage is supplied to the system through a bias-T junction just prior to the input terminals of the preamplifier. The bias-T junction permits the flow of DC voltage to the coil diodes, but prevents its flow into the terminals of the preamp to keep from destroying it.

Active decoupling performs a number of functions. During the transmit phase of an MRI scan, a considerable amount of RF energy is pulsed into the bore to tip the precessing spins within the imaging volume. Since coils are designed as energy storage devices, large voltages induced in resonant coils may potentially cause serious RF burns to a patient within the bore [21]. By supplying a DC voltage to the coil during the transmit phase, the coil is detuned and acts as an open-circuited conductor within the

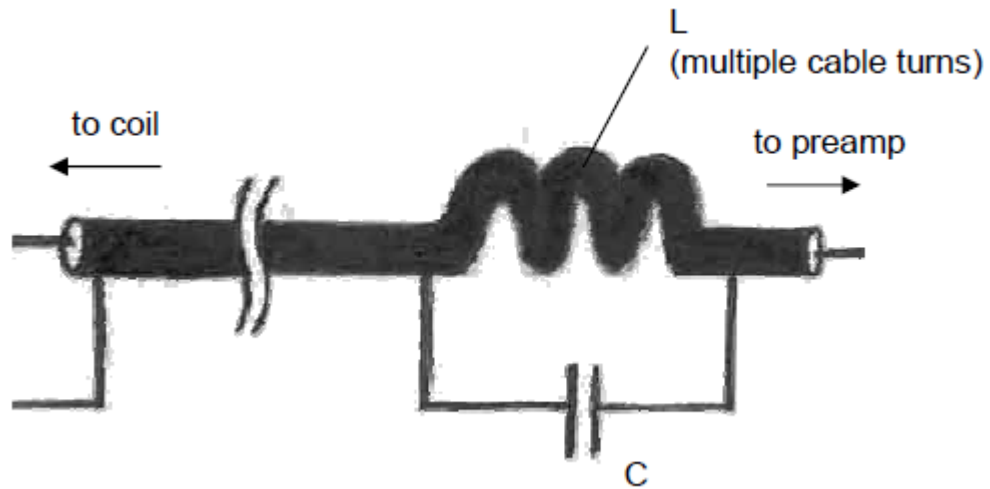


FIG. 2.63: Parallel resonance cable trap used to eliminate common mode currents.

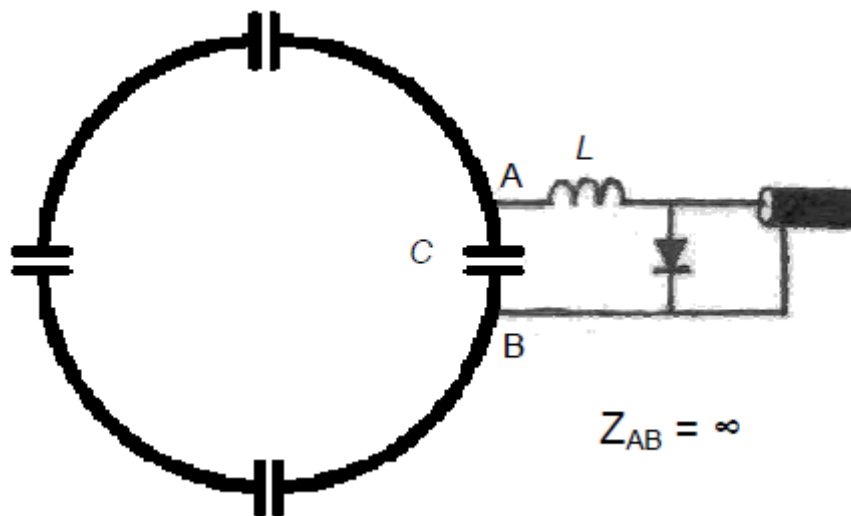


FIG. 2.64: An active decoupling or detuning trap. When DC current is supplied through the coaxial cable, the diode becomes reverse-biased and a virtual open circuit is established across capacitor C .

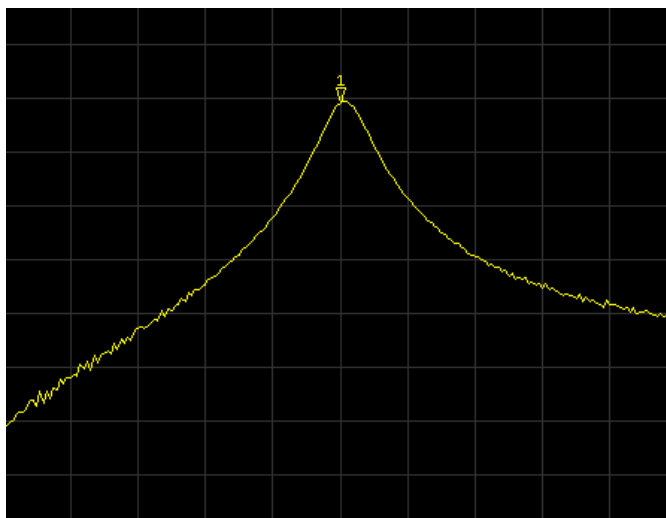


FIG. 2.65: S21 curve of a resonant, isolated coil when decoupling circuit is not activated. The resonant peak is at 123.23 MHz.

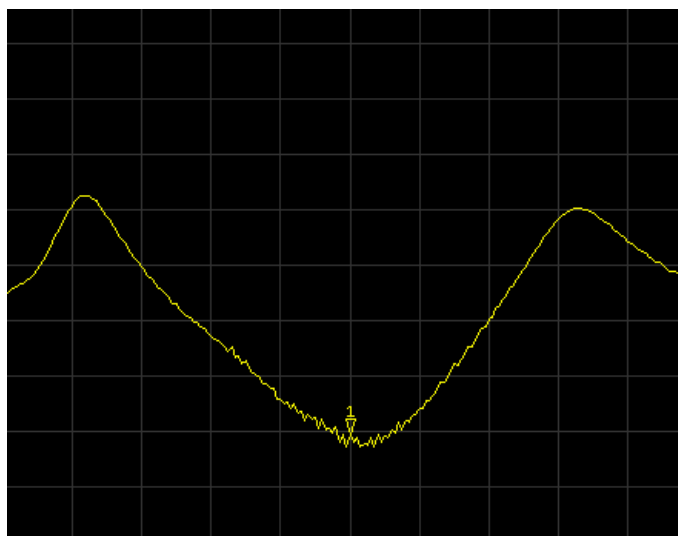


FIG. 2.66: S21 curve showing active decoupling applied to a resonant coil. Power transmission at 123.23 MHz is decreased by approx. 30 dB, and the coil is considered *detuned*.

bore. Burns are prevented unless the active decoupling circuitry fails. In addition, active decoupling is useful during the construction and testing process of a coil. Individual coils can be conveniently switched on and off to verify that coil interactions are minimized. The active decoupling circuitry also performs the added function of impedance matching the coil to 50 ohms when loaded to reduce signal reflections at resonance [26].

Passive decoupling circuits (Fig. 2.67) are used as a failsafe against the malfunction of the active decoupling circuitry of each coil. Should abnormally large voltages be detected on the coil, one diode of a reversed-diode pair becomes conductive during each half period of coil resonance. A small parallel resonance trap is activated, opening the coil and preventing RF burns. In application to the optic nerve coil, passive decoupling is especially important for coils surrounding the eye regions. The lack of blood circulation in the orbits makes them very sensitive to energy deposition from RF radiation [18]; in other words, the orbits have a high specific absorption rate (SAR).

2.5.4 Preamplifier Decoupling

Preamplifier decoupling reduces the interaction of nonadjacent coils. The preamplifier is designed to establish a low impedance across its input terminals. By means of a pi-network phase shifter, the electrical distance from the coil to the preamplifier is tuned to $\frac{1}{2}$ wavelength (λ). The low input impedance of the preamplifier is translated through the coaxial cable by $\frac{1}{2} \lambda$, creating a virtual low impedance (or short circuit) across the diode of the detuning trap, and parallel resonance occurs in the same manner as with active decoupling. The circuitry that enables preamplifier decoupling is shown in Figure 2.68.

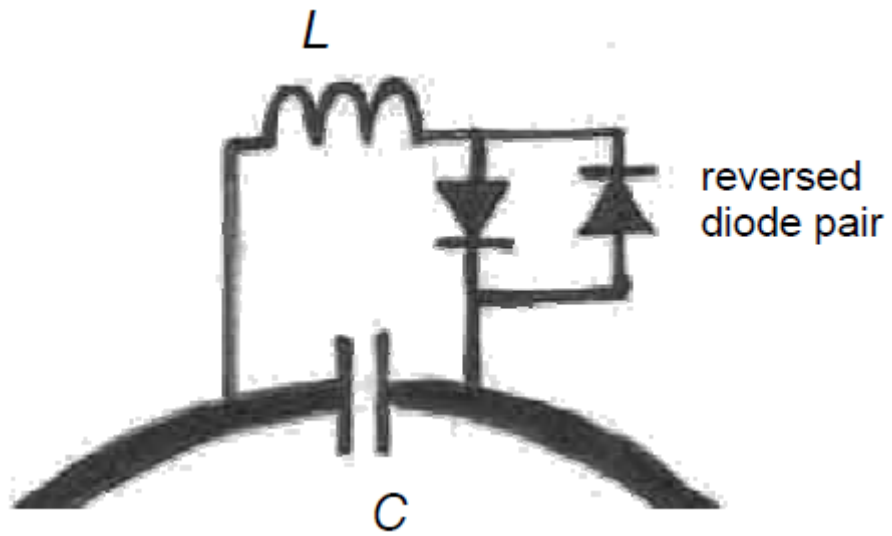


FIG. 2.67: Passive decoupling trap installed across a coil capacitor.

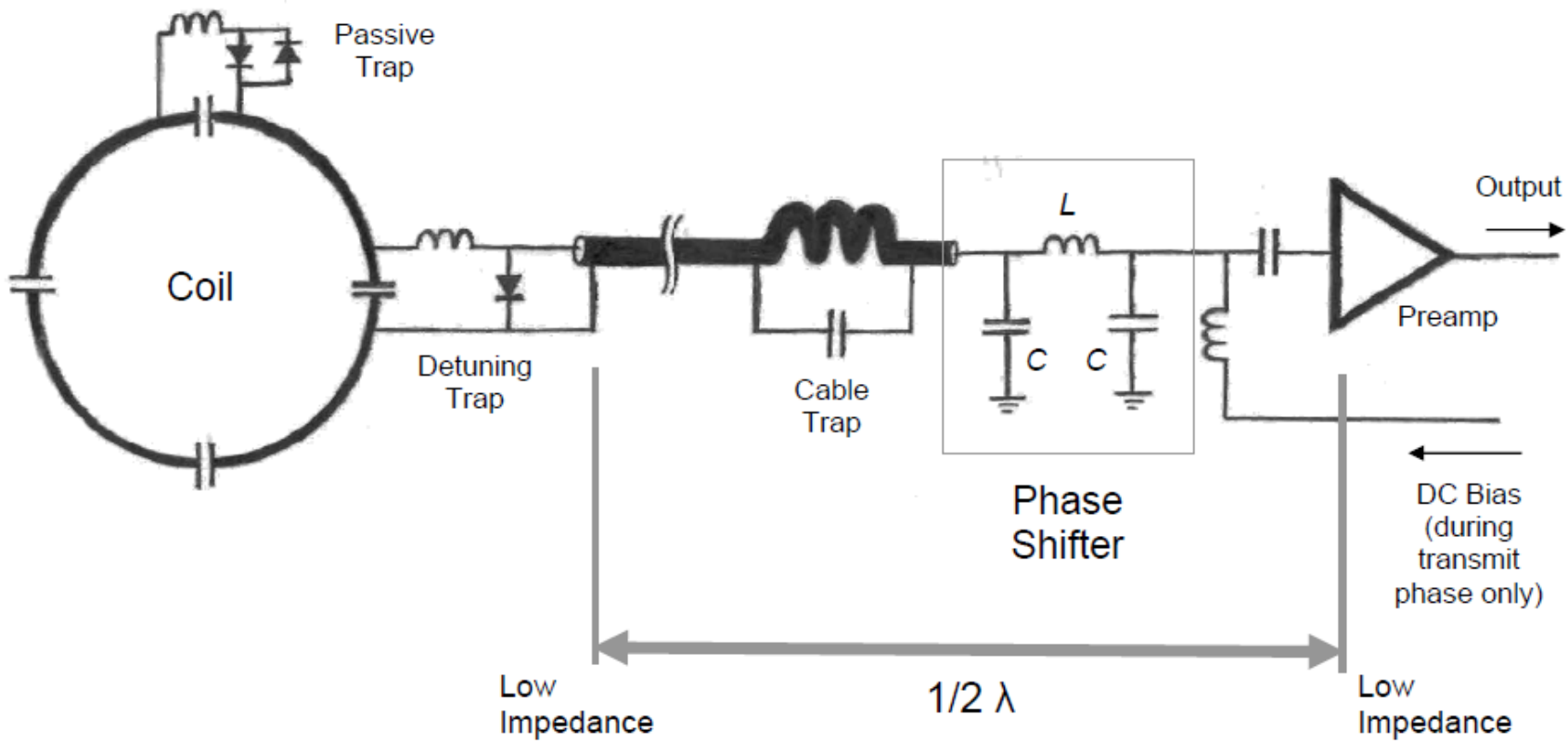


FIG. 2.68: Surface coil and supporting circuitry with preamplifier decoupling detailed.

Interestingly, preamplifier decoupling occurs during the *receive* phase of the MRI scan, rather than the *transmit* phase when active decoupling normally takes place. It may seem a paradox that the preamplifier circuitry causes the coil to become an open circuit during the receive phase, when the coil should be a closed-circuit resonator to receive the FID signal. There are two explanations for this fact. First, the preamp is designed to amplify *voltage* signals rather than *current* signals. Thus, most of the resonating current in the coil (induced by the FID signal) is blocked by the parallel resonance effect, but voltage signals are still received and successfully transferred to the preamp [32]. Second, preamplifier decoupling is not nearly as strong a decoupling method as active decoupling. Power transmission is reduced only by 18 dB, rather than the 30+ dB observed with active decoupling (see Figs. 2.69 and 2.70).

Since preamplifier decoupling reduces the magnitude of the current resonating in the coil, there is a significant reduction in the coil's induced magnetic field, and further, in the mutual inductance between coils. Little noise and signal are transferred between coils during receive mode as a result. Though preamplifier decoupling is not as effective a method for eliminating mutual flux as the direct overlapping of coil elements, it offers an effective solution to reduce the mutual inductance of nonadjacent coils that cannot be directly overlapped.

2.6 Parallel Imaging

The maximum rSNR available for imaging is determined by the coil geometry, scanner field strength, and sample properties and geometry – in general, the physical arrangement of the MRI setup. With knowledge of the desired final product, coil design

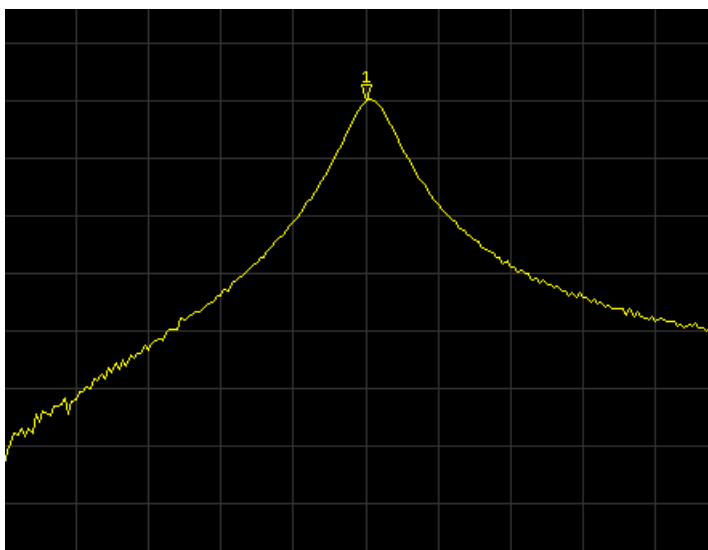


FIG. 2.69: S21 curve of an isolated coil without preamplifier decoupling. The resonant peak is at 123.23 MHz.

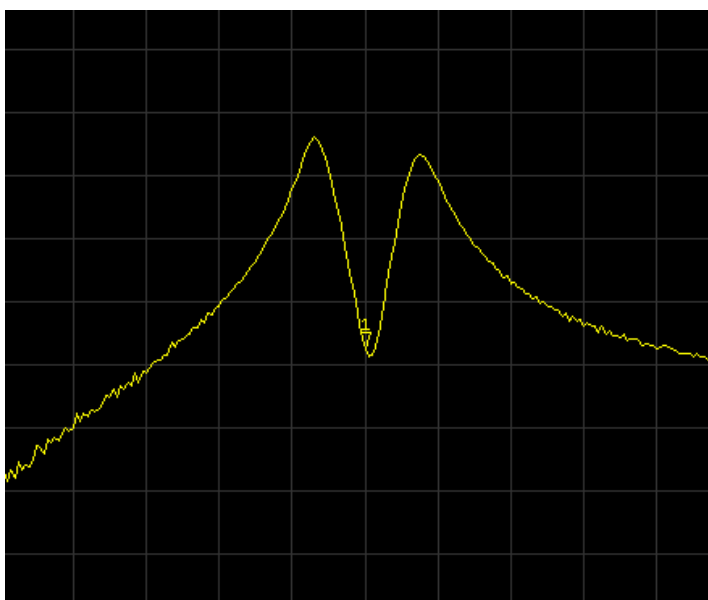


FIG. 2.70: S21 curve showing preamplifier decoupling applied. Power transmission at 123.23 MHz is decreased by approx. 18 dB.

can be optimized for different functions, i.e. imaging resolution, speed, etc., based on the clinical need.

Parallel imaging is a relatively new imaging technique that makes use of the unique position of each individual coil in the array. While ONC2 was not optimized for high imaging speed, both the high rSNR and the large number of coils serve to appreciably reduce imaging time if desired [10]. Equation 2.31 describes how the SNR of the final image when parallel imaging is applied ($SNR^{reduced}$) is lessened from the full SNR provided by the coil (SNR^{full}) [34]:

$$SNR^{reduced} = \frac{SNR^{full}}{G\sqrt{R}} \quad [2.31]$$

The two terms in the denominator of Equation 2.31 dictate the performance of parallel imaging. The second term, called the reduction factor R , refers to the number of samples that are skipped when signal data is being acquired by the scanner. In other words, during normal imaging, k -space is filled in along k_x , one k_y -line at a time [35]. During parallel imaging, only every ‘ R ’-th line is sampled. Since decreasing the sample density reduces the field of view, the final image is produced with heavy aliasing. However, if the aliasing can be fixed during postscan processing, then skipping lines of k -space essentially translates into faster imaging.

The other denominator term in Equation 2.31, called the geometry factor (G -factor), quantifies how well the aliasing problem from an increased reduction factor can be overcome. G -factor is a per-voxel measurement, and is based on the ability of the image reconstruction algorithm to resolve individual voxels’ signal from the complex

FID ensemble. By way of illustration, the red dot in Figure 2.71 represents the signal from a single voxel. Because the signal can be uniquely identified by the single coil loop on the left, the G-factor for this voxel is very low; ideally the G-factor would be unity. However, if a different coil layout were used as shown in Figure 2.72, signal from the same voxel is detected by a number of coils. When such a coil is used, the reconstruction algorithm would have a more difficult time determining the origin of the signal. The G-factor of the voxel is thus increased, and the resulting SNR of the image is reduced. Since the unique sensitivity profile of each coil loop helps ‘fill in’ missing k-space information during parallel imaging, the formal name for this technique is *SENSitivity Encoding*, or ‘SENSE’.

G-factor is strongly determined by the geometry of the receiver coil (loop layout, loop size, etc.) and the location of the sample relative to the coil. Typically, voxels in the sample that are nearest a specific coil have low G-factors, since that coil functions as the dominant receiver. However, the signal from voxels in the center of a sample is often received equally well by multiple coil loops. The G-factor of those voxels would be quite high. Thus, with a general knowledge of the desired anatomy to be imaged, the rSNR of a coil can be optimized based upon the specific clinical need, i.e., the need for increased imaging speed or increased resolution.

2.7 Conclusion

This chapter has provided an overview of the basic principles and practice for RF receive coil design in magnetic resonance imaging. Although the descriptions and illustrations focused on brain imaging, the physics apply for any anatomy of interest. The

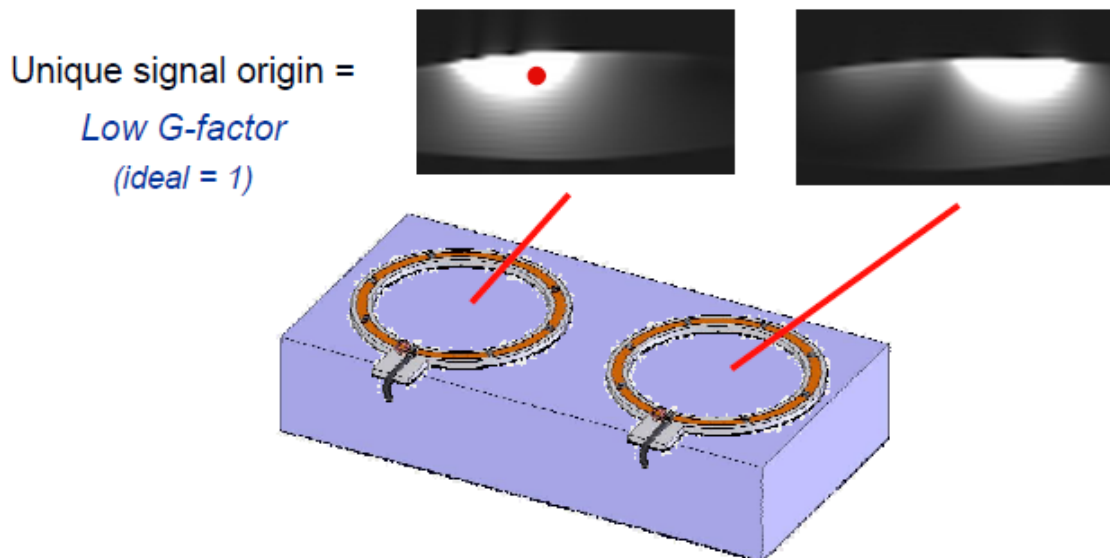


FIG. 2.71: A voxel is said to have a low G-factor if its location can be uniquely determined.

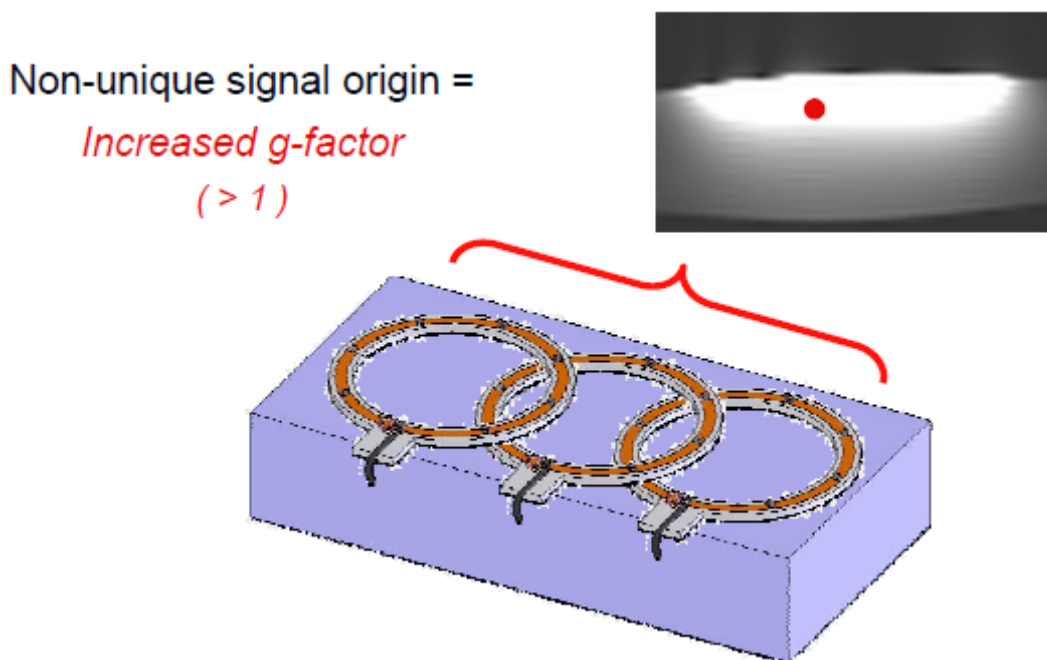


FIG. 2.72: A voxel has a lower G-factor the left and center coils have equal claim to the voxel's location.

theory, measurement methods, and skills described in this chapter were accumulated from the references cited, numerous advisor explanations, and a great deal of trial and error experience, during the construction and testing process of ONC2. The purpose of this background chapter is to foster an intuitive understanding of coil theory, and to function as an instructive guide and for efficient coil design and construction.

CHAPTER 3

METHODS AND COIL CONSTRUCTION

When the 20-channel coil (“ONC1”) was presented at the International Society of Magnetic Resonance in 2007 [13], it evoked a great deal of feedback from the coil community, indicating a possible need for constructing a new coil. It was suggested that the use of copper wire rather than copper foil as a coil conductor would lead to reduced capacitive coupling between loops, and minimize an effect known as flux shielding [12]. Also, it was recommended that including more coil channels to cover the entire head would lead to increased rSNR and parallel imaging performance.

Because of the high interest at the University of Utah in screening for Multiple Sclerosis, funding was provided through the Cumming Foundation and Dr. John Rose of the Brain Institute to construct a new coil (“ONC2”) for imaging optic neuritis. The features discussed at the conference mentioned above were to be utilized in the new coil, namely, using wire loop coil elements arranged to cover the entire head. In addition, a collapsible mask design was to be employed to achieve higher rSNR for patients with different head sizes.

Many coil development tools were required before construction could begin on the optic nerve coil itself. These tools were researched, designed, and fabricated to augment the construction process. Optimizing the physical construction of the individual

coil channels was also an important task to perform before actual coil construction. Since each loop placed on the helmet would potentially be overlapped by up to 6 adjacent loops, maximizing the coil sensitivity by selecting the proper construction technique was crucial to obtain maximum rSNR. This process involved a number of preliminary studies.

While the purpose of the preliminary studies was to optimize the sensitivity of the individual coil elements, verifying the advantages of using copper wire over copper foil as the coil conductor was not a specific aim of this thesis. Many studies could be performed on this topic alone. Thus, the topic will be discussed in the “Future Work” section of this thesis, included in Chapter 5.

3.1 Preliminary Work

3.1.1 Phantom Construction

A fiberglass mold filled with a CuSO_4 solution [36] was made to serve as an imaging phantom for the coil (Fig. 3.1). Using a phantom allowed the laborious process of coil construction, tuning, and overlapping to take place without the constant use of a human volunteer. While a phantom does not perfectly mimic a human sample load, the proper copper sulfate concentration provided T_1 and T_2 relaxation time constants to very nearly simulate the conductive properties of the brain. Table salt (NaCl) was later added to the phantom until the load approximately matched that of a human head. After construction and testing of the coil with the phantom, the coil would be retuned to a human head for volunteer and patient studies.

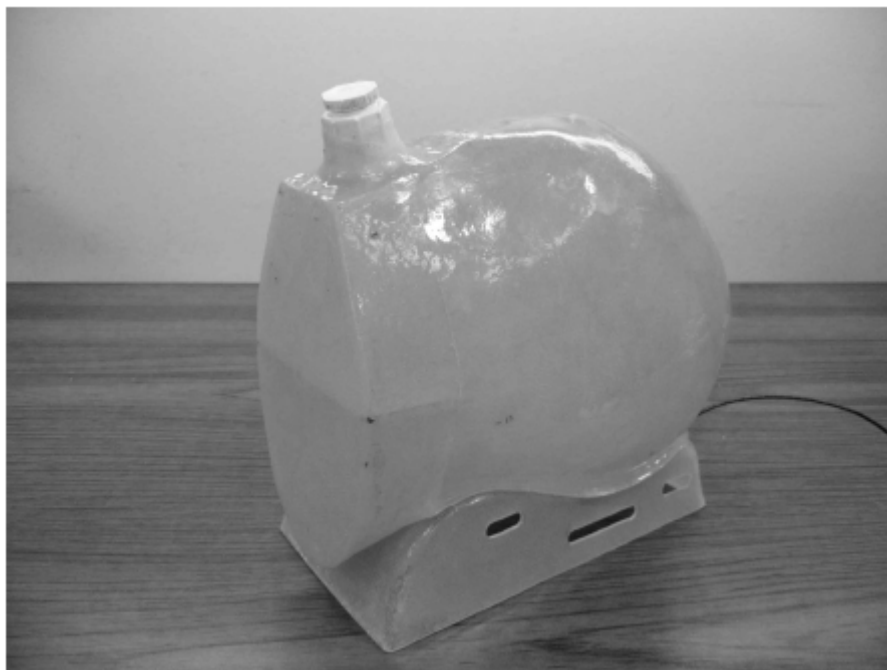


FIG. 3.1: Fiberglass head imaging phantom filled with a solution of CuSO_4 and table salt (NaCl).

3.1.2 Double-loop (S_{21}) Measurement Probe

A measurement tool was required for the process of coil decoupling. Hoult describes a method of constructing a pick-up loop suitable for obtaining resonant frequency measurements from individual coil elements [37]. The loop is configured in such a manner (Fig. 3.2) that an applied current creates a magnetic field, which excites a nearby coil by mutual inductance. Stray or conservative electric fields are contained within the insulator region of the probe loop, and nonconservative electric fields are suppressed due to a small gap in the outer conductor. When two such loops are used in conjunction, the transmit loop excites a nearby coil and the receive loop detects the resonating magnetic field, allowing S_{12} measurements to be read from a network analyzer. By reciprocity, either loop can act as transmitter or receiver. The setup explained in Chapter 2 (Fig. 2.33) is a standard coil measurement method, where the two Hoult pick-up loops are placed on either side of the coil under test. However, a convenient handheld probe can be fashioned by overlapping the two loops to reduce their own mutual inductance to zero. In this arrangement the two loops function as though physically separated (Fig. 3.3).

3.1.3 Q Test Jig

Measuring the Q of a coil is notoriously very difficult, requiring extreme stability as the coil load is placed in proximity to, then removed from, the coil itself. The difficulty of measurement is only increased when the Q of two or more coils must be compared accurately. In this case, the coils must be repositioned precisely in relation to the coil load and the measurement probe. In response to the inconsistencies encountered

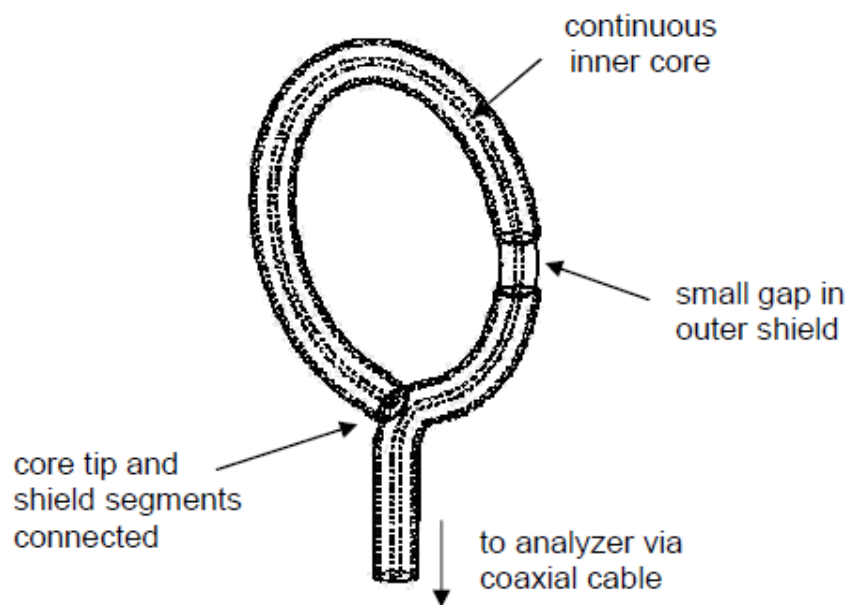


FIG. 3.2: Diagram of the Hoult pick-up loop.

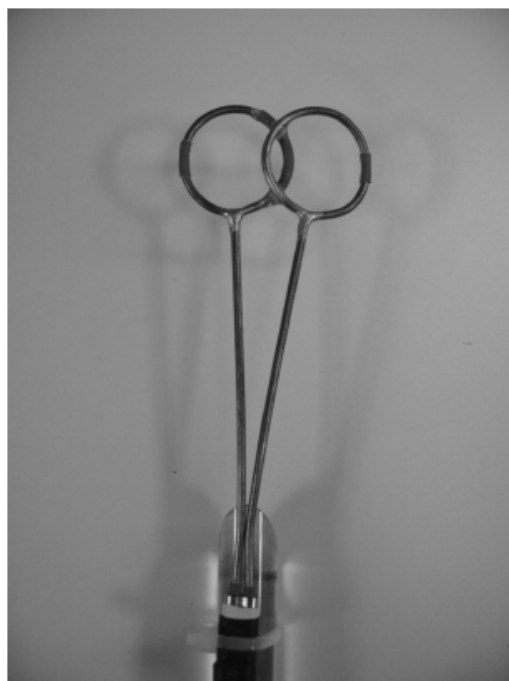


FIG. 3.3: Handheld S_{21} probe employing two Hoult pick-up loops overlapped to reduce their own mutual magnetic coupling to zero.

when the early Q comparisons for this project were performed, the rigid Q testing jig shown in Figure 3.4 was designed and constructed. The loading phantom can be slid in and out on two rails beneath the coil while the measurement probe remains rigidly fixed. In addition, the coil itself can be interchanged with repeatability.

3.1.4 Test Board

Constructing a test board was essential to simulate the coil interface of the MRI table in the lab (Fig. 3.5). The board supplies the DC bias voltage that is necessary to detune the coil loops, allowing each loop to be turned ‘on’ or ‘off’ independently. The preamps, used to amplify the signal from each coil, are also supplied from the test board with the necessary power to provide gain. Providing preamp power as a built-in feature eliminated the need for a separate preamp testing jig, and permitted the measurement of noise figure through the entire coil assembly.

3.1.5 Study #1: Variable Capacitor Q

Variable capacitors were used to tune and match the individual coil elements of ONC2. Chip capacitors are preferable for long term reliability, but would not have been practical since frequent changes had to be made to the tune and match capacitor values during the coil overlapping process. Thus, using variable capacitors saved a great deal of construction time.

Q was measured and sensitivity calculated for several types of variable capacitors available in the lab. The sensitivity measurement for each trimmer was taken after a single test coil was assembled with the trimmer in both the tune and match locations. The interleaved and dielectric style capacitors were found to be comparable in their

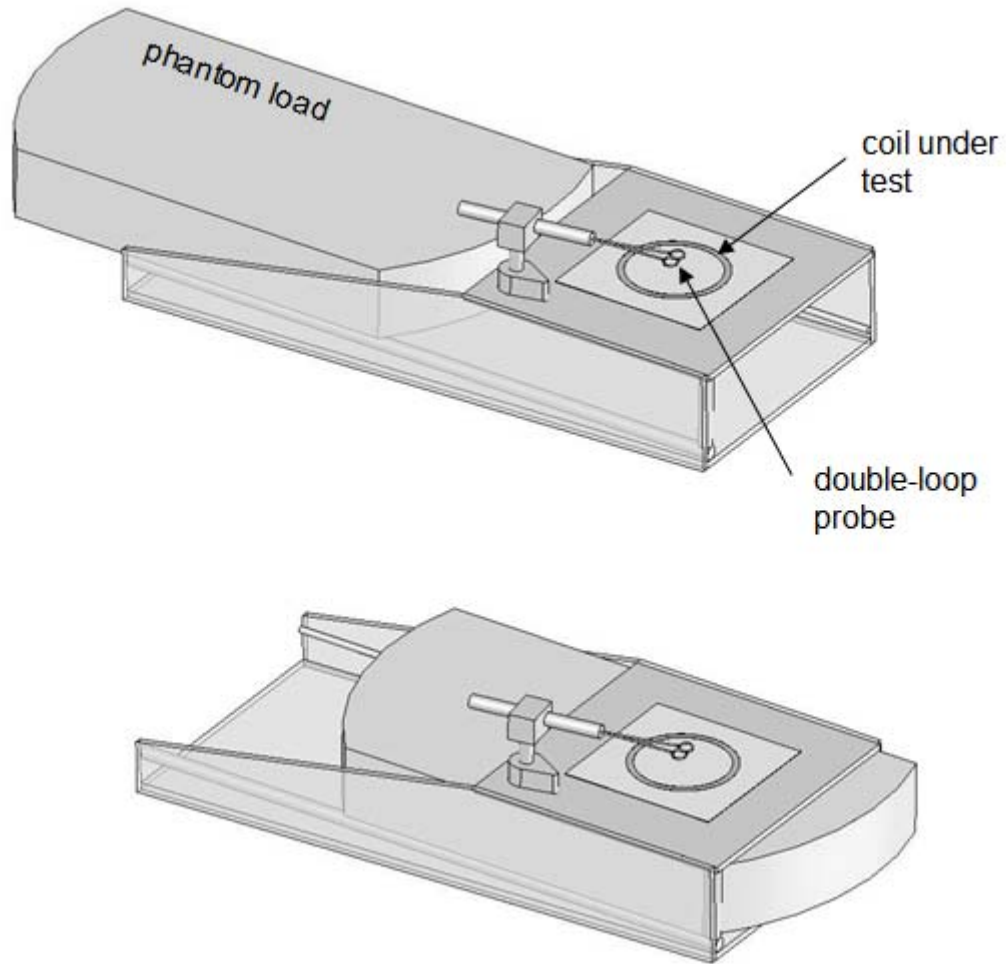


FIG. 3.4: Coil Q testing jig, with the coil-under-test placed on the measurement platform, shown in the unloaded state (top) and loaded state (bottom); the Hoult double-loop probe is rigidly fixed during all tests.

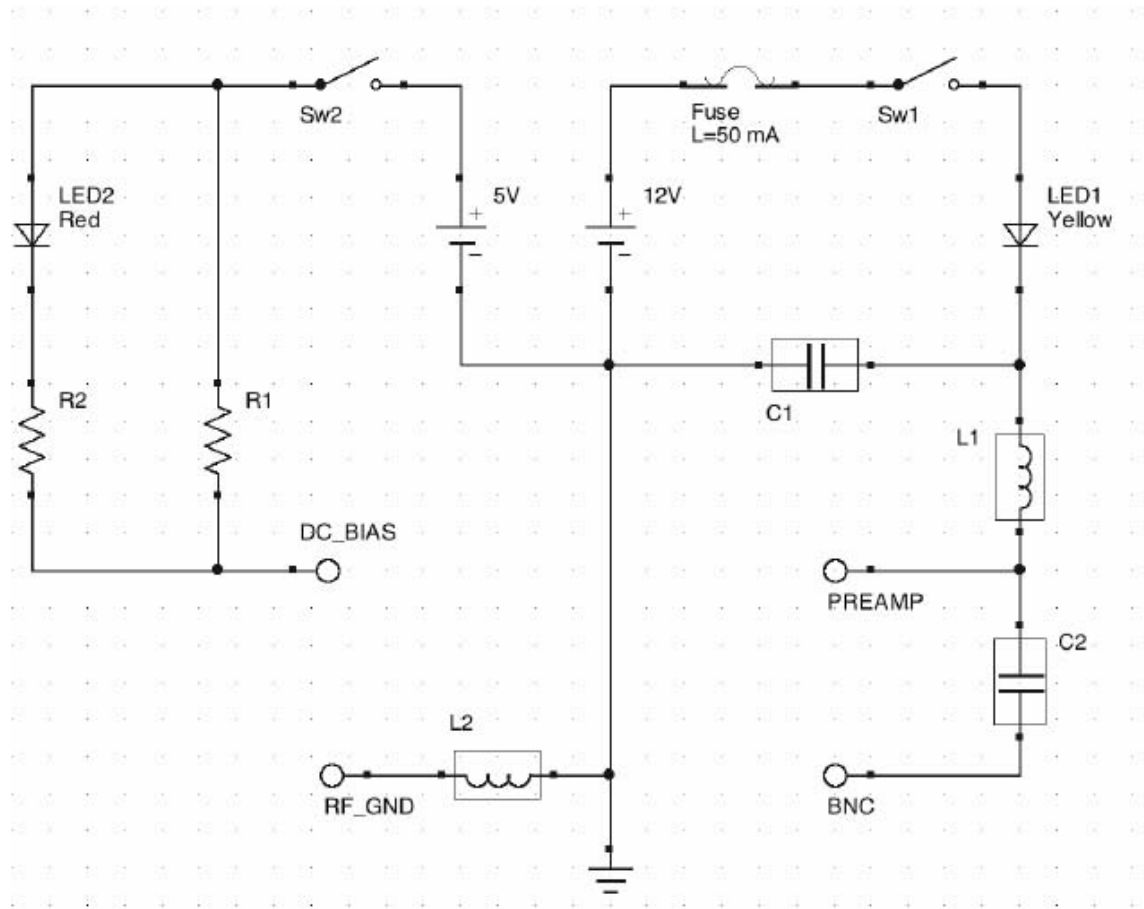


FIG. 3.5: Schematic of switching and bias-T electronics of the lab MRI table simulator. Only one of 32 total channels is shown.

performance (see Table 3.1). However, due to the drastic price difference, the multiturn dielectric style (\$22 each) was only utilized when extreme precision was required, i.e. for the coils immediately near the optic nerve pathway. Otherwise, the interleaved style (\$1.50 each) was used due to its low cost and ease of soldering.







3.1.6 Study #2: Coil Construction Parameters

3.1.6.1 Initial Tests

Q tests were performed with isolated test coils to determine ideal construction characteristics for the optic nerve coil. Initially, the test coils were measured using the setup described in Chapter 2 (Fig. 2.33), before the Q testing jig described in section 3.1.3 was completed. These initial measurements proved to be not as accurate as later measurements using the jig. However, they are included here because they influenced the early coil construction decisions that were made.

The following three design parameters were studied in detail: (1) coil loop diameter, (2) wire gauge (or thickness of the coil conductor wire), and (3) number of capacitors equally spaced around the coil loop. Foil loops were also included in the study to determine any preliminary difference in Q between isolated loops made of wire or foil, prior to their insertion into an array. The three test parameters listed are important because each one influences the electromagnetic properties of the coil. Each coil has a characteristic inductance, capacitance, and loss, which is affected by the construction method. Reducing the coil loss was the primary focus of this study, since it correlates directly to the sensitivity of the coil.

TABLE 3.1: Comparison chart of various trimmer capacitors, shown in order of increasing sensitivity when measured on the constructed test coil.

	Part #	Coil Sensitivity (Q_U / Q_L)	Type	Range	Price Mouser.com, '09
	GKY30066	2.021	Ceramic	6 - 30 pF	\$1.00
	N/A	3.555	Ceramic	N/A	N/A
	N/A	3.593	Ceramic	N/A	N/A
	JZ300	4.028	Ceramic	3 - 15 pF	\$3.00
	GYA36000	4.295	Interleaved	3 - 36 pF	\$1.50
	A1J12	4.411	Dielectric	1.6 - 12 pF	\$22

Investigating the number of distributed loop capacitors was a particular focus of this study due to an important trade-off: a greater number of capacitors around the coil tends to increase the *resistive loss* of the coil, which decreases the coil unloaded Q. However, a greater number of capacitors also decreases the *sample loss* of the coil by reducing the stray electric field through the sample. As discussed in section 2.3.3: Electric Fields and Coil Noise, reducing the sample loss decreases the amount of noise received by the coil.

A total of eight individual test loops were investigated to determine any sensitivity improvements from one loop configuration to another (see Fig. 3.6). The Q measurements obtained from the test coils (Table 3.2) demonstrated that loops constructed using wire rather than copper foil generally produce more sensitive coils. Since Q measurements are notoriously very troublesome, and the data was not always consistent, rSNR studies of the test coils were performed to supplement the sensitivity data. Gradient Echo and noise-only tests were performed with each test coil using a phantom load in the MRI scanner. However, the resulting rSNR data from each coil was equally inconclusive. Thus, the number of capacitors was chosen to be three for convenience in overlapping coils with hexagonal layout geometry.

3.1.6.2 Revised Q Tests

After the Q testing jig described in section 3.1.3 was completed, Q measurements of the test coils were repeated using the jig. In this case, test coils of various wire gauges were substituted for the small (5.5cm) coils, because such small coils were not used in the

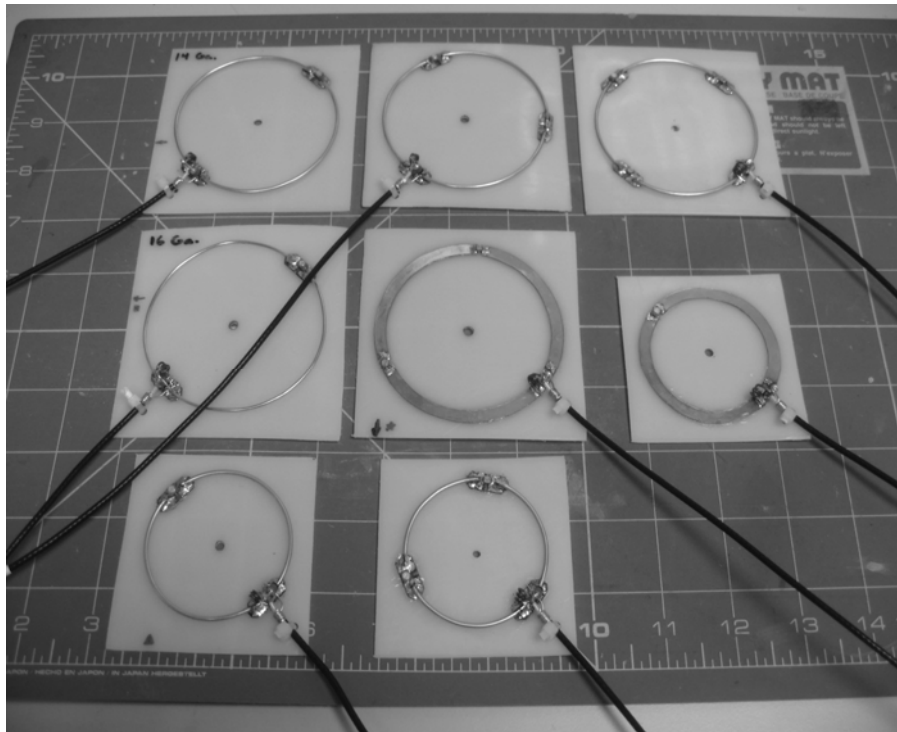


FIG. 3.6: Sample coils from Q and rSNR tests of coil construction parameters. A total of 16 individual test loops were constructed, 8 of which are shown here.

optic nerve coil itself. The revised results are shown in Table 3.3. As can be seen in comparing Tables 3.2 and 3.3, the newly developed jig provided Q values that were much more consistent across similar coil types, as the number of distributed capacitors was changed. Though the highlighted configuration in Table 3.3 (14-gauge wire with three distributed capacitors) was selected from the previous Q study, it proved to be a suitable compromise between sensitivity and construction expediency.

3.2 Construction Procedure

The optic nerve coil in this study was constructed using two fiberglass formers that fit together to surround the entire head (Fig. 3.7). The mask, or anterior former, was created from the plaster mold of a relatively generic human head. The posterior former supports the neck and head, and was molded from a commercially available foam head rest. Both formers were made symmetric by hand, then trimmed to slide over one another to accommodate any arbitrary head size. In this design, the coils maintain close coupling near the eyes and around the head in general, to eliminate the air void regions that occur between the coil elements and the head when smaller heads are imaged in one-piece, nonadjustable coil formers.

The MRI scanner available for research study provides support for up to 32 coil channels. However, four of these channels are accessed by a four channel plug, which was unavailable to implement into the coil design. Thus, the number of channels was limited to 28: 26 coil elements were reserved for placement on the mask, and the remaining two coils were housed in the posterior headrest former.

TABLE 3.2: Initial Q results for the various coil configurations shown in Fig. 3.6. 14-gauge wire with three distributed capacitors (highlighted) was the selected configuration.

Coil Type (7cm dia.)	# Caps	Sensitivity (Q_U/Q_L)
Foil	3	10.0
Wire – 14 ga.	2	10.8
Wire – 14 ga.	3	10.4
Wire – 14 ga.	4	11.4
Wire – 16 ga.	2	11.6
(5.5cm dia.)		
Foil	2	5.0
Wire – 14 ga.	2	5.4
Wire – 14 ga.	3	4.4

TABLE 3.3: Data from a revised Q study using the test jig shown in Fig. 3.4. The highlighted configuration (14-gauge wire with three distributed capacitors) was selected from the previous Q study.

Coil Type	# Caps	Sensitivity (Q_U/Q_L)
Foil	2	11.44
Foil	3	11.03
Foil	4	9.26
Wire – 14 ga.	2	11.05
Wire – 14 ga.	3	10.26
Wire – 14 ga.	4	9.82
Wire – 16 ga.	3	10.05
Wire – 18 ga.	2	9.74

In order to achieve maximum head coverage with 26 channels, a mesh made of elastic cord and metal O-rings was created to duplicate the hexagonal/pentagonal geometry of a soccer ball [11]. This mesh, shown in Fig. 3.8, allowed simultaneous adjustment of loop size around the entire mask, while still maintaining the proper geometry. Another advantage was allowing the surface area of the individual elements to be enlarged or reduced depending upon their position relative to the location and depth of the optic nerve region to obtain maximum rSNR [31]. Along the optic nerve pathway, the coils were arranged so that overlapping would occur in the transverse (X - Y) plane for maximum signal sensitivity, as discussed in Chapter 2 (Figs. 2.52 – 2.54).

Once secured, the vertices of the mesh were transferred to the fiberglass former, and the layout pattern was reproduced with a pen to guide coil placement (Fig. 3.9). The coil was assembled by circumscribing the bent wire loops around the pentagonal and hexagonal shapes of the marked layout geometry. Small bridges were formed into the wire at the overlap points to reduce the capacitive coupling between coils. The ends of the bent wire segments of each coil were soldered to fiberglass pads, as were the tune and match capacitors. Since these solder pads were fastened to the former by epoxy, it was thought that they would provide a sturdy anchor to the former while allowing the wire segments to flex when the former is fitted to a patient. The two headrest coils (Fig. 3.10) were overlapped to reduce coupling, and tuned and matched to a load separated by 1 cm of foam padding for comfort.

Proper mounting of the amplification electronics was an important mechanical hardware design consideration of ONC2. The quality of images produced by the coil depends highly upon the repeatable positioning and immobilization of the patient, so an



FIG. 3.7: Collapsible mask/headrest design (foam padding on headrest not shown).

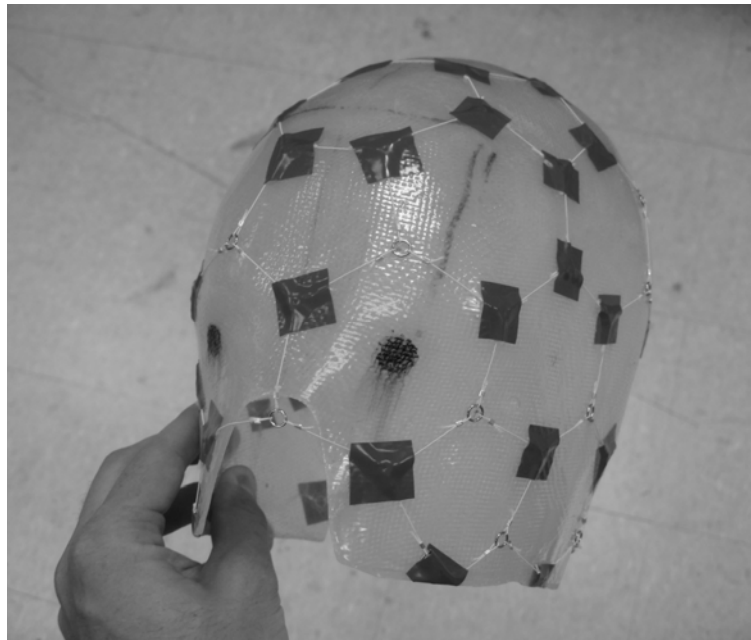


FIG. 3.8: Mask former with stretchy mesh used to create coil layout pattern (vertices secured to fiberglass with tape).

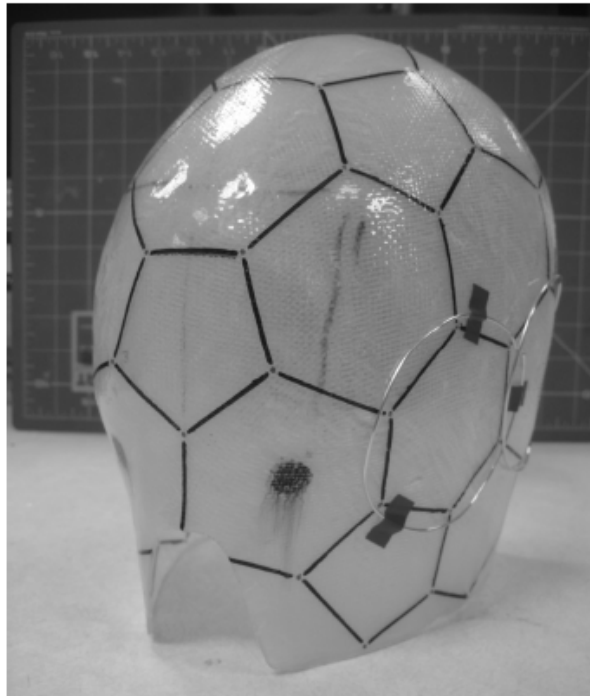


FIG. 3.9: Coil pattern transferred to mask former to guide coil placement.

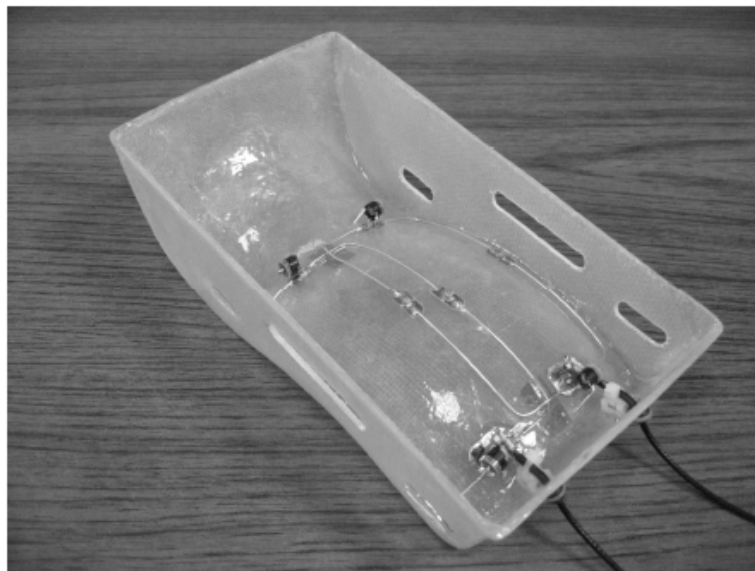


FIG. 3.10: Headrest with two rectangular coils overlapped in the transverse plane (shown in upside-down position).

acrylic mounting apparatus was devised to provide sufficient room around the head for stabilization by a plastic (PVC) arch (Figs. 3.11 and 3.12). The unit was made to be self contained, allowing technicians to easily install and remove the coil from the MRI table.

As a result of using the stretchy mesh method of coil layout, all 26 coil elements placed on the mask former of ONC2 were of dissimilar diameter, ranging from 6 cm to 10 cm. The coils placed immediately along the optic pathway region were overlapped in the transverse plane to provide as much rSNR as possible (Fig. 3.13), since the optic pathway was the primary region of interest. The coil layout pattern of ONC1 is shown in Figure 3.14 for comparison. ONC1 was constructed using coils of 5.5 cm diameter on the sides of the mask, and 7 x 6 cm elliptical coils over the eyes and forehead.

Each wire element of ONC2 was tuned and matched as an isolated antenna to the phantom load. Variable capacitors at the tune and match points of the coil provided a quick and relatively reliable means of adjustment. While tuning each coil loop, a single chip capacitor was removed from each of the other 25 loops to render them nonresonant [Wig06]. In addition, each coil was equipped with a detuning trap at the match point of the loop. In the completed array, individual coils were alternately switched on and off to verify that coil-to-coil interactions were minimized.

ONC2 was tested initially in the MRI scanner by using a Gradient Echo (GRE) scan sequence and a phantom load. Matlab was used to analyze the image data obtained from the scanner. Matlab programs are available to compute the noise correlation among the coil loops, which accurately quantified the degree of decoupling (if two loops were not properly overlapped, the mutual inductance was not zero, and a large quantity of noise was shared between the loops). Matlab was also employed to produce rSNR maps

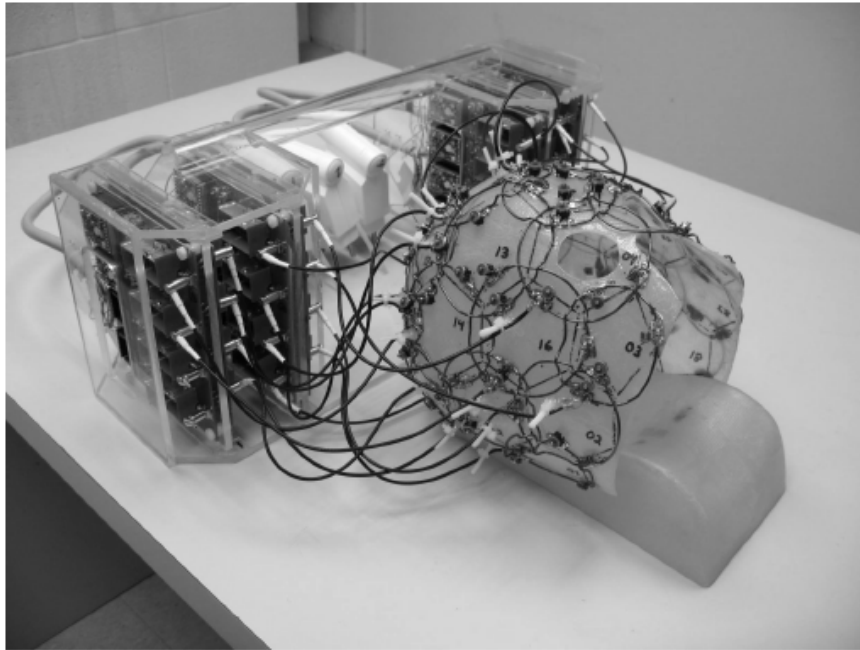


FIG. 3.11: Completed 28-channel optic nerve coil (“ONC2”) with the accompanying preamp board electronics.

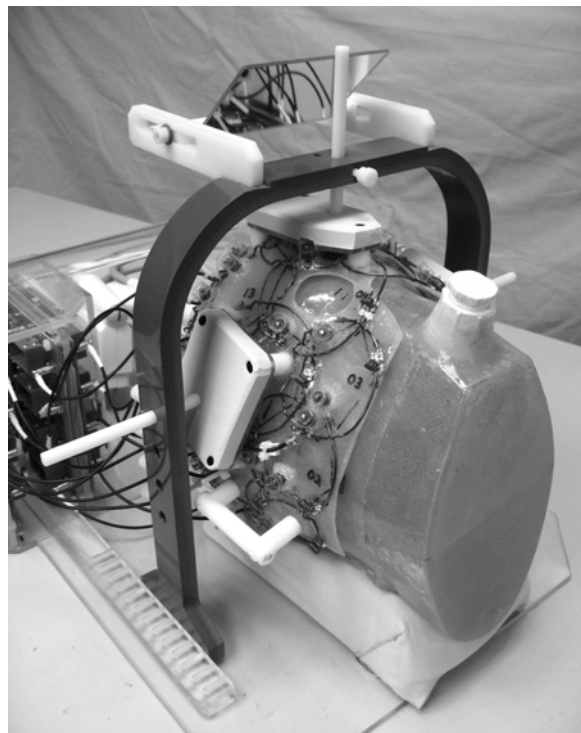


FIG. 3.12: Arch system for rigidly securing the head, including an adjustable mirror.

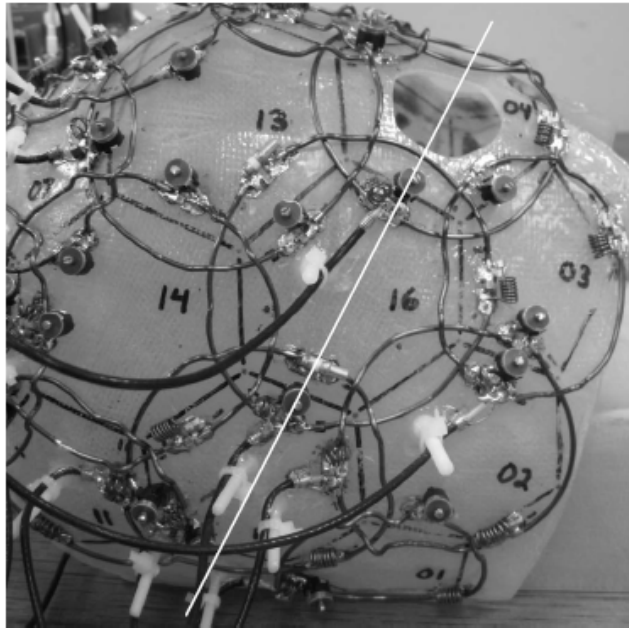


FIG. 3.13: Coil overlap pattern of ONC2, with patient right side shown. Superimposed line indicates the optic pathway.

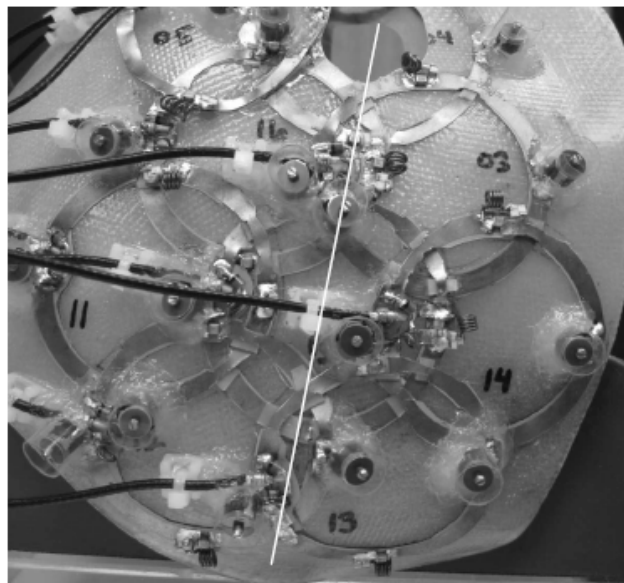


FIG. 3.14: Coil overlap pattern of ONC1, with patient right side shown. Superimposed line indicates the optic pathway.

illustrating the signal reception uniformity. As any abnormalities were observed, the offending coils were examined and fixed, and the test scans repeated. Finally, when all coils appeared to behave properly, the phantom studies of Chapter 4 were initiated. Following these studies the coil was tuned to a human head (a volunteer) and human volunteer and patient scans were performed.

CHAPTER 4

IMAGING RESULTS

The purpose of this thesis has been to improve the study of optic neuritis through the construction of a new coil (“ONC2”) specifically designed to image the optic nerve tract. This chapter shows how the various design features implemented in the construction of ONC2 have significantly increased the quality and effectiveness of optic nerve imaging.

Numerous advanced phased-array head coils have been developed in recent years for general brain imaging [8, 9, 10, 11, 12], with designs ranging in complexity from 4 to 96 channels. These coils have typically been constructed using dome-shaped, ‘one size fits all’ helmet structures to allow room for a wide range of head sizes. However, when used for optic nerve imaging, coils with rigid formers tend to fall short of their intended SNR capability. This is due to the large void regions occur around a patient’s head when the coil is too large or otherwise not well fitted. These gaps separate the receiver coils from the desired anatomy and result in reduced rSNR compared to the available intrinsic rSNR [4].

The first prototype optic nerve-specific coil (“ONC1”) built at UCAIR was constructed as a tight-fitting mask to overcome the typical problem of coil-to-anatomy separation. When ONC1 was presented at the 15th annual ISMRM conference [13], it

evoked numerous comments from the coil hardware community. The ensuing discussions involved the benefits of using copper wire, rather than copper foil, as the conductor material of each coil element [12]. Increasing the number of coil elements to achieve full head coverage, rather than a simple mask design, was also generally encouraged. In addition to the ideas gathered at the ISMRM meeting, a novel method of achieving full head coverage by arranging coil elements in soccer ball geometry was published [11]. In response, a second generation optic nerve imaging coil (“ONC2”) was constructed atUCAIR. Many of the suggested design ideas were merged into a single coil in order to provide increased imaging performance over general purpose brain coils in the study of optic neuritis. Specifically, the following major design improvements were implemented in the design of ONC2:

- (1) The coil layout of ONC2 consists of 26 loops arranged in a soccer ball pattern surrounding the face as a mask, with an additional two loops in the head/neck support, for full head coverage.
- (2) The fiberglass formers of ONC2 feature a collapsible design, allowing the mask to remain very near the face regardless of the head size of the patient.
- (3) The individual coil elements were made using copper wire in order to reduce magnetic flux limitation through the coil.

The bulk of this chapter is comprised of three sections. First, a detailed account is given of the improved imaging performance from the 28-channel, full head coverage coil layout of ONC2. Second, the rSNR contribution from the collapsible former design is reported. For these studies, both ONC1 and the Siemens 12-channel rigid head coil were used as comparison benchmarks from which the relative performance improvement of

ONC2 was measured. All scans were performed using a Siemens 3T TIM Trio scanner [Siemens Healthcare AG, Erlangen, Germany]. A 2-D gradient echo (GRE) sequence was used with a 2x2x5mm voxel size and TR/TE/flip of 500ms/4.38/90°, respectively. The sum of squares recombination method was used to produce the final images [32]. The third and final section of the chapter briefly covers the results from a number of investigational clinical trials that were performed with optic neuritis patients using ONC2. The pulse sequences employed during these scans are mentioned as appropriate.

4.1 – Coil Layout Comparison Studies

4.1.1 – rSNR Comparison of Coil Layout

For the coil layout study of ONC2, the previous generation optic nerve imaging coil known as ONC1 was used as a comparison benchmark because of its similar mask design. Although both ONC1 and ONC2 fit normal volunteers equally well during clinical trials, their respective, dedicated phantoms could not be interchanged for direct rSNR comparison between the two coils because ONC2 was made to fit a newer, more symmetric head phantom. To solve this problem, both phantoms were individually scanned using the Siemens 12-channel head coil (Figs. 4.1 – 4.3). From these scans, an rSNR reference baseline was produced so that the rSNR improvements of ONC1 and ONC2 could be compared directly. Both phantoms were filled with a CuSO_4 solution from the same batch.

Figure 4.4 shows a direct rSNR comparison of ONC1 and ONC2 when imaged in the scanner with their respective phantoms. The data from each coil was normalized by



FIG. 4.1: “PH-1” – dedicated phantom for ONC1



FIG. 4.2: “PH-2” – dedicated phantom for ONC2

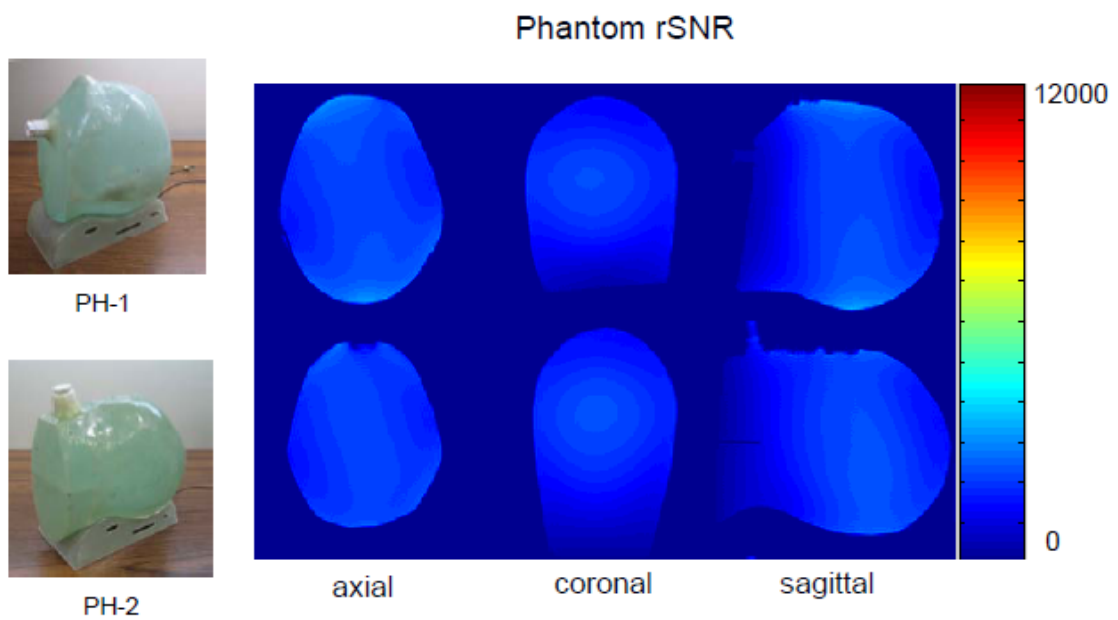


FIG. 4.3: rSNR data obtained from the Siemens 12-channel coil for each phantom

its respective phantom baseline. Due to the relatively large size of the ONC2 coil elements, the measured rSNR at the surface of PH-2 is not as high as PH-1. This observation can be made especially well in the axial plot of ONC2: not as much high-magnitude 'red color' is seen at the phantom surface, except for a regular 'hotspot' pattern that is due to the overlap regions in the transverse plane along the optic pathway. However, a slightly greater imaging depth due to the larger coil size of ONC2 can be observed. Higher available rSNR at the center of the head allows higher resolution imaging of the optic chiasm to be performed. The two large coils in the headrest of ONC2 contribute to this greater region of sensitivity as well.

Profile plots were produced in Matlab® from the axial data of each coil shown in Figure 4.4. Figure 4.5 illustrates the coronal and sagittal data profiles, which are then compared in Figures 4.6 and 4.7 as the relative SNR plotted against image pixels. Immediately noticeable in these plots is the significant rSNR increase at the chiasm exhibited by ONC2. Since the individual loops of ONC2 are larger than those of ONC1, the rSNR at the surface of PH-2 is lower in the coronal profile, but falls off less rapidly. The rSNR contribution of the back elements of ONC2 can be seen in the sagittal profile.

In order to quantitatively determine the rSNR performance increase of ONC2 over ONC1, the average rSNR was calculated [1] over four different regions of interest. These regions, shown in Table 4.1, approximately represent the anatomy of interest along the optic pathway. Table 4.2 compares the rSNR increase of both ONC1 and ONC2 over the Siemens 12-channel coil, with the Siemens coil set as the comparison baseline.

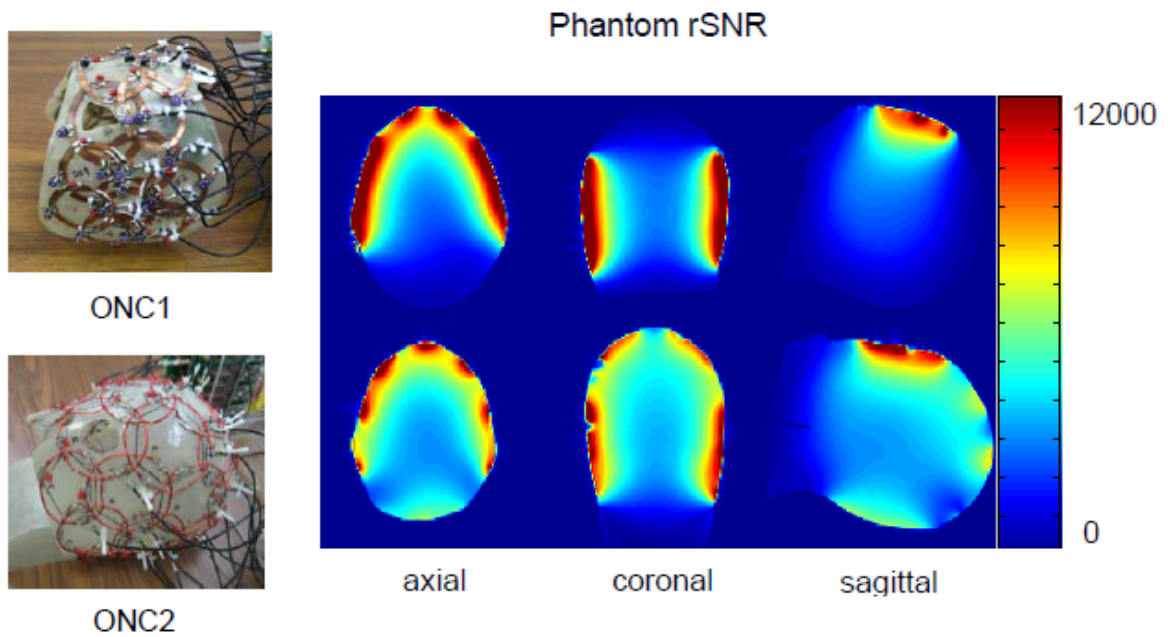


FIG. 4.4: Phantom rSNR comparison of ONC1 (top) and ONC2 (bottom).

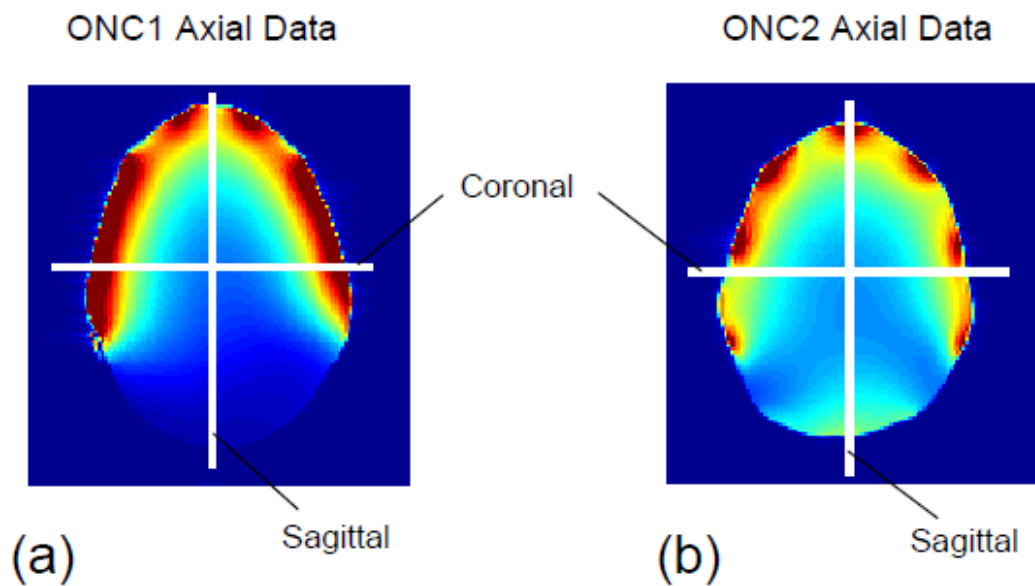


FIG. 4.5: Coronal and sagittal data profiles taken from axial plots of Fig. 4.4. (a) ONC1 axial data. (b) ONC2 axial data.

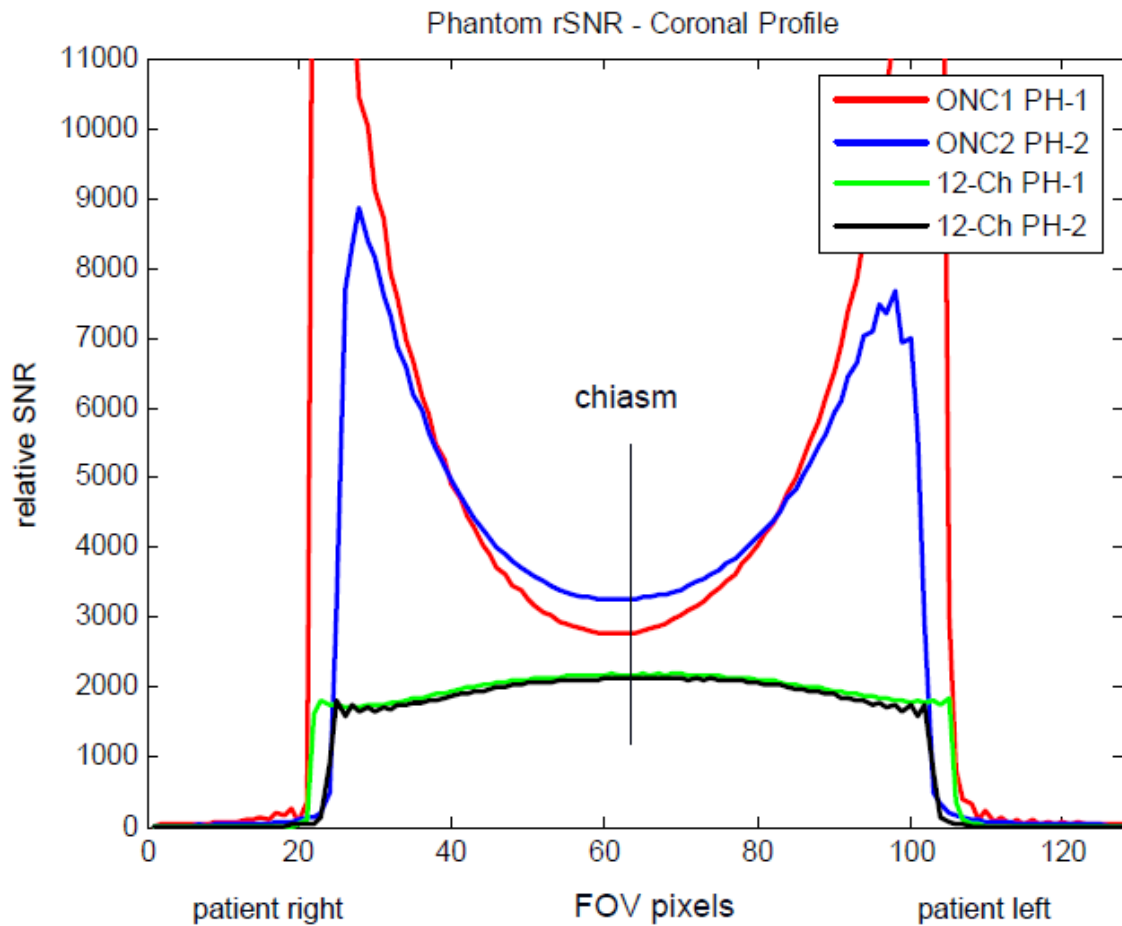


FIG. 4.6: Coronal profile data plots of ONC1 (20-Ch, red) and ONC2 (28-Ch, blue) with respective phantoms, and the phantom baseline plots with the Siemens 12-channel coil (green, black). The approximate side-to-side location of the optic chiasm is labeled.

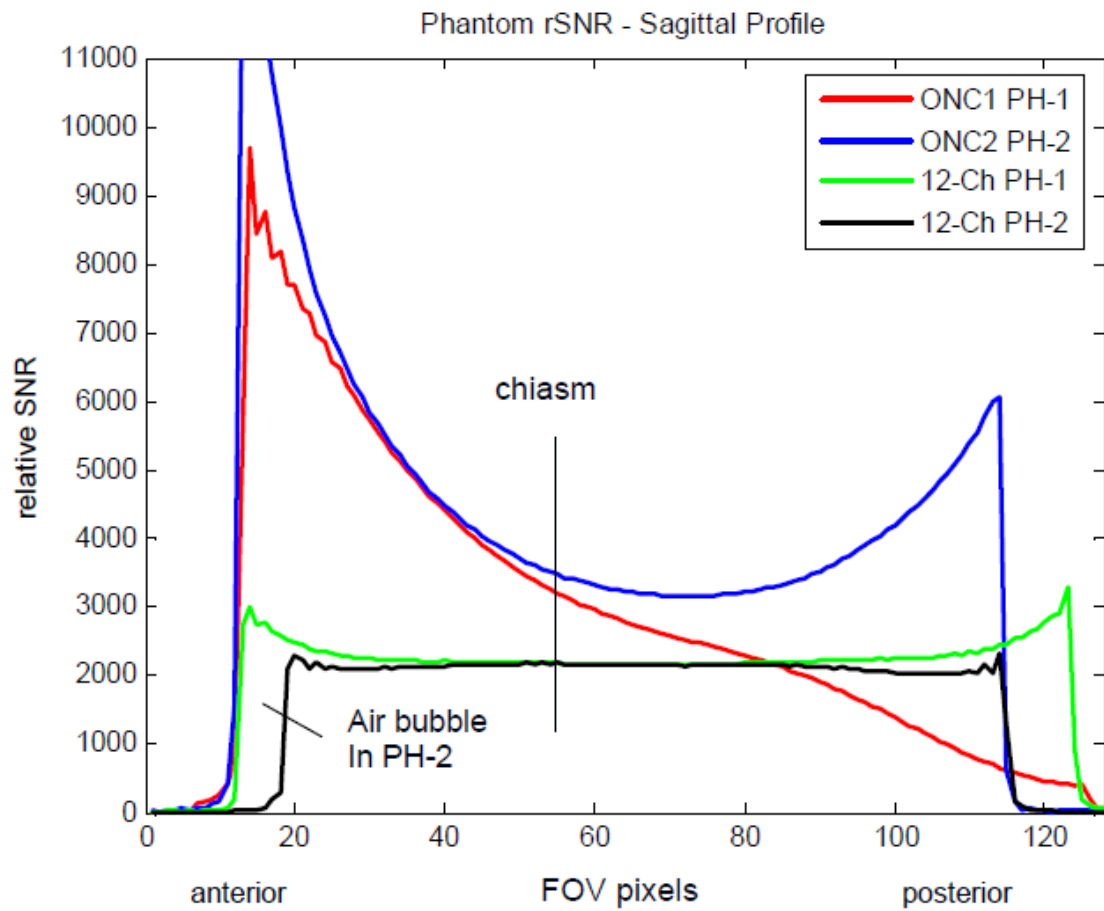


FIG. 4.7: Sagittal profile data plots of ONC1 (20-Ch, red) and ONC2 (28-Ch, blue) with respective phantoms, and the phantom baseline plots with the Siemens 12-channel coil (green, black). The approximate front-to-back location of the optic chiasm is labeled.

TABLE 4.1: ONC2 axial data showing the relative position of each region of interest.

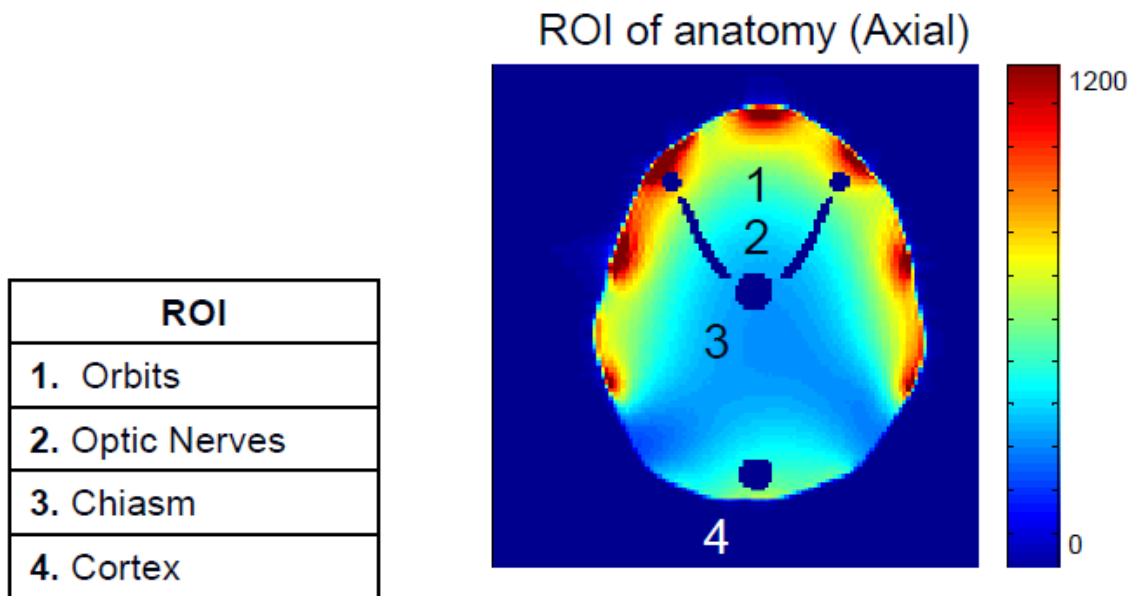


TABLE 4.2: Sagittal rSNR image data with corresponding rSNR increase over the Siemens 12-channel coil. ONC1 (20-channels) has all channels active, while ONC2 (28-channels) is shown in two different configurations: (*All* channels active and *19* channels active). Relative scale: 0 (dark blue) to 12000 (deep red).

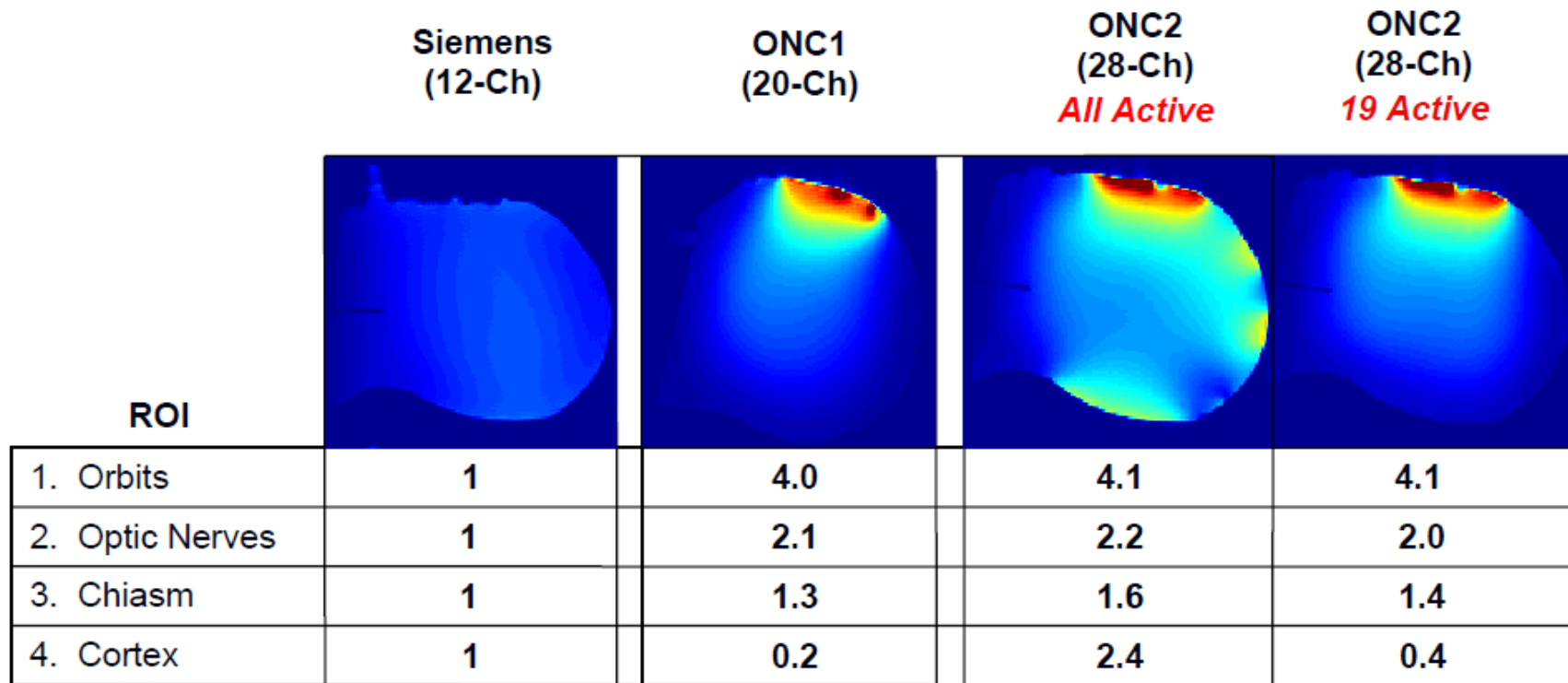


Table 4.2 compares the rSNR performance of ONC1 and ONC2 relative to the Siemens 12-channel coil. In the case of ONC1 and the Siemens coil, the data was obtained from each coil with all the respective coil elements active; i.e. the signal data obtained from all 20 or 12 elements, respectively, was included in the rSNR calculation.

Two different coil configurations are shown for ONC2 in Table 4.2. For the data labeled “All Active,” the signal contribution of all 28 channels of ONC2 was included. The data labeled “19 Active,” on the other hand, excludes signal data from the headrest coils and seven additional coils at the crown of the head. In this case, the rSNR data is the same data that was obtained by scanning with all channels active, but only the signal contribution from each desired coil channel is combined in software during image reconstruction. In the configuration with only 19 channels active, ONC2 has approximately the same coil coverage as ONC1, and the rSNR performance of ONC2 compared to ONC1 is very similar.

Studying ONC2 with a reduced number of active channels was of interest to determine the relative performance of individual coil elements. For example, coils along the sides of the head are in a different relative position to the primary magnetic field of the scanner compared to coils at the crown of the head, and thus contribute different rSNR magnitudes [30]. As can be observed, the direct rSNR contribution of the top-most coils to the optic nerve tract is not significant. However, these additional coils proved helpful when parallel imaging was investigated using ONC2.

ONC2 was also compared to the Siemens 12-channel coil as shown in Figures 4.8 and 4.9. Figure 4.8 was produced from a single volunteer scan, where the improved rSNR of ONC2 is immediately noticeable from the various imaging planes. Figure 4.9

rSNR Comparison of Coils



ONC2
(28-ch)



Siemens
(12-ch)

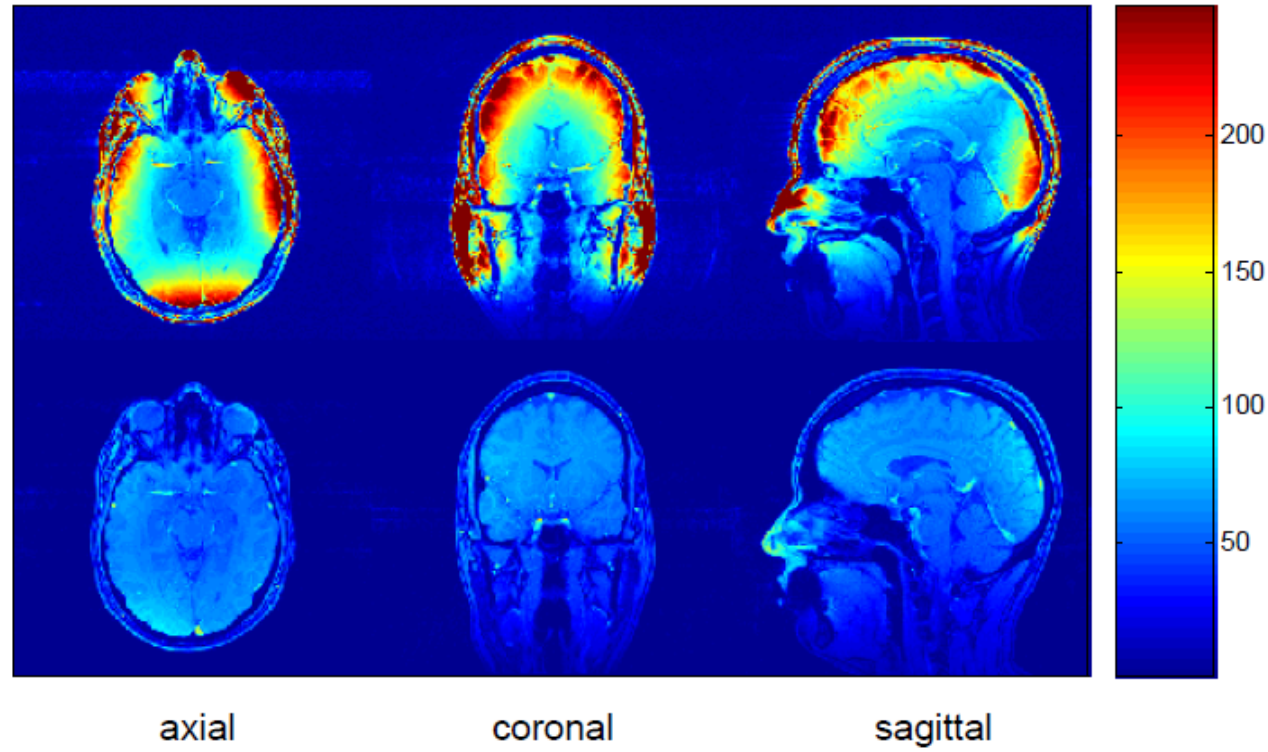


FIG. 4.8: Relative SNR comparison of ONC2 (top) and the Siemens coil (bottom).

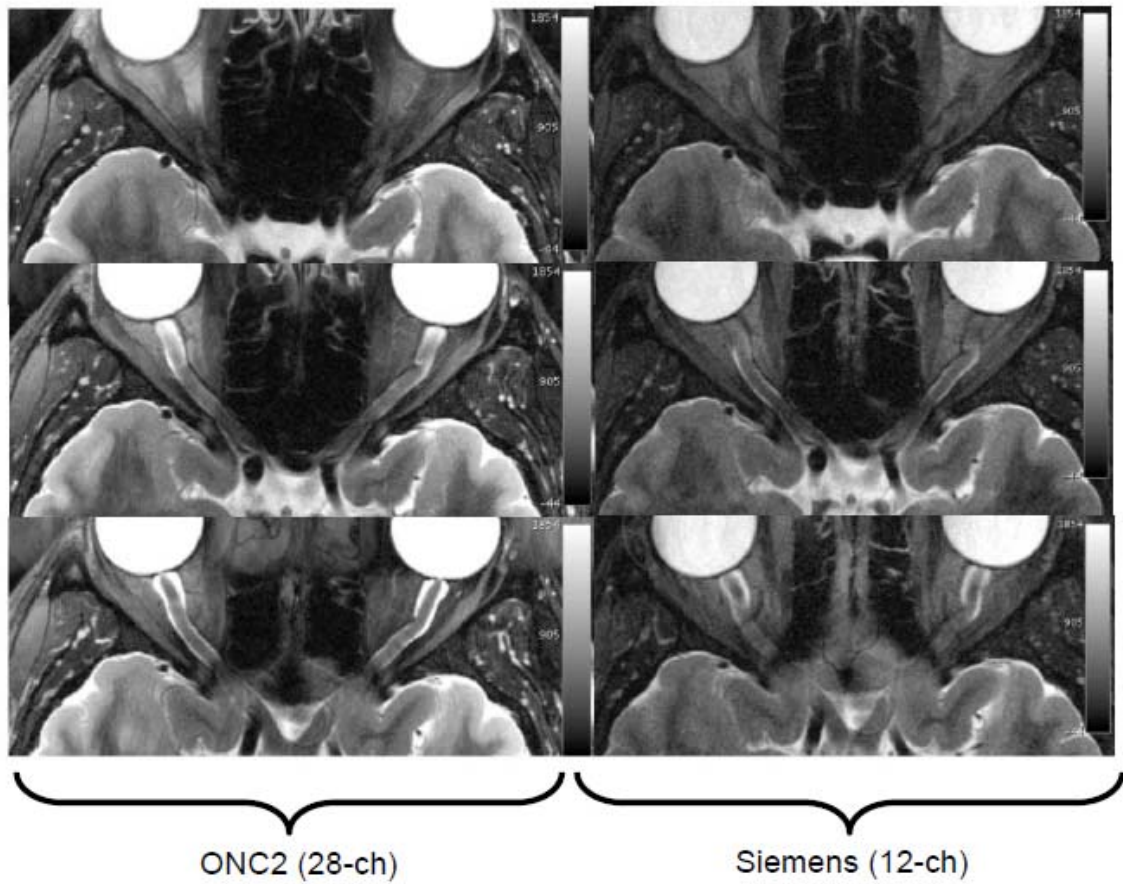


FIG. 4.9: Clinical image comparison of sequential slices through the optic nerve region, showing the increased image clarity of ONC2 (left column).

compares the image clarity of optic nerve anatomical scans acquired from a similar volunteer. Again, the increased rSNR of ONC2 provides greatly improved clarity along the optic nerves and in the surrounding regions.

4.1.2 Parallel Imaging Comparison

Figure 4.10 shows a comparison of parallel imaging performance for ONC1 and ONC2. The imaging speed factors (x2, x3, 2x2, 2x3, etc.) have reference to the lines of k-space that were skipped during imaging time, and filled in during postprocessing from known coil sensitivities. The colored 1/G-factor maps illustrate that ONC2 performs well over the region of the optic nerve, where values near 1 (red) indicate better parallel imaging performance. As imaging speed was increased, ONC2 exhibited a much lower amount of image decomposition from aliasing compared to ONC1. The improvement is primarily due to the additional nine coils and full head coverage design of ONC2.

4.2 Collapsible Design Comparison Studies

As stated before, many existing head coils are built using one-piece rigid cylindrical formers, to which phased arrays are attached. While these nonadjustable coils provide high SNR when imaging patients with medium- to large-sized heads, performing advanced imaging techniques of the optic nerve (ON) is problematic for patients with small-sized heads. Small heads tend to decrease the coil filling factor and increase the distance between the coil elements and sample (distance ' d ', Fig. 4.11), resulting in a loss of SNR in the region from the orbits to the chiasm. The following studies present imaging data of phantoms and human volunteers within ONC2 and the commercially

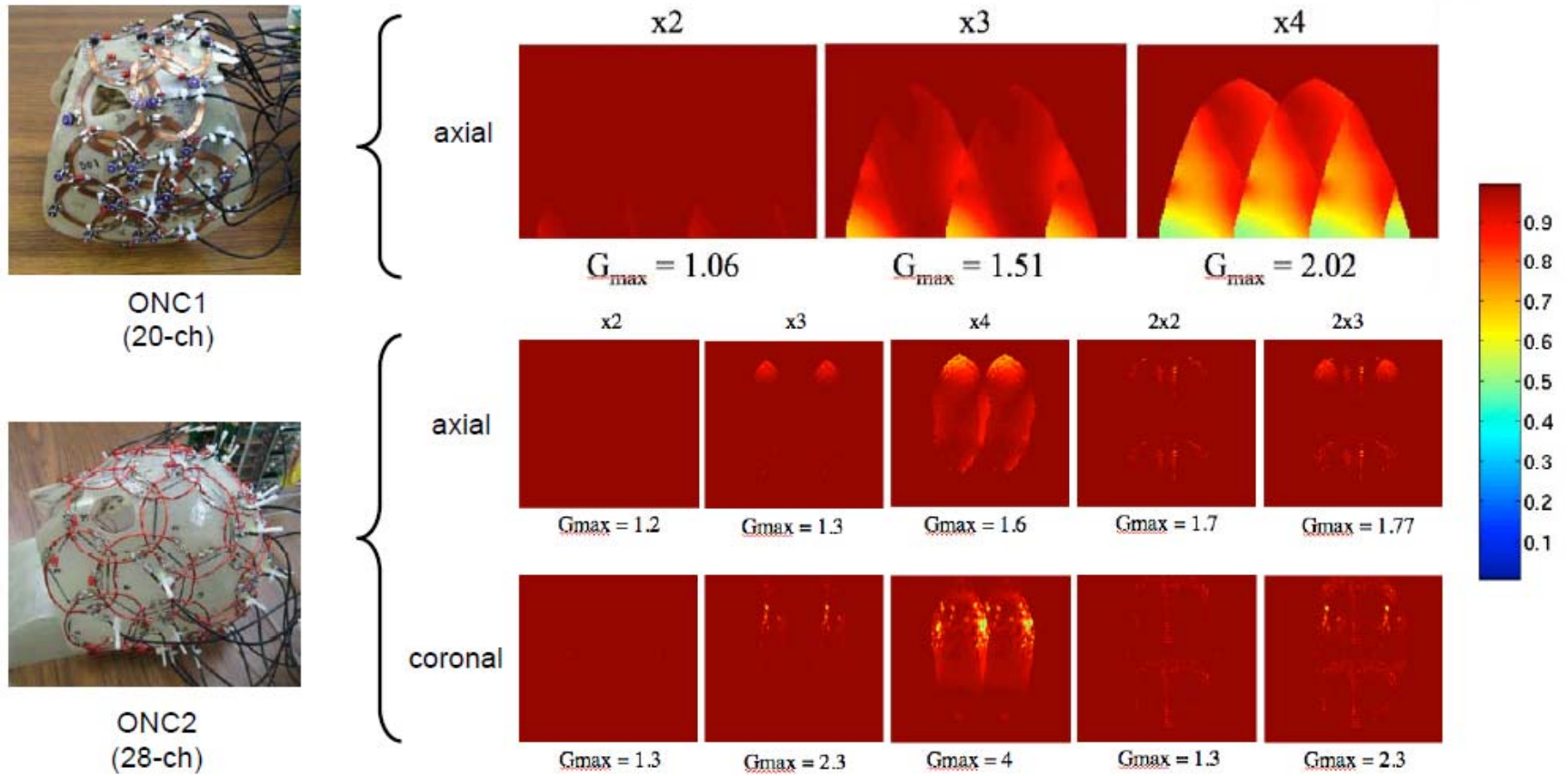


FIG. 4.10: $1/G$ factor maps of ONC1 (top row) and ONC2 (bottom two rows), with reduction factor (x2, x3, etc.) and maximum G -factor (G_{\max}) indicated.

available Siemens 12-channel rigid head coil. The results are compared to quantitatively determine the relative SNR benefit of the collapsible helmet construction of ONC2.

4.2.1 – rSNR Comparison of Former Design

A cylindrical NiCl₂ phantom (8 inches in diameter) was imaged in the rigid Siemens 12-channel head coil at various vertical positions within the coil ($d_{\text{lower}} = 60\text{mm}$, $d_{\text{middle}} = 25\text{mm}$, $d_{\text{upper}} = 2\text{mm}$, Fig. 4.12). An rSNR difference of 62% was observed between the two extreme lower and upper positions using a region of interest (ROI) that approximated the position of the orbits within the head. A difference of 22% was observed between the lower and middle positions. Changing the coil-to-sample distance in this manner simulated the insertion of patients with various head sizes into the coil. The rSNR values of this study represent a considerable loss in spatial resolution that would be experienced when a small head is placed within a rigid coil. Since many modern imaging techniques cannot afford the loss of rSNR resulting from a low filling factor, the need is evident for a coil with a collapsible feature that maintains consistent rSNR for any head size.

The reposition study of Figure 4.12 was repeated using a normal volunteer instead of a phantom. The volunteer was imaged in ONC2 and the Siemens coil during one scanning session to legitimize the comparison of relative SNR. For both ONC2 and the Siemens coil, the volunteer was placed in two different locations within the coil as shown in Figure 4.13 and Table 4.3. Distances d_{lower} and d_{upper} were measured from the top dead center of the coil to the forehead of the volunteer at the point between the eyebrows.

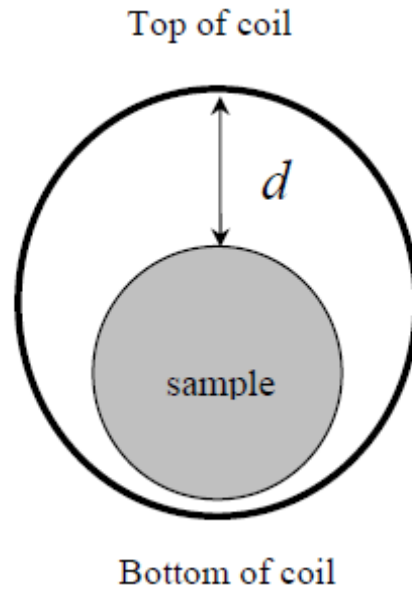


FIG. 4.11: Axial view of a sample within a rigid, cylindrical head coil (with distance ' d ' from coil elements to sample 'face' defined).



FIG. 4.12: Relative SNR plot of an axial slice through a cylindrical phantom placed in various locations within the Siemens 12-channel coil ($d_{\text{lower}} = 60\text{mm}$, $d_{\text{middle}} = 25\text{mm}$, $d_{\text{upper}} = 2\text{mm}$).

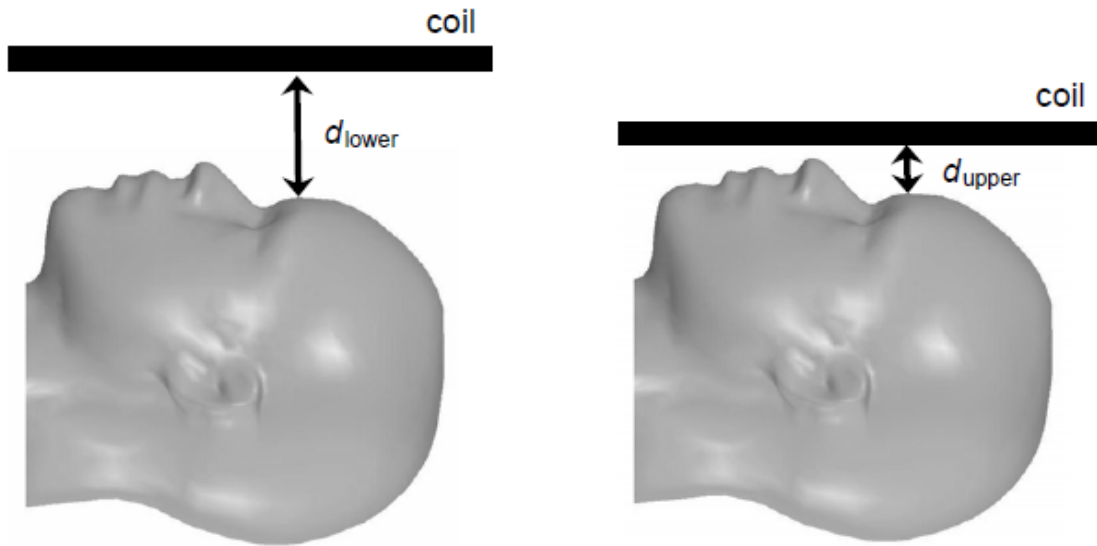


FIG. 4.13: Coil-to-sample distance (d) measurements for the two head positions studied within ONC2 and the Siemens coil.

TABLE 4.3: Table of measurements for d_{lower} and d_{upper} .

Coil	d_{lower}	d_{upper}
ONC2	2 cm	0 cm
Siemens	5 cm	1 cm

For the d_{lower} scan of ONC2, padding was placed between the coil and the volunteer's forehead in order to lift the mask former away from the face. This lower position within ONC2 simulated the spacing of the mask coils away from the patient as if the formers *weren't* collapsible. Likewise, for the d_{upper} scan of the Siemens coil, padding was placed beneath the volunteer's head to elevate it within the coil in order to simulate a collapsible design. The data from this volunteer study are shown in Figures 4.14 and 4.15. ONC2 exhibited an rSNR improvement of 28% at the orbits when the volunteer was placed in the upper vs. lower positions within the coil. Similarly, the Siemens coil exhibited an rSNR improvement of 32% between these two volunteer positions. This study demonstrates that the collapsible feature of ONC2 is a key improvement in head coil design, since such large rSNR improvements confirm the advantage of using coils in close proximity to the desired anatomy.

4.2.2 Multiple Head-Size Study

A proof of concept study was designed and performed to further test the rSNR advantages of the collapsible design of ONC2. Three volunteers were recruited for the study following IRB standard guidelines. Volunteer selection was based on head size, which was quantified using head circumference or 'hat size' as shown in Figure 4.16 and Table 4.4. All volunteers were scanned one after another within a four-hour time period using both ONC2 and the Siemens coil. The results of this study are shown in Figures 4.17 and 4.18. The same approximate regions of interest of Table 4.1 were used, only drawn individually to match the anatomy of each image.

rSNR Comparison of Head Positions



ONC2
(28-ch)



Siemens
(12-ch)

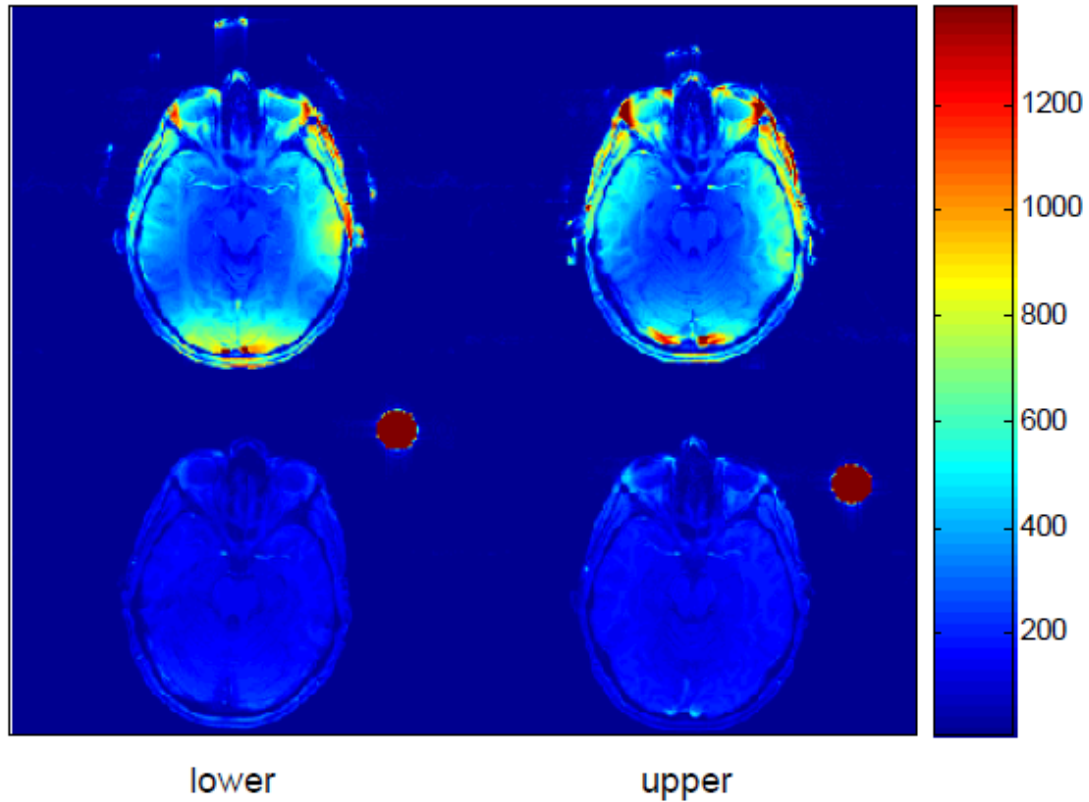


FIG. 4.14: Relative axial SNR data from one normal volunteer placed in various positions within ONC2 (top row) and the Siemens coil (bottom row). The large dot is a small reference phantom to show relative head position within the Siemens coil. Silicone was used to secure components on ONC2; silicone signal can be seen in the top row, showing the relative upper and lower positions of the mask former.

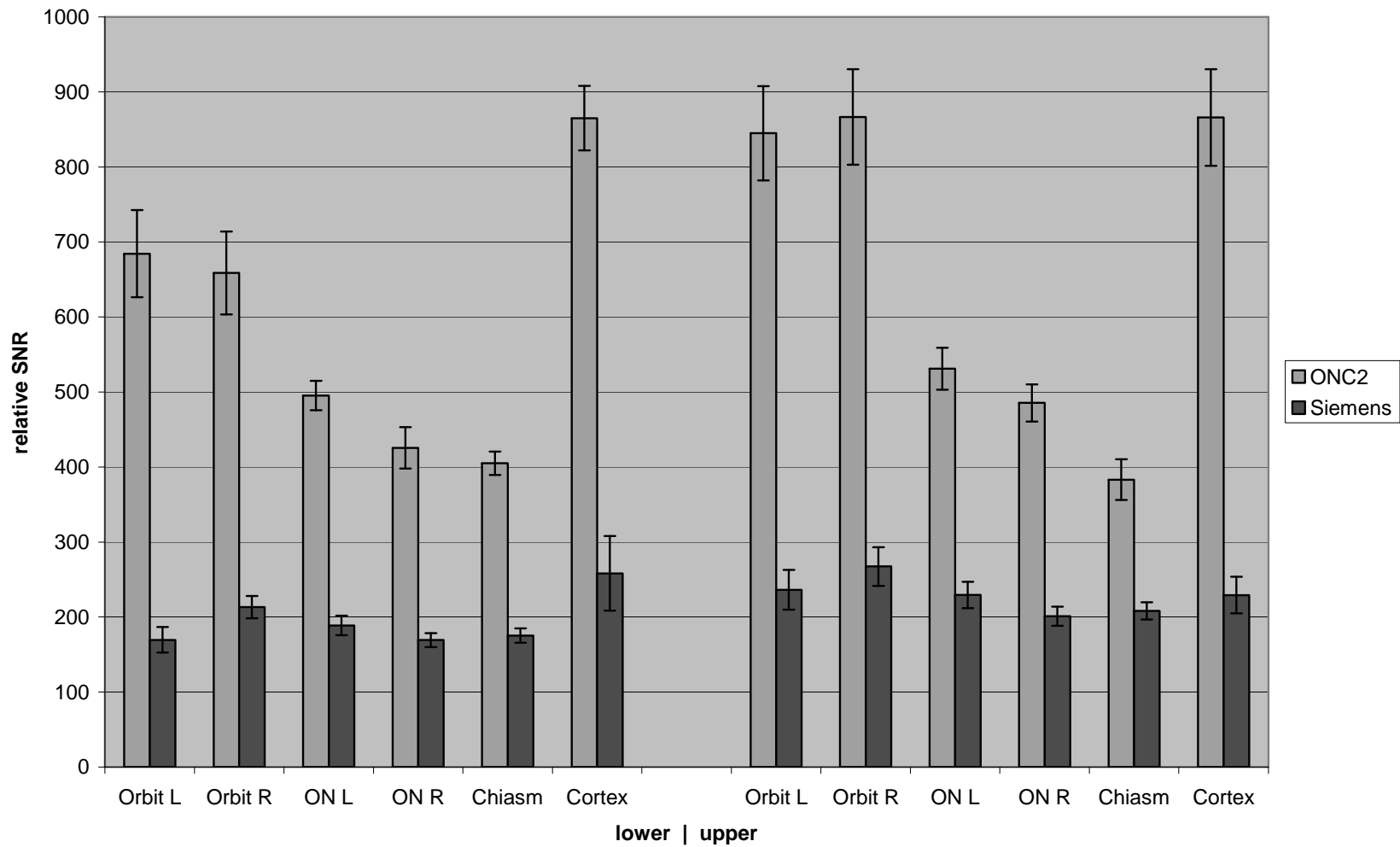


FIG. 4.15: Mean rSNR data at each region of interest of one volunteer imaged in ONC2 and the Siemens coil. The *lower* position is the normal imaging position for the Siemens coil, while the *upper* position is normal for ONC2.

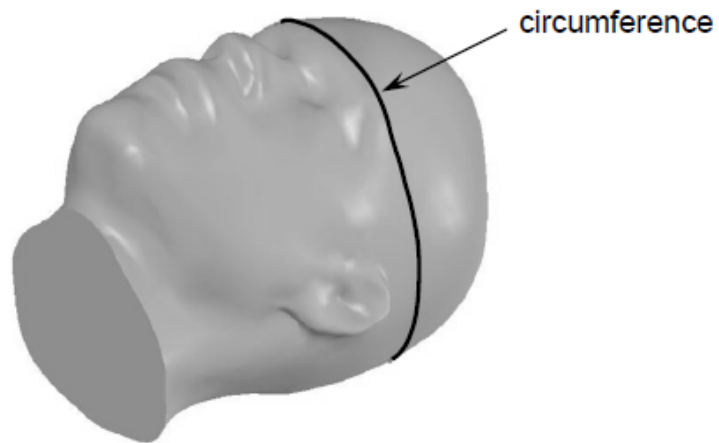


FIG. 4.16: Head circumference, or ‘hat size’, was used to quantify the head size of the three volunteers.

TABLE 4.4: Table of volunteer head sizes.

Head Size	<i>Circumference</i>	<i>Distance ‘d’</i>
Small	53 cm	4.5 cm
Medium	56 cm	4.1 cm
Large	61 cm	2.9 cm

rSNR Comparison of Head



ONC2
(28-ch)



Siemens
(12-ch)

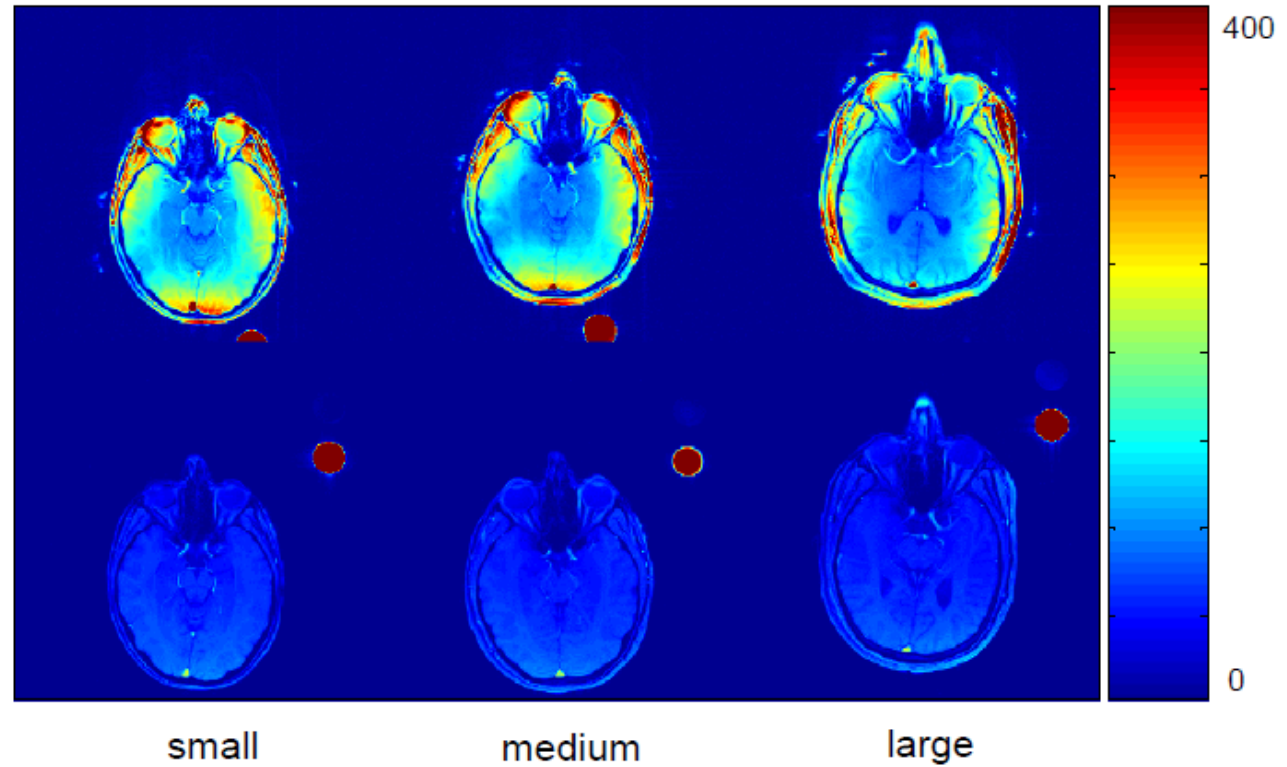


FIG. 4.17: Relative SNR plot of a three normal volunteers within ONC2 (top row) and the Siemens coil (bottom row). ‘Hat size’ (or head circumference) was used to quantify head size (small = 53cm, medium = 56cm, and large = 61cm). The large dot is a small reference phantom to show relative head position. The reference phantom is not shown for the large head size in ONC2 because the field of view was shifted to include the entire head in the image.

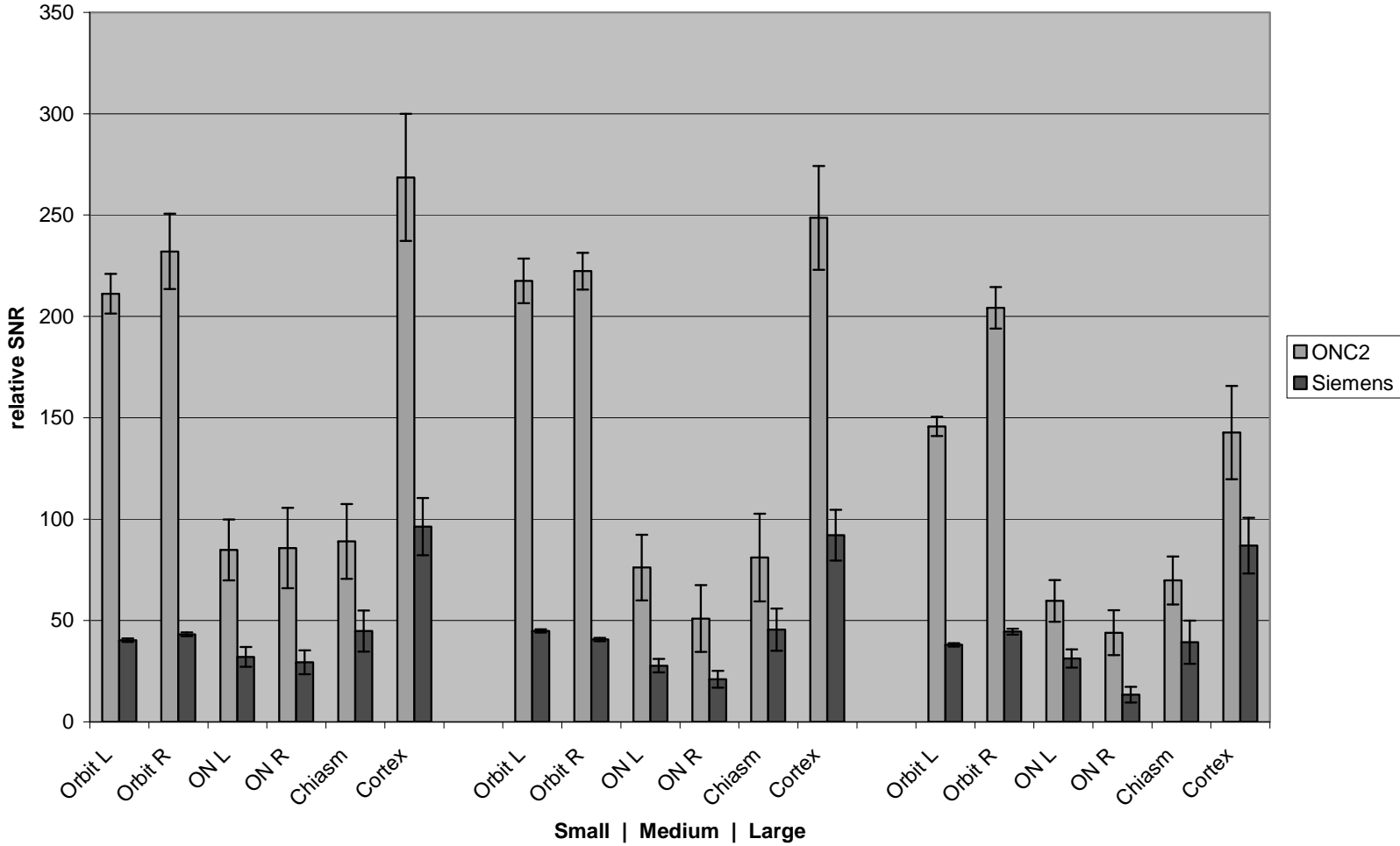


FIG. 4.18: Mean rSNR data at each region of interest for the various head sizes imaged in ONC2 and the Siemens coil. Although the data varies in consistency from head to head, ONC2 exhibits approximately twice the relative SNR along the entire optic pathway, and even up to 4x in the orbits.

From the data of Figure 4.18, ONC2 exhibits a general rSNR improvement trend on the order of two to five times the Siemens coil along the entire optic pathway. The rSNR differences from head to head are most likely due to the varying filling factor and coil loading effects (ultimately influencing the coil tune and match) typically encountered when scanning different subjects. Another possibility may be due to the ROI selection. For applications where homogeneous, entire brain images are desired, the Siemens coil is a suitable choice. However, for higher resolution, anatomy specific imaging of the optic pathway, ONC2 provides significantly higher rSNR and parallel imaging performance.

4.2.3 Patient Studies

When patients with known histories of optic neuritis were imaged using ONC2, abnormalities were discovered that corresponded well with particular symptoms (Fig. 4.19). Clinicians have expressed excitement that ONC2 has achieved sufficient resolution to detect diagnosable features. For clinical scans, a 2D TSE acquisition with Fat Saturation and a $0.4 \times 0.4 \times 2 \text{ mm}^3$ voxel size (TR/TE = 4.5s/120ms) was used.

Additional studies were conducted with ONC1 and ONC2 which had previously not been considered due to the general lack of SNR in coil imaging. Diffusion Weighted (DW) imaging is a method for tracking fiber orientation of nerve and muscle tissue. In this procedure the molecular structure of specific tissues can be studied in addition to the T_1 and T_2 characteristics observed through conventional MRI [38]. DW imaging of the optic nerve is challenging because the nerve is small and freely mobile. However, the rapid and high-resolution capabilities of ONC1 and ONC2, due to their anatomy specific construction, proved advantageous for this modern imaging technique. A difference in

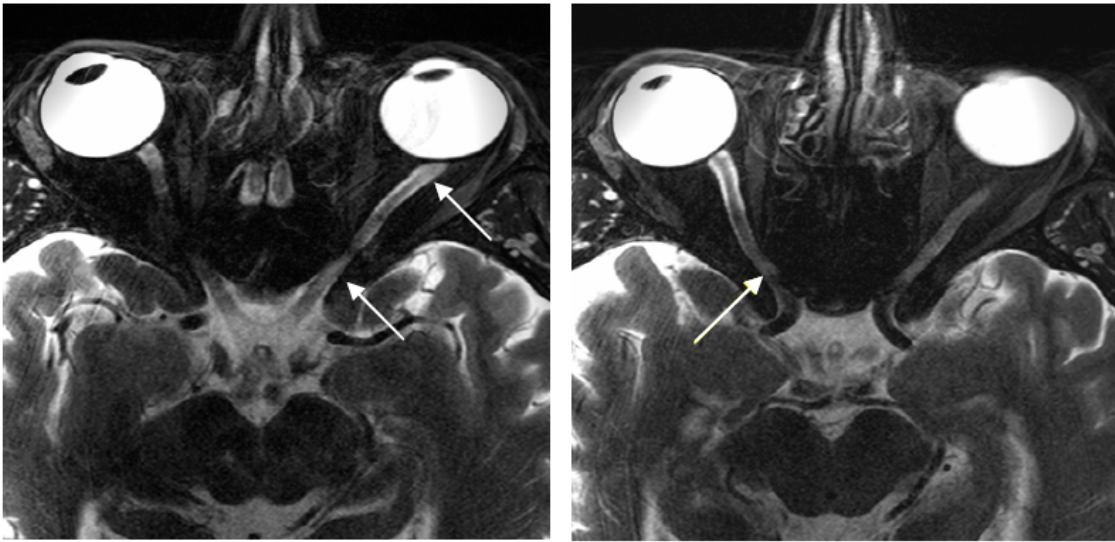


FIG. 4.19: *Patient A*: plaque on the left optic nerve (arrows in left image) and signal abnormality on the right optic nerve (single arrow in right image).

DW imaging performance was observed between the two coils in regards to the imaging depth: ONC1 outperformed ONC2 for shallower anatomy, while ONC2 surpassed ONC1 for deeper structures.

Diffusion Tensor Imaging (DTI) is an experimental scan procedure that may provide a qualitative measurement for evaluating optic neuritis [39]. As with DW imaging, high-resolution DTI shows detailed nerve and muscle fiber orientations through fiber tracking techniques, allowing a level of image analysis that is not always obtained through visual image inspection. DTI was performed on patient volunteers with 1 x 1 x 2 mm³ spatial resolution, 7 minute imaging time, 8 slices locations, b=0 and 500 s/mm² along 12 noncollinear diffusion encoding directions, and 12 magnitude averages at each direction. The results from this study have demonstrated that high resolution DTI can be performed in the optic nerve using ONC2, which provides high local rSNR.

CHAPTER 5

DISCUSSION

In Chapter 3: Coil Construction, it was mentioned that securing the individual coil elements to the fiberglass former was done by fastening solder pads to the former with epoxy. This method had a number of problems. Most significantly, the 14-gauge wire was sufficiently thick to prevent the conductor segments from bending easily when the coil former was flexed. Due to the rigid segments, the bending forces were focused at the solder joints of the tuning and matching capacitors (Fig. 5.1), causing them to break often. Additional wire gauges were included in the revised Q tests of Table 3.3 as potential alternatives. According to the sensitivity data, the wire gauge of ONC2 could be reduced to 16-gauge without a significant loss in sensitivity.

During coil placement, the stretchy mesh method of coil layout was discovered to have a serious disadvantage. Typical surface coil arrays such as ONC1 have loop elements of constant size, allowing similar component values (i.e. tune and match capacitance values) to be used for all elements. Thus, when the component values for the initial coil were determined, one could construct the remaining coils without further calculations. Unfortunately, the stretchy mesh layout method used to guide coil placement on ONC2 dramatically increased the coil construction time. Since each coil

was of dissimilar diameter, unique component values had to be determined for each individual coil.

A number of important observations can be drawn from Table 4.2. First, the large rSNR contribution made by the two headrest coils of ONC2 to the optic cortex region is immediately noticeable, an improvement of 6- to 12-times over the other coil designs. However, a similar improvement would probably be expected with ONC1 if it also included headrest coils. Second, the coils at the crown of the head of ONC2 do not seem to contribute significantly to the rSNR in the regions of interest along the optic pathway. This observation confirms the importance of coil placement relative to the primary magnetic field in regard to obtaining maximum rSNR [11]. It also prompts the question of whether the full head coil coverage feature of ONC2 is as beneficial as anticipated, while considering that constructing nine extra coil elements (and their respective amplification circuits) significantly complicates the design of the coil over the less complicated mask design of ONC1. In other words, the question is whether surrounding the entire head with coils produces a worthwhile performance improvement. The parallel imaging plots of Figure 4.12 show that the increased number of coils in ONC2 does indeed offer improved performance, if increased imaging speed is a desired feature of the finished coil.

ONC2 differs sufficiently enough from ONC1 that one particular design feature of ONC2 cannot be credited with the slight performance increase noted above. Section 6.3 – Future Work will provide additional detail about a number of spin-off studies designed to isolate and test the various new features of ONC2.

While the collapsible design of ONC2 offers improved rSNR at the orbits and chiasm, significant imaging gaps (Fig. 5.2) can be observed in the regions surrounding the joint between the upper and lower formers (Fig. 3.7) where there is a gap in the coil overlap pattern. For optic nerve imaging, high rSNR at the orbits and chiasm was of higher priority than uniform full head imaging. Thus, the regions of lower rSNR at the back of the head were not considered injurious to the primary function of the coil.

Despite the rSNR improvement of the collapsible former design, such a tight-fitting fiberglass helmet could be less comfortable than roomy, rigid coils for patients with tendencies toward claustrophobia. As an alternative, achieving a small coil-to-sample distance in rigid coils may be possible by adding more padding to the bottom of the coil, forcing the face up near the top elements.

High rSNR imaging of the optic nerve has typically been limited by the large distances between the coil elements and the orbits of the patient. Modern imaging techniques cannot afford the loss of SNR resulting from such a low filling factor. For ONC2, however, the coil-to-orbit distance remained consistently at $d = 0$ cm, thus maintaining a high filling factor for the variety of differently-sized heads that have been imaged.

This project involved many considerations not directly related to Electrical Engineering, such as patient comfort and positioning in the MRI scanner. Such issues were very important to the functionality of the coil and the success of the final product in a clinical environment. Patient comfort was of primary concern, since image quality depends highly upon the patient remaining absolutely still and relaxed during an MRI scan. The coil was required to withstand repeated deflection as it was placed over and

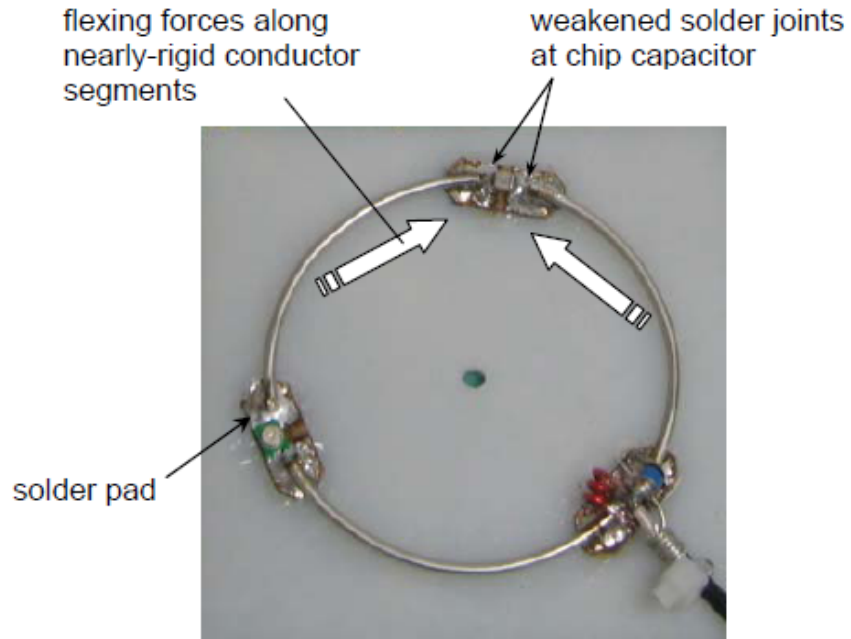


FIG. 5.1: Typical coil element failure occurs at solder joints between chip capacitor and coil conductor segments.

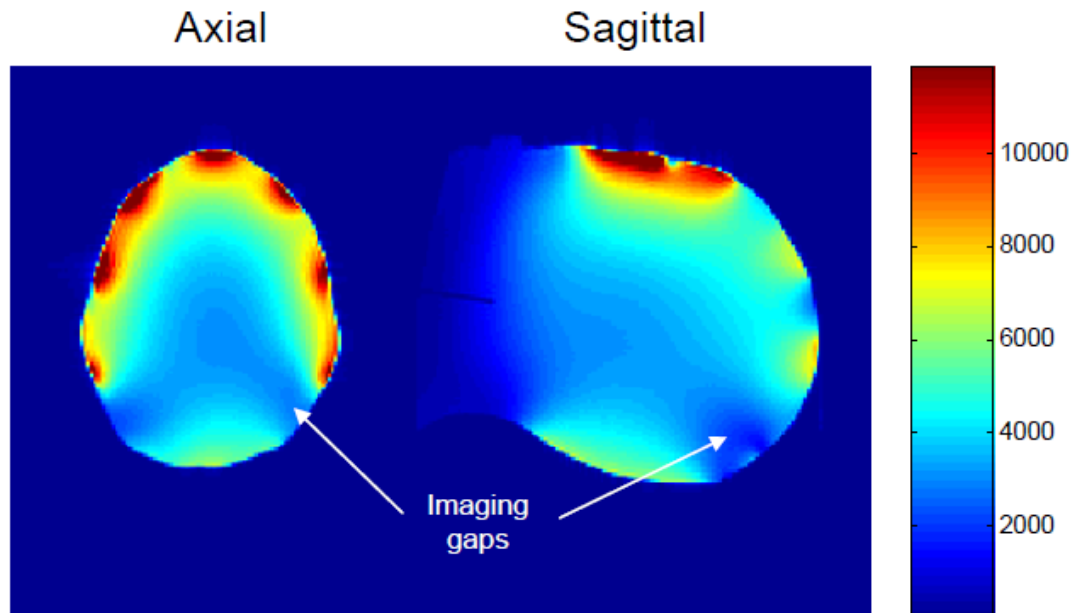


FIG. 5.2: Imaging gaps are observed where the two halves of the ONC2 former separate, and coils are not present.

removed from the head of a patient. Additionally, the coil and the associated amplification electronics also were to withstand repeated installation and removal from the MRI table. In short, while this project is primarily a study of electromagnetics, the application of many additional knowledge disciplines was required.

CHAPTER 6

SUMMARY, CONCLUSIONS, AND FUTURE WORK

6.1 Summary

This thesis describes the design, construction, and testing procedures of a twenty-eight-channel phased-array head coil for improved optic nerve imaging. As an introduction, an in-depth MRI background chapter is included to help the reader understand the design and engineering decisions involved in developing the coil. Many preliminary research studies were performed and supplementary coil development tools fabricated to better optimize the coil and facilitate the coil assembly process. The coil itself was constructed with two fiberglass former halves that fit together in a collapsible design, with 26 coils placed on the mask former and two in the headrest former. Thirty-two channels were available on the Siemens 3T TIM Trio scanner used in this study, but only 28 channels were utilized due to the lack of availability of the required four-channel plug, and the lack of space for the additional electronics in the preamplifier housing box.

Data from phantom and human imaging studies demonstrates that the collapsible design and full head coverage layout of the constructed coil are key improvements in head coil design when performing studies involving the optic pathway. The new coil provides 400% greater rSNR in the orbits, over 200% along the length of the optic nerve, and 55% at the chiasm, when compared to similar commercial head coils. With the

unique collapsible design of the new coil, these improvements can be maintained for a variety of patients with different head sizes. Numerous (15+) volunteer and clinical studies suggest that the optic nerve can be visualized using 3T MRI with advanced imaging coils, providing improved care for optic neuritis patients.

6.2 Significance

In general, the SNR advances of MRI technology have typically focused on increasing the strength of the primary magnetic field of the MRI scanner. This focus has merit, since the proportional rSNR improvement with increased field strength is nearly linear [40]. However, upgrading the field strength is prohibitively expensive, both in monetary cost and lost revenue from down time during the scanner upgrade. Such costs have been a significant factor retarding the widespread use of advanced MRI technology. As an alternative, the development and general application of anatomy-specific coils offers a promising economic solution. Study results from this thesis, and nearly every literature reference describing the construction of an anatomy-specific coil, report significant improvements in imaging performance. Such improvements come with a noteworthy price tag reduction from \$3-5 million for a new scanner to perhaps \$20,000-80,000 for a new coil. The use of RF coils in magnetic resonance imaging can offer a number of advantages to both doctor and patient. Anatomy-specific coils allow the anatomical regions of interest to be targeted, supply significant improvement in rSNR, and provide a cost efficient solution to implement modern imaging techniques and provide improved patient care.

The anatomy-specific coil described in this thesis has improved MR imaging of the optic nerve. Significant SNR gains not attainable with commercial coils were achieved from the implementation of three design features: a collapsible design for different head sizes, coil loops encompassing the entire head, and wire loop construction. While an increase in SNR is not a universal indicator of improved patient care, it offers a quantifiable metric for assessing coil performance. Providing a prolonged and comfortable life to a patient is the ultimate measure of success for any medical technology.

6.3 Future Work

The construction process of ONC2 stimulated thought into a number of spin-off studies that could be performed to isolate and measure the design improvements of ONC2. It has been hypothesized that coils built using copper foil conductors suffer from possible magnetic flux limitation effects [12]. Wire conductors, it is believed, allow a greater amount of magnetic flux through each loop element, and also reduce the capacitive coupling between overlapped loops. A number of studies could target the particular influence of wire vs. foil construction on imaging performance. One such study would involve constructing overlapped coil clusters on a flat substrate, with the coils of each cluster made of a different conductor material. The Q and rSNR of each cluster could then be measured and studied. As a second study, two additional helmet coils could be constructed to test the difference between copper wire and copper foil elements in a more realistic overlapped configuration, i.e., when the elements are placed on an actual coil former. The only difference between the two coils would be the coil

conductor material; all other parameters would be held constant, including the coil element size, placement pattern, number of distributed capacitors, and the fiberglass former design. Phantoms and human volunteers could be imaged within these coils to form a more accurate judgment of the advantages of copper wire vs. copper foil.

The current trend in coil design is to surround a given imaging volume with an ever greater number of coils [12]. This trend, in addition to the gradual increase of primary field strength, contributes new challenges to the study of coil design. Not only are the radiation losses increased and the coil field homogeneity reduced, but the coils themselves must be physically smaller and more intricate in design. Despite the increased construction costs, if an MRI scanner system with more receive channels were made available, increasing the number of coil elements beyond thirty-two may be an attractive option for increased rSNR.

Additional future work for ONC2 includes further assessment of the coil in a clinical setting. More patient studies, particularly involving advanced imaging techniques such as DTI, could broaden the imaging ‘toolbox’ available to radiologists for characterizing disease. All in all, the development of ONC2 has provided a springboard to promote interest, opportunities, and funding for future optic nerve research.

APPENDIX A

MUTUAL INDUCTANCE

This appendix contains the Matlab code for the mutual inductance plot of Figure 2.47.

```
%%%%%%%%%%%%%%%%%%%%%%%%%%%%%%%%%%%%%%%%%%%%%%%%%%%%%%%%%%%%%%%%%%%%%%%%%%
%   Robb Merrill, Dec 09
%   Roemer.m - This program reproduces the mutual inductance plot of
%               two overlapped loops (Fig. 2.50), as described in
%               The NMR Phased Array by Roemer [32].
%
%   Supporting functions:  self_calc.m,
%                           induct_calc.m,
%                           vector_distance.m,
%                           loop_calc.m,
%                           make_diagram2.m
%%%%%%%%%%%%%%%%%%%%%%%%%%%%%%%%%%%%%%%%%%%%%%%%%%%%%%%%%%%%%%%%%%%%%%%%%%
clear all;
close all;

%% mag. permeability in vacuum, in units of mm
u0 = 4*pi*10^(-7) * 1000;

%   space volume dimensions:      Units : mm
xsize = 200;                      % 20 cm
ysize = 100;                       % 10 cm
zsize = 100;                       % 10 cm

xy_plane = zeros(xsize,ysize);
a = 25;                             % half of loop x dimension = 2.5cm
b = 25;                             % half of loop y dimension = 2.5cm

%%%%%%%%%%%%%%%%%%%%%%%%%%%%%%%%%%%%%%%%%%%%%%%%%%%%%%%%%%%%%%%%%%%%%%%%%% Self Inductance
induct_11 = self_calc(xy_plane,a,b);
induct_22 = induct_11;

%%%%%%%%%%%%%%%%%%%%%%%%%%%%%%%%%%%%%%%%%%%%%%%%%%%%%%%%%%%%%%%%%%%%%%%%%% Mutual Inductance
separation_amt = 0:80;

total_induct = [];
diagram_cell = cell(1,length(separation_amt));
```

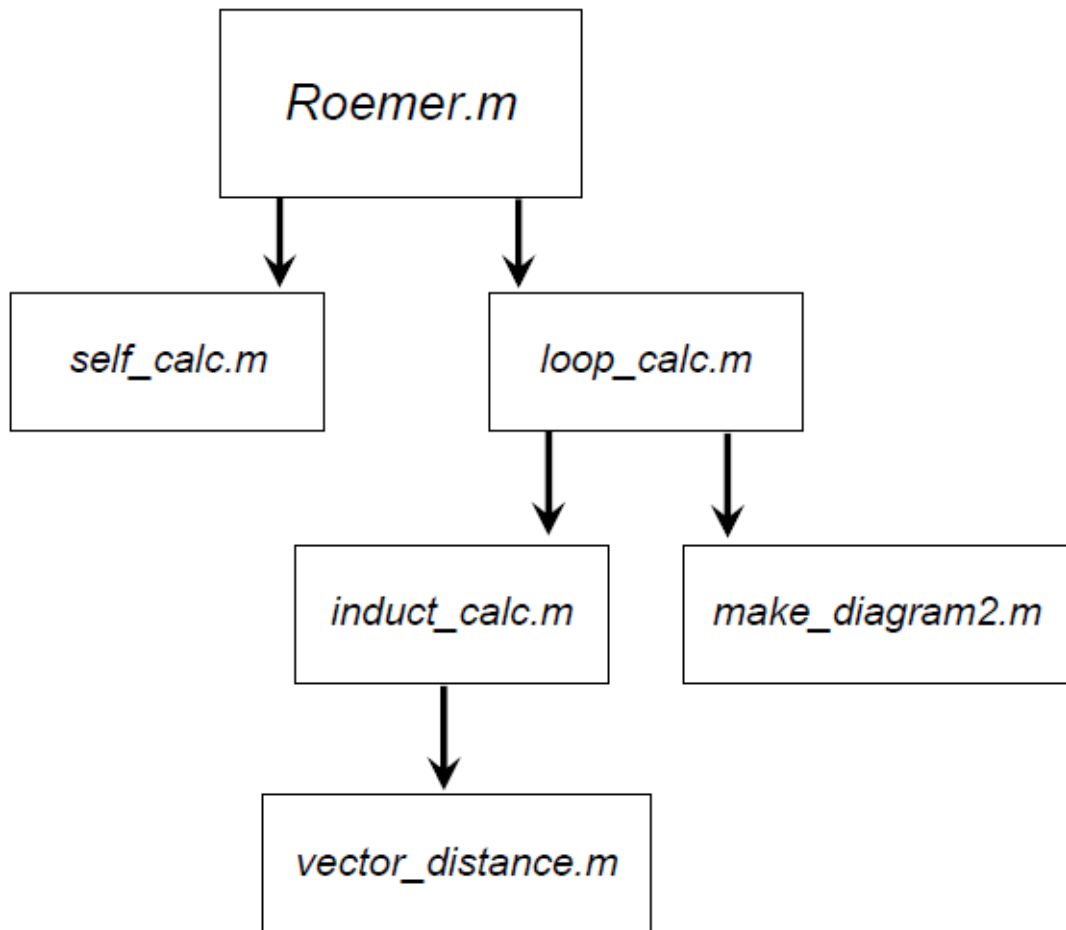


FIG. A.1: Program flow chart


```

for index = 1:length(separation_amt)
    separation = separation_amt(index);

    loop1_shift = floor(separation/2);      % Move right
    loop2_shift = -ceil(separation/2);     % Move left

    [diagram1,diagram2,new_induct] = ...
        loop_calc(xy_plane,a,b,loop1_shift,loop2_shift);
    total_induct = cat(2,total_induct,new_induct);

    full_diagram = diagram1 + diagram2;
    diagram_cell(1,index) = {full_diagram};

end

% Roemer equation
total_induct = u0/(4*pi).* total_induct;
% divide by self-inductance
total_induct = total_induct ./ sqrt(induct_11 * induct_22);
% normalize to max = 1
total_induct = total_induct ./ max(total_induct);
% x_axis units = separation amt / loop size
separation_index = separation_amt ./ (2*a);

figure(4);
hold on;
line1 = plot(separation_index,total_induct,'b');
line2 = plot(separation_index,0,'r--');
axis image; axis([0 1.6 -.25 1]);
%title('');
xlabel('Ratio of: Overlap separation distance / coil width');
ylabel('Magnetic Coupling Coefficient');
hold off;

% The following two lines find the loop overlap point of zero
% mutual inductance
total_induct_abs = abs(total_induct);
[min_value,min_index] = min(total_induct_abs);

% The following stuff plots the overlapped loops in black and
% the background in white. Also, it makes the axes labels
% read positive/negative from the center point of overlap
plot_cell = rot90(diagram_cell{1,min_index});
plot_cell = 1./(plot_cell + .01);
[rowsize,colsize] = size(plot_cell);
rowmiddle = rowsize/2;
colmiddle = colsize/2;
overlap_row_index = -rowmiddle:1:rowmiddle-1;
overlap_col_index = -colmiddle+2:1:colmiddle-1+2;

figure(5);
imagesc(overlap_col_index,overlap_row_index,plot_cell);
axis equal;
axis([-colmiddle+35 colmiddle-1-34 -rowmiddle+10 rowmiddle-1-9]);
colormap(bone);

```

```

%%%%%%%%%%%%%%%%%%%%%%%%%%%%%%%%%%%%%%%%%%%%%%%%%%%%%%%%%%%%%%%%%%%%%%%%
%   Robb Merrill, Dec 09
%   self_calc.m -
%       (1) Changes from array (corner) indexing to distance-from-
%           center indexing
%       (2) For every point on the loop, calculates the mutual
%           inductance with every other point on the loop
%%%%%%%%%%%%%%%%%%%%%%%%%%%%%%%%%%%%%%%%%%%%%%%%%%%%%%%%%%%%%%%%%%%%%%%%

function total_induct = self_calc(plane,a,b)

total_induct = 0;
loop1_shift = 0;
loop2_shift = 0;
offset_shift = 0;

[rowsize,colsize] = size(plane);
rowmiddle = rowsize/2;
colmiddle = colsize/2;

%%%%%%%%%%%%%%%%%%%%%%%%%%%%%%%%%%%%%%%%%%%%%%%%%%%%%%%%%%%%%%%%%%%%%%%% rail 1 (left, 2a long)
dcol = colmiddle - b;
rail = 1;
for drow = (rowmiddle - a + loop1_shift):(rowmiddle + a + loop1_shift)
    total_induct = total_induct + ...
        induct_calc(plane,rail,drow,dcol,a,b,loop2_shift, offset_shift);
end

%%%%%%%%%%%%%%%%%%%%%%%%%%%%%%%%%%%%%%%%%%%%%%%%%%%%%%%%%%%%%%%%%%%%%%%% rail 2 (bottom, 2b long)
drow = rowmiddle + a + loop1_shift;
rail = 2;
for dcol = (colmiddle - b + 1):(colmiddle + b - 1)
    total_induct = total_induct + ...
        induct_calc(plane,rail,drow,dcol,a,b,loop2_shift, offset_shift);
end

%%%%%%%%%%%%%%%%%%%%%%%%%%%%%%%%%%%%%%%%%%%%%%%%%%%%%%%%%%%%%%%%%%%%%%%% rail 3 (right, 2a long)
dcol = colmiddle + b;
rail = 3;
for drow = (rowmiddle - a + loop1_shift):(rowmiddle + a + loop1_shift)
    total_induct = total_induct + ...
        induct_calc(plane,rail,drow,dcol,a,b,loop2_shift, offset_shift);
end

%%%%%%%%%%%%%%%%%%%%%%%%%%%%%%%%%%%%%%%%%%%%%%%%%%%%%%%%%%%%%%%%%%%%%%%% rail 4 (top, 2b long)
drow = rowmiddle - a + loop1_shift;
rail = 4;
for dcol = (colmiddle - b + 1):(colmiddle + b - 1)
    total_induct = total_induct + ...
        induct_calc(plane,rail,drow,dcol,a,b,loop2_shift, offset_shift);
end

```

```

%%%%%%%%%%%%%%%%%%%%%%%%%%%%%%%%%%%%%%%%%%%%%%%%%%%%%%%%%%%%%%%%%%%%%%%%
%   Robb Merrill, Dec 09
%   induct_calc.m -
%       (1) Changes from array (corner) indexing to distance-from-
%           center indexing
%       (2) Calls 'vector_distance.m' to calculate the distance
%           magnitude between a point on loop1 and a point on
%           loop2, and to obtain the dot product of the distance
%           vector
%       (3) For every point on loop1, calculates the mutual inductance
%           with each point on loop2
%%%%%%%%%%%%%%%%%%%%%%%%%%%%%%%%%%%%%%%%%%%%%%%%%%%%%%%%%%%%%%%%%%%%%%%%

function total_induct = ...
    induct_calc(plane,rail1,row_point1,col_point1,a,b,shift,offset_shift)

total_induct = 0;

[rowsize,colsize] = size(plane);
rowmiddle = rowsize/2;
colmiddle = colsize/2;

%%%%%%%%%%%%%%%%%%%%%%%%%%%%%%%%%%%%%%%%%%%%%%%%%%%%%%%%%%%%%%%%%%%%%%%% rail 1 (left, 2a long)
dcol = colmiddle - b + offset_shift;
rail2 = 1;
for drow = (rowmiddle - a + shift):(rowmiddle + a + shift)
    [dot_prod, dist_mag] = ...
        vector_distance(rail1,row_point1,col_point1, rail2,drow,dcol);
    if dist_mag ~= 0
        % The following equation is from Roemer's paper: [Eqn. 38].
        % The coefficients are multiplied into the entire array in
        % double_loop.m
        total_induct = total_induct + (dot_prod/dist_mag);
    end
end

%%%%%%%%%%%%%%%%%%%%%%%%%%%%%%%%%%%%%%%%%%%%%%%%%%%%%%%%%%%%%%%%%%%%%%%% rail 2 (bottom, 2b long)
drow = rowmiddle + a + shift;
rail2 = 2;
for dcol = ...
    (colmiddle - b+1 + offset_shift):(colmiddle + b-1 + offset_shift)
    [dot_prod, dist_mag] = ...
        vector_distance(rail1,row_point1,col_point1, rail2,drow,dcol);
    if dist_mag ~= 0
        total_induct = total_induct + (dot_prod/dist_mag);
    end
end

%%%%%%%%%%%%%%%%%%%%%%%%%%%%%%%%%%%%%%%%%%%%%%%%%%%%%%%%%%%%%%%%%%%%%%%% rail 3 (right, 2a long)
dcol = colmiddle + b + offset_shift;
rail2 = 3;
for drow = (rowmiddle - a + shift):(rowmiddle + a + shift)
    [dot_prod, dist_mag] = ...
        vector_distance(rail1,row_point1,col_point1, rail2,drow,dcol);
    if dist_mag ~= 0
        total_induct = total_induct + (dot_prod/dist_mag);
    end
end

```

```
end
end

%%%%%%%%%%%%%%%%%%%%%%%%%%%%%%%%%%%%%%%%%%%%%%%%%%%%%%%%%%%%%%%%%%%%%%%% rail 4 (top, 2b long)
drow = rowmiddle - a + shift;
rail2 = 4;
for dcol = ...
    (colmiddle - b+1 + offset_shift):(colmiddle + b-1 + offset_shift)
    [dot_prod, dist_mag] = ...
        vector_distance(rail1,row_point1,col_point1, rail2,drow,dcol);
    if dist_mag ~= 0
        total_induct = total_induct + (dot_prod/dist_mag);
    end
end
end
```

```

%%%%%%%%%%%%%%%%%%%%%%%%%%%%%%%%%%%%%%%%%%%%%%%%%%%%%%%%%%%%%%%%%%%%%%%%
%   Robb Merrill, Dec 09
%   vector_calc.m -
%       (1) calculates the dot product, depending upon which rails of
%           loop1 and loop2 are being used
%       (2) calculates the vector distance between two given points
%%%%%%%%%%%%%%%%%%%%%%%%%%%%%%%%%%%%%%%%%%%%%%%%%%%%%%%%%%%%%%%%%%%%%%%%

function [dot_prod, dist_mag] = ...
    vector_distance(rail_1,drow1,dcoll1, rail_2,drow2,dcoll2)

minimum_dist = 0.5;

% Look-up table: dot_prod(rail_1, rail_2)
dot_prod_table = [ 1  0 -1  0;
                  0  1  0 -1;
                  -1 0  1  0;
                  0 -1  0  1];

dot_prod = dot_prod_table(rail_1,rail_2);

row_dist = abs(drow1-drow2);
col_dist = abs(dcoll1-dcoll2);
% calculate distance magnitude
dist_mag = sqrt((row_dist)^2 + (col_dist)^2);

if dist_mag == 0
    dist_mag = minimum_dist;
end

```

```

%%%%%%%%%%%%%%%%%%%%%%%%%%%%%%%%%%%%%%%%%%%%%%%%%%%%%%%%%%%%%%%%%%%%%%%%
%   Robb Merrill, Dec 09
%   loop_calc.m -
%       (1) Changes from array (corner) indexing to distance-from-
%           center indexing
%       (2) Creates a 'top-down view' diagram of loop1 in the plane
%       (3) Calls 'induct_calc.m' to calculate mutual inductance
%           integral
%       (4) Calls 'make_diagram2.m' to creates a 'top-down view'
%           diagram of loop2 in the plane
%%%%%%%%%%%%%%%%%%%%%%%%%%%%%%%%%%%%%%%%%%%%%%%%%%%%%%%%%%%%%%%%%%%%%%%%

function [diagram1,diagram2,total_induct] = ...
    loop_calc(plane,a,b,loop1_shift,loop2_shift)

total_induct = 0;
offset_shift = 1;          % shifts loop 2 so it isn't directly over loop1

diagram1 = plane;         % start with a plane of zeros
diagram2 = plane;
[rowsize,colsize] = size(plane);
rowmiddle = rowsize/2;
colmiddle = colsize/2;

%%%%%%%%%%%%%%%%%%%%%%%%%%%%%%%%%%%%%%%%%%%%%%%%%%%%%%%%%%%%%%%%%%%%%%%% rail 1 (left, 2a long)
dcol = colmiddle - b;
rail1 = 1;
for drow = (rowmiddle - a + loop1_shift):(rowmiddle + a + loop1_shift)

    % Assign a 'one' to the array element where a segment of the coil
    % should appear.  This way, when plotted, the coil will show up.
    diagram1(drow,dcol) = diagram1(drow,dcol) + 1;

    total_induct = total_induct + ...

induct_calc(plane,rail1,drow,dcol,a,b,loop2_shift,offset_shift);
end

%%%%%%%%%%%%%%%%%%%%%%%%%%%%%%%%%%%%%%%%%%%%%%%%%%%%%%%%%%%%%%%%%%%%%%%% rail 2 (bottom, 2b long)
drow = rowmiddle + a + loop1_shift;
rail1 = 2;
for dcol = (colmiddle - b + 1):(colmiddle + b - 1)
    diagram1(drow,dcol) = diagram1(drow,dcol) + 1;
    total_induct = total_induct + ...

induct_calc(plane,rail1,drow,dcol,a,b,loop2_shift,offset_shift);
end

%%%%%%%%%%%%%%%%%%%%%%%%%%%%%%%%%%%%%%%%%%%%%%%%%%%%%%%%%%%%%%%%%%%%%%%% rail 3 (right, 2a long)
dcol = colmiddle + b;
rail1 = 3;
for drow = (rowmiddle - a + loop1_shift):(rowmiddle + a + loop1_shift)
    diagram1(drow,dcol) = diagram1(drow,dcol) + 1;
    total_induct = total_induct + ...

```

```
induct_calc(plane,rail1,drow,dcol,a,b,loop2_shift,offset_shift);
end

%%%%%%%%%%%%%%%%%%%%%%%%%%%%%%%%%%%%%%%%%%%%%%%%%%%%%%%%%%%%%%%%%%%%%%%% rail 4 (top, 2b long)
drow = rowmiddle - a + loop1_shift;
rail1 = 4;
for dcol = (colmiddle - b + 1):(colmiddle + b - 1)
    diagram1(drow,dcol) = diagram1(drow,dcol) + 1;
    total_induct = total_induct + ...
end

induct_calc(plane,rail1,drow,dcol,a,b,loop2_shift,offset_shift);
end

% Compile the 'loop2' diagram
diagram2 = diagram2 +
make_diagram2(plane,a,b,loop2_shift,offset_shift);
```

```

%%%%%%%%%%%%%%%%%%%%%%%%%%%%%%%%%%%%%%%%%%%%%%%%%%%%%%%%%%%%%%%%%%%%%%%%
%   Robb Merrill, Dec 09
%   make_diagram2.m -
%       (1) Changes from array (corner) indexing to distance-from-
%           center indexing
%       (2) Creates a 'top-down view' diagram of loop2 in the plane
%%%%%%%%%%%%%%%%%%%%%%%%%%%%%%%%%%%%%%%%%%%%%%%%%%%%%%%%%%%%%%%%%%%%%%%%

function diagram2 = make_diagram2(plane,a,b,loop2_shift, offset_shift)

diagram2 = plane;    % start with a plane of zeros

[rowsize,colsize] = size(plane);
rowmiddle = rowsize/2;
colmiddle = colsize/2;

% Assign a 'one' to the array element where a segment of the coil
% should appear.  This way, when plotted, the coil will show up.

%%%%%%%%%%%%%%%%%%%%%%%%%%%%%%%%%%%%%%%%%%%%%%%%%%%%%%%%%%%%%%%%%%%%%%%% rail 1 (left, 2a long)
dcol = colmiddle - b + offset_shift;
rail = 1;
for drow = (rowmiddle - a + loop2_shift):(rowmiddle + a + loop2_shift)
    diagram2(drow,dcol) = diagram2(drow,dcol) + 1;
end

%%%%%%%%%%%%%%%%%%%%%%%%%%%%%%%%%%%%%%%%%%%%%%%%%%%%%%%%%%%%%%%%%%%%%%%% rail 2 (bottom, 2b long)
drow = rowmiddle + a + loop2_shift;
rail = 2;
for dcol = ...
    (colmiddle - b+1 + offset_shift):(colmiddle + b-1 + offset_shift)
    diagram2(drow,dcol) = diagram2(drow,dcol) + 1;
end

%%%%%%%%%%%%%%%%%%%%%%%%%%%%%%%%%%%%%%%%%%%%%%%%%%%%%%%%%%%%%%%%%%%%%%%% rail 3 (right, 2a long)
dcol = colmiddle + b + offset_shift;
rail = 3;
for drow = (rowmiddle - a + loop2_shift):(rowmiddle + a + loop2_shift)
    diagram2(drow,dcol) = diagram2(drow,dcol) + 1;
end

%%%%%%%%%%%%%%%%%%%%%%%%%%%%%%%%%%%%%%%%%%%%%%%%%%%%%%%%%%%%%%%%%%%%%%%% rail 4 (top, 2b long)
drow = rowmiddle - a + loop2_shift;
rail = 4;
for dcol = ...
    (colmiddle - b+1 + offset_shift):(colmiddle + b-1 + offset_shift)
    diagram2(drow,dcol) = diagram2(drow,dcol) + 1;
end

```


APPENDIX B

MAGNETIC FIELD PROFILE PLOTS

The program described below – *double_loop.m* – was developed using Matlab to compute the magnetic field profile plots of the two overlapped coils shown in Figures 2.56 – 2.58. The corresponding data of coil 1 and coil 2 were computed separately then combined using the sum-of-squares technique to produce the final image [32]. The following text describes how the sum-of-squares method was implemented in the program.

B.1 Sum-of-Squares Image Combination

After a coil detects the NMR signal from a given voxel, the NMR signal data is transformed into a pixel of intensity p . Mathematically, p is a complex vector containing data from each coil n :

$$p_{n(j,k)}^{xy} = \left[B_{n(j,k)}^x + iB_{n(j,k)}^y \right] \quad [\text{B.1}]$$

The x and y superscripts in Equation [B.1] make this vector particular to the magnetic field data calculated in the x - y cross-sectional plane (see Fig. 2.52–b). If the y - z plane

were of interest (Fig. 2.53–b) instead, the superscripts of Equation [B.1] would be altered accordingly.

The variables B^x and B^y respectively contain the x - and y -directed magnetic field components from voxel (j,k) in the plane, as detected by an isolated coil n . Thus, vector $p_{n(j,k)}^{xy}$ represents the signal intensity from a single voxel. In the program code, however, the variables B^x and B^y are treated as separate 2-D arrays to store x - and y - signal data from the entire plane, or 2-D voxel space (j,k) . For this reason, the vector p_n^{xy} (with the j and k subscripts dropped) represents the signal intensity from all voxels in the plane as detected by coil n .

Vector p can also be stated as a complex column vector to include the data from all the coils being used:

$$p^{xy} = \begin{bmatrix} B_1^x + iB_1^y \\ B_2^x + iB_2^y \end{bmatrix} \quad [\text{B.2}]$$

When combining the data of multiple coils into a single image, the general equation for the optimum combination of pixels is as follows [32]:

$$P = \sqrt{p^T R^{-1} p^*} \quad [\text{B.3}]$$

where P is the combined collection of every pixel in the plane (i.e. the final image), and R is the noise resistance matrix of the coil setup:

$$R = \begin{bmatrix} n_{11} & n_{12} \\ n_{21} & n_{22} \end{bmatrix} \quad [\text{B.4}]$$

In *double_loop.m*, coils 1 and 2 are assumed to be properly overlapped since the correct amount of coil offset for zero mutual inductance was calculated using the program in Appendix A. Thus, no noise is shared between the two coils via mutual inductance. If a conductive phantom were used in the program, some noise is still shared through electric field coupling [32]. However, the primary purpose of this code is to plot the magnetic field lines in space; thus, no electric field coupling occurs, and the values of n_{12} and n_{21} in Equation [B.4] are set to zero. Since the coils are assumed to be exactly the same, the self-noise terms n_{11} and n_{22} can be normalized to $n_{11} = n_{22} = 1$, and Equation [B.3] is reduced to the following:

$$P = \sqrt{p^T p^*} \quad [\text{B.5}]$$

After the substitution of Equation [B.2] for p , the simplified version of Equation [B.5] becomes Equation [B.6] once the complex terms are simplified:

$$P = \sqrt{p_1^T p_1^* + p_2^T p_2^*} \quad [\text{B.6}]$$

Equation [B.6] was used in *double_loop.m* to combine the magnetic field data from two isolated loops. Data from the three cross-sectional planes – xy , yz , and xz – were stored in separate 2-D arrays for each coil. Data from the two different coil overlap

directions – *transverse* (t) and *bore* (z , *along the scanner axis*) – were stored in separate arrays as well, to be plotted after the calculations were performed.

As a side note, the program code makes use of the variables $S1$ and $S2$ in place of p_1 and p_2 , and $totalS$ in place of P .

B.2 Program Code

```

%%%%%%%%%%%%%%%%%%%%%%%%%%%%%%%%%%%%%%%%%%%%%%%%%%%%%%%%%%%%%%%%%%%%%%%%
%   Robb Merrill, Dec 09
%   double_loop.m - This program displays the magnetic field profiles
%                   of two overlapped loops, when overlapped along
%                   both the transverse and bore-axis planes [Figs.
%                   2.56 - 2.58].
%
%   Supporting functions:  overlap.m,
%                           plane_calc.m,
%                           single_point.m
%%%%%%%%%%%%%%%%%%%%%%%%%%%%%%%%%%%%%%%%%%%%%%%%%%%%%%%%%%%%%%%%%%%%%%%%

clear all;
close all;
clc;

% space volume dimensions:
xsize = 200;
ysize = 200;
zsize = 200;
xy_plane = ones(xsize,ysize);           % Imaging planes
xz_plane = ones(xsize,zsize);
yz_plane = ones(ysize,zsize);

%%%%%%%%%% The optimal separation/overlap distance of 46 corresponds
%%%%%%%%%% to the a square loop size of 50mm x 50mm from Roemer.m

    a = 25;                               % half of loop x dimension
    b = 25;                               % half of loop y dimension
        % transverse overlap:
    x_sep    = 46;                         % optimal coil overlap separation
    x_offset = 2;                          % coil overlap offset to prevent
                                           %   problems from loop stacking

        % bore overlap:
    y_sep    = 46;
    y_offset = 2;

```

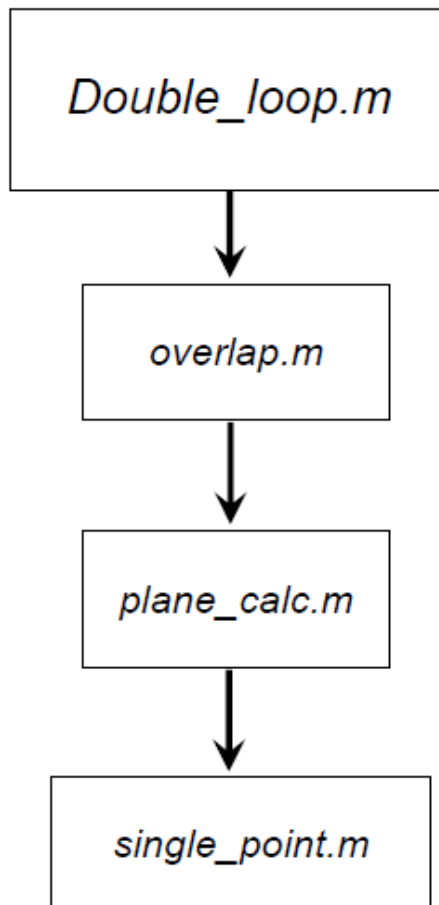


FIG. B.1: Program flow chart

```

        %%%% _t = transverse overlap direction
        %%%% _z = bore overlap
    %%%% XY
        [xy_x1_t,xy_y1_t,xy_x2_t,xy_y2_t] = ...
            overlap(xy_plane, 'xy', a,b,x_sep,y_offset);
        [xy_x1_z,xy_y1_z,xy_x2_z,xy_y2_z] = ...
            overlap(xy_plane, 'xy', a,b,x_offset,y_sep);
    %%%% XZ
        [xz_y1_z,xz_z1_z,xz_y2_z,xz_z2_z] = ...
            overlap(xz_plane, 'xz', a,b,x_sep,y_offset);
        % [xz_x1_t,xz_z1_t,xz_x2_t,xz_z2_t] = ...
        %     overlap(xz_plane, 'xz', a,b,x_offset,y_sep);
    %%%% YZ
        % [yz_y1_z,yz_z1_z,yz_y2_z,yz_z2_z] = ...
        %     overlap(yz_plane, 'yz', a,b,x_sep,y_offset);
        [yz_y1_t,yz_z1_t,yz_y2_t,yz_z2_t] = ...
            overlap(yz_plane, 'yz', a,b,x_offset,y_sep);

    %%%%%%%%%%%%%%%%%%%%%%%%%%%%%%%%%%%%%%%%%%%%%%%%%%%%%%%%%%% Contours    (the X axis in this simulation
    %%%%%%%%%%%%%%%%%%%%%%%%%%%%%%%%%%%%%%%%%%%%%%%%%%%%%%%%%%%                    is the scanner Z axis)

    %%%%%%%%%%%%%%%%%%%%%%%%%%%%%%%%%%%%%%%%%%%%%%%%%%%%%%%%%%% Complex magnitude calculation
    %     Template:
    %         S1 = x_1 + i*y_1          (loop1)
    %         S2 = x_2 + i*y_2          (loop2)
    %         total_S = sqrt[S1.*conj(S1) + S2.*conj(S2)]

    %%%% XY
        S1_xy_t = [xy_x1_t + i*xy_y1_t];
        S2_xy_t = [xy_x2_t + i*xy_y2_t];
        totalS_xy_t = sqrt(S1_xy_t.*conj(S1_xy_t) + ...
            S2_xy_t.*conj(S2_xy_t));

        S1_xy_z = [xy_x1_z + i*xy_y1_z];
        S2_xy_z = [xy_x2_z + i*xy_y2_z];
        totalS_xy_z = sqrt(S1_xy_z.*conj(S1_xy_z) + ...
            S2_xy_z.*conj(S2_xy_z));

    %%%% XZ
        %     S1_xz_t = [xz_x1_t + i*xz_z1_t];
        %     S2_xz_t = [xz_x2_t + i*xz_z2_t];
        %     totalS_xz_t = sqrt(S1_xz_t.*conj(S1_xz_t) + ...
        %         S2_xz_t.*conj(S2_xz_t));

        S1_xz_z = [xz_y1_z + i*xz_z1_z];
        S2_xz_z = [xz_y2_z + i*xz_z2_z];
        totalS_xz_z = sqrt(S1_xz_z.*conj(S1_xz_z) + ...
            S2_xz_z.*conj(S2_xz_z));

    %%%% YZ
        S1_yz_t = [yz_y1_t + i*yz_z1_t];
        S2_yz_t = [yz_y2_t + i*yz_z2_t];
        totalS_yz_t = sqrt(S1_yz_t.*conj(S1_yz_t) + ...

```

```

        S2_yz_t.*conj(S2_yz_t));

%   S1_yz_z = [yz_y1_z + i*yz_z1_z];
%   S2_yz_z = [yz_y2_z + i*yz_z2_z];
%   totalS_yz_z = sqrt(S1_yz_z.*conj(S1_yz_z) + ...
%       S2_yz_z.*conj(S2_yz_z));
%end

%%%%%%%%%% For the following plots I am using scanner
%%%%%%%%%% axes as the plot axes labels

axis_settings = [20 180 40 160];

figure(1);
    subplot(1,2,1);
    contour(totalS_xy_t,35);
    axis image; axis([60 140 20 180]);
    title('Bore overlap'); xlabel('X axis (mm)');
    ylabel('Z axis (mm)');

figure(2);
    contour(totalS_xy_z,35);
    axis image; axis([20 180 60 140]);
    title('Transverse overlap'); xlabel('X axis (mm)');
    ylabel('Z axis (mm)');

figure(3);
    plot_totalS_yz_t = rot90(totalS_yz_t);
    contour(plot_totalS_yz_t,35);
    axis image; axis(axis_settings);
    title('Transverse overlap'); xlabel('X axis (mm)');
    ylabel('Y axis (mm)');

figure(4);
    plot_totalS_xz_z = rot90(totalS_xz_z);
    contour(plot_totalS_xz_z,35);
    axis image; axis(axis_settings);
    title('Bore overlap'); xlabel('Z axis (mm)');
    ylabel('Y axis (mm)');

profile_depths = [115 125 135 145 155];
figure(21);
    hold on;
    for depth = 1:5
        profile_col = profile_depths(depth);

        %%% Transverse profile
        yz_profile_t = totalS_yz_t(:,profile_col);

        if depth == 1
            neg_profile = -yz_profile_t;
            [min_value,min_index] = min(neg_profile);

```

```
        max_value = -min_value;
    end
    yz_profile_t_norm = yz_profile_t./max_value;

%%% Bore profile
    xz_profile_z = totalS_xz_z(:,profile_col);
    xz_profile_z_norm = xz_profile_z./max_value;

    plot(yz_profile_t_norm,'b');
    plot(xz_profile_z_norm,'r--');

end

axis square; axis([0 xsize 0 1.1]);
title('Relative Flux Magnitude Profiles for Various Imaging
      Depths');
ylabel('Relative magnetic field magn. '); xlabel('Overlap axis
      (mm) ');
legend('transverse','bore');
hold off;
```



```

%%%%%%%%%%%%%%%%%%%%%%%%%%%%%%%%%%%%%%%%%%%%%%%%%%%%%%%%%%%%%%%%%%%%%%%%
%   Robb Merrill, Dec 09
%   overlap.m -
%       (1) Computes a shift-apart distance for each loop
%       (2) Calls 'plane_calc.m' to calculate the magnetic field
%           profile of each loop, and stores the results
%           in pass-back variables
%%%%%%%%%%%%%%%%%%%%%%%%%%%%%%%%%%%%%%%%%%%%%%%%%%%%%%%%%%%%%%%%%%%%%%%%
function [jflux1, kflux1, jflux2, kflux2] = ...
    overlap(plane,orientation,a,b,j_sep,k_sep)
%%% Prefix 'j' simply means one orthogonal direction in the plane,
%%%      'k' means the other orthogonal direction

[rowsize,colsized] = size(plane);
jflux1 = 0; kflux1 = 0; jflux2 = 0; kflux2 = 0;

%%%% Compute the shift distances of each loop
j1_shift = ceil(j_sep/2);      % Move up, eliminate fractions
j2_shift = -floor(j_sep/2);    % Move down, eliminate fractions

k1_shift = ceil(k_sep/2);      % Move left
k2_shift = -floor(k_sep/2);    % Move right

switch orientation
    case 'yz'
        % Obtain field data for loop 1
        [yflux1,zflux1] = plane_calc(plane,'yz',a,b,j1_shift,k1_shift);
        % Obtain field data for loop 2
        [yflux2,zflux2] = plane_calc(plane,'yz',a,b,j2_shift,k2_shift);

        jflux1 = yflux1;
        kflux1 = zflux1;
        jflux2 = yflux2;
        kflux2 = zflux2;

    case 'xy'
        [xflux1,yflux1] = plane_calc(plane,'xy',a,b,j1_shift,k1_shift);
        [xflux2,yflux2] = plane_calc(plane,'xy',a,b,j2_shift,k2_shift);

        jflux1 = xflux1;
        kflux1 = yflux1;
        jflux2 = xflux2;
        kflux2 = yflux2;

    case 'xz'
        [yflux1,zflux1] = plane_calc(plane,'xz',a,b,j1_shift,k1_shift);
        [yflux2,zflux2] = plane_calc(plane,'xz',a,b,j2_shift,k2_shift);

        jflux1 = yflux1;
        kflux1 = zflux1;
        jflux2 = yflux2;
        kflux2 = zflux2;
end

```

```

%%%%%%%%%%%%%%%%%%%%%%%%%%%%%%%%%%%%%%%%%%%%%%%%%%%%%%%%%%%%%%%%%%%%%%%%
%   Robb Merrill, Dec 09
%   plane_calc.m -
%       (1) Changes from array (corner) indexing to distance-from-
%           center indexing
%       (2) Calls 'single_point.m' to determine the magnetic field
%           contribution of every small segment of a coil loop,
%       (3) Accumulates the results and stores them in pass-back
%           variables
%%%%%%%%%%%%%%%%%%%%%%%%%%%%%%%%%%%%%%%%%%%%%%%%%%%%%%%%%%%%%%%%%%%%%%%%
function [j_comp, k_comp] = ...
    plane_calc(plane,orientation,a,b,j_sep,k_sep)

[rowsize,colsize] = size(plane);

j_comp = 0;
k_comp = 0;

xflux = zeros(rowsize,colsize);
yflux = zeros(rowsize,colsize);
zflux = zeros(rowsize,colsize);

switch orientation
    case 'yz'
        z_loc = colsize/2;
        for dz = 1:colsize
            for dy = 1:rowsize
                y = ((rowsize/2)-dy);
                z = (z_loc-dz);
                [yflux(dy,dz),zflux(dy,dz)] = ...
                    single_point(y,z,'yz',a,b,j_sep,k_sep);
            end
        end
        j_comp = yflux;
        k_comp = zflux;

    case 'xy'
        for dx = 1:rowsize
            for dy = 1:colsize;
                x = ((rowsize/2)-dx);
                y = ((colsize/2)-dy);
                [xflux(dx,dy),yflux(dx,dy)] = ...
                    single_point(x,y,'xy',a,b,j_sep,k_sep);
            end
        end
        j_comp = xflux;
        k_comp = yflux;

figure(100);
contour(j_comp+k_comp,35);
axis image; axis(axis_settings);
title('Transverse overlap');
xlabel('X axis (mm)'); ylabel('Y axis (mm)');

```

```
case 'xz'  
    z_loc = colsize/2;  
    for dz = 1:colsize  
        for dx = 1:rowsize  
            x = ((rowsize/2)-dx);  
            z = (z_loc-dz);  
            [yflux(dx,dz),zflux(dx,dz)] = ...  
                single_point(x,z,'xz',a,b,j_sep,k_sep);  
        end  
    end  
    j_comp = yflux;  
    k_comp = zflux;  
end
```

```

%%%%%%%%%%%%%%%%%%%%%%%%%%%%%%%%%%%%%%%%%%%%%%%%%%%%%%%%%%%%%%%%%%%%%%%%
%   Robb Merrill, Dec 09
%   single_point.m -
%       (1) Calculates the magnetic field (due to a small segment of
%           the coil loop) at every point in the given plane,
%           according to the equations from [Mis00].
%%%%%%%%%%%%%%%%%%%%%%%%%%%%%%%%%%%%%%%%%%%%%%%%%%%%%%%%%%%%%%%%%%%%%%%%
function [flux1_point, flux2_point] = ...
    single_point(coord1, coord2, orientation, a, b, j_sep, k_sep)

%% mag. permeability in vacuum, in units of mm
u0 = 4*pi*10^(-7) * 1000;
%% Unit current
I = 1;
coeff = u0*I/4*pi;

switch orientation
    case 'yz'
        x = 0;
        y = coord1;
        z = coord2;
    case 'xy'
        x = coord1;
        y = coord2;
        z = 0;
    case 'xz'
        x = coord1;
        y = 0;
        z = coord2;
end

c = ones(4,1); d = ones(4,1); p = ones(4,1);
q = ones(4,1); t = ones(4,1); r = ones(4,1);

%%%% Loop 1 terms
% c = row distance from y-parallel loop sides
c(1) = a + x + j_sep;
c(2) = a - x - j_sep + 1;
c(3) = -c(2);
c(4) = -c(1);

% d = col distance from x-parallel loop sides
d(1) = y + b - k_sep;
d(2) = d(1);
d(3) = y - b - k_sep;
d(4) = d(3);

for count = 1:4
    % account for x == a
    if (c(count) == 0) && (d(count) == 0)
        c(count) = 0.8;
        d(count) = 0.8;
    end
    if z == 0
        z = 0.8; % 0.8 = 'best' number after experimentation
    end
end
end

```

```

%%% Distance magnitudes
r(1) = sqrt(c(1)^2 + d(1)^2 + z^2);
r(2) = sqrt(c(2)^2 + d(2)^2 + z^2);
r(3) = sqrt(c(2)^2 + d(3)^2 + z^2);
r(4) = sqrt(c(1)^2 + d(4)^2 + z^2);

%%%%% Components of Loop 1
%%% X
bx1 = 0;
for corner = 1:4
    if ((r(corner)+d(corner))*r(corner)) ~= 0
        p(corner) = (z*(-1)^(corner+1)) / ...
            ((r(corner)+d(corner))*r(corner));
        bx1 = bx1 + p(corner);
    end
end

%%% Y
by1 = 0;
for corner = 1:4
    if ((r(corner)+((-1)^(corner+1))*c(corner))*r(corner)) ~= 0
        p(corner) = (z*(-1)^(corner+1)) / ...
            ((r(corner)+((-1)^(corner+1))*c(corner))*r(corner));
        by1 = by1 + p(corner);
    end
end

%%% Z
bz1 = 0;
for corner = 1:4
    if (r(corner)*(r(corner)+((-1)^(corner+1))*c(corner))) ~= 0
        if (r(corner)*(r(corner)+d(corner))) ~= 0
            p(corner) = ((-1)^corner)*d(corner) / ...
                (r(corner)*(r(corner)+((-1)^(corner+1))*c(corner)));
            q(corner) = -c(corner)/(r(corner)*(r(corner)+d(corner)));
            t(corner) = p(corner) + q(corner);
            bz1 = bz1 + t(corner);
        end
    end
end

switch orientation
    case 'yz'
        flux1_point = coeff*by1;
        flux2_point = coeff*bz1;
    case 'xy'
        flux1_point = coeff*bx1;
        flux2_point = coeff*by1;
    case 'xz'
        %flux1_point = bx1;
        flux1_point = coeff*by1;
        flux2_point = coeff*bz1;
end

```

REFERENCES

- [1] E. Vinogradov, A. Degenhardt, et al, "High-Resolution Anatomic, Diffusion Tensor, and Magnetization Transfer Magnetic Resonance Imaging of the Optic Chiasm at 3T," *JMRI*, vol. 22, pp. 302-206, 2005.
- [2] M. Wilejto, M. Shroff, et al, "The clinical features, MRI findings, and outcome of optic neuritis in children," *Neurology*, vol. 67, pp. 258-262, 2006.
- [3] L. J. Balcer, "Optic Neuritis," *N. Engl. J. Med.*, vol. 354, pp. 1273-80, 2006.
- [4] S. W. Atlas, L. T. Bilaniuk, et al, "Orbit: Initial Experience with Surface Coil Spin-Echo MR Imaging at 1.5 T," *Radiology*, vol. 164(2), pp. 501-509, 1987.
- [5] A. Gass, G. J. Barker, et al, "High resolution magnetic resonance imaging of the anterior visual pathway in patients with optic neuropathies using fast spin echo and phased array local coils," *J. Neurol. Neurosurg. Psychiatry*, vol. 58, pp. 562-569, 1995.
- [6] F. Fazekas, F. Barkhof, et al, "The contribution of magnetic resonance imaging to the diagnosis of multiple sclerosis," *Neurology*, vol. 53, pp. 448-456, 1999.
- [7] M. A. Rocca, S. J. Hickman, et al, "Imaging the optic nerve in multiple sclerosis," *Multiple Sclerosis*, vol. 11, pp. 537-541, 2005.
- [8] J. R. Porter, S. M. Wright, et al, "A 16-Element Phased-Array Head Coil," *Magn. Reson. Med.*, vol. 40, pp. 272-279, 1998.
- [9] J. R. Hadley, B. E. Chapman, et al, "A Three-Coil Comparison for MR Angiography," *JMRI*, vol. 11, pp. 458-468, 2000.
- [10] J. A. de Zwart, P. J. Ledden, et al, "Signal-to-Noise Ratio and Parallel Imaging Performance of a 16-Channel Receive-Only Brain Coil Array at 3.0 Tesla," *Magn. Reson. Med.*, vol. 51, pp. 22-26, 2004.
- [11] G. C. Wiggins, C. Triantafyllou, et al, "32-Channel 3 Tesla Receive-Only Phased-Array Head Coil With Soccer-Ball Element Geometry," *Magn. Reson. Med.*, vol. 56, pp. 216-223, 2006.

- [12] G. C. Wiggins, V. Alagappan, et al, "Design Optimization and SNR Performance of 3T 96 Channel Phased Array Head Coils," *Proc. Intl. Soc. Magn. Reson. Med.* 15, 2007.
- [13] J. R. Hadley, E. Minalga, et al, "20 Channel Coil Array for High Resolution Imaging of the Optic Nerve," *Proc. Intl. Soc. Magn. Reson. Med.* 15, 2007.
- [14] A. Kumar, W. A. Edelstein, et al, "Noise Figure Limits for Circular Loop MR Coils," *Magn. Reson. Med.*, vol. 64, pp. 1201-1209, 2009.
- [15] Lemelson-MIT Program, (2009, Nov.), *Winner's Circle (2001): Raymond Damadian*, [Online], Available: <http://web.mit.edu/invent/a-winners/a-damadian.html>.
- [16] D. G. Nishimura, *Principles of Magnetic Resonance Imaging*, Dept. of Electrical Engineering, Stanford University, 1996.
- [17] C. L. Partain, A. E. James, et al, *Nuclear Magnetic Resonance (NMR) Imaging*, W. B. Saunders Company, 1983.
- [18] J. M. Jin, "Electromagnetics in Magnetic Resonance Imaging," *IEEE Antennas and Propagation Magazine*, vol. 40(6), pp. 7-22, 1998.
- [19] R. P. Feynman, R. B. Leighton, et al, *The Feynman Lectures on Physics*, Addison-Wesley Publishing Company, Reading, Mass., 1963.
- [20] H. H. Schild, *MRI made easy*, Berlex Laboratories, 1992.
- [21] J. R. Hadley, *Design of Optimal Radio Frequency Coils for Improved Signal-to-Noise Ratio in Magnetic Resonance Angiography*, Dept. of Electrical and Computer Engineering, University of Utah, 2006.
- [22] H. L. Krauss, C. W. Bostian, et al, *Solid State Radio Engineering*, John Wiley & Sons, New York, 1980.
- [23] R. Wolfson and J. M. Pasachoff, *Physics for Scientists and Engineers – 3rd Ed*, Addison-Wesley Publishing Company, 1999.
- [24] W. L. Stutzman and G. A. Thiele, *Antenna Theory and Design*, John Wiley & Sons, New York, 1981.
- [25] M. Misakian, "Equations for the Magnetic Field Produced by One or More Rectangular Loops of Wire in the Same Plane," *J. Res. Natl. Inst. Stand. Technol.*, vol. 105(4), pp. 557-564, 2000.

- [26] C. E. Hayes and L. Axel, "Noise performance of surface coils for magnetic resonance imaging at 1.5T," *Med. Phys.*, vol. 12, pp. 604-607, 1985.
- [27] C. Bowick, *RF Circuit Design*, Prentice Hall Computer Publishing, 1995.
- [28] C. E. Hayes and P. B. Roemer, "Noise Correlations in Data Simultaneously Acquired from Multiple Surface Coil Arrays," *Magn. Reson. Med.* vol. 16, pp. 181-191, 1990.
- [29] R. A. Kruger and L. Limin, "An electrodeless measuring technique for determining conductivity of biological tissues at radio frequencies," *Phys. Med. Biol.*, vol. 33(12), pp. 1443-1452, 1988.
- [30] K. M. Welker, J. S. Tsuruda, et al, "Radio-frequency Coil Selection for MR Imaging of the Brain and Skull Base," *Radiology*, vol. 221, pp. 11-25, 2001.
- [31] T. J. Lawry, M. W. Weiner, et al, "Computer modeling of surface coil sensitivity," *Magn. Reson. Med.*, vol. 16, pp. 294-302, 1990.
- [32] P. B. Roemer, W. A. Edelstein, et al, "The NMR Phased Array," *Magn. Reson. Med.*, vol. 16, pp. 192-225, 1990.
- [33] A. R. Applegate, (2009, Nov.), *Common Mode Currents*, [Online], Available: <http://www.k0bg.com/common.html>.
- [34] K. P. Pruessmann, M. Weiger, et al, "SENSE: Sensitivity Encoding for Fast MRI." *Magn. Reson. Med.*, vol. 42, pp. 952-962, 1999.
- [35] G. L. Zeng, *Medical Image Reconstruction*, Higher Education Press, Beijing, and Springer-Verlag, Berlin, 2010.
- [36] J. G. Och, G. D. Clarke, et al, "Acceptance Testing of Magnetic Resonance Imaging Systems." *Med. Phys.*, vol. 19(1), pp. 217-229, 1992.
- [37] D. I. Hoult, "The Principle of Reciprocity in Signal Strength – A Mathematical Guide," *Concepts Magn. Reson.*, vol. 12, pp. 173-187, 2000.
- [38] S. J. Hickman, A. M. Claudia, et al, "Optic Nerve Diffusion Measurement from Diffusion-Weighted Imaging in Optic Neuritis," *AJNR*, vol. 26, pp. 951-956, 2005.
- [39] E. K. Jeong, S. E. Kim, et al, "High-resolution DTI of a localized volume using 3D single-shot diffusion-weighted STimulated echo-planar imaging," *Magn. Reson. Med.*, vol. 56(6), pp. 1173-1181, 2006.
- [40] B. K. Rutt and D. H. Lee, "The Impact of Field Strength on Image Quality in MRI," *J. Magn. Reson. Imaging*, vol. 6(1), pp. 57-62, 1996.